STUDY OF THE EFFECTS OF SINGLE AND DOUBLE DROPLETS IMPINGEMENT ON SURFACE COOLING

A Thesis

by

HSIN-MIN TSAI

Submitted to the Office of Graduate Studies of
Texas A&M University
in partial fulfillment of the requirements for the degree of

MASTER OF SCIENCE

August 2011

Major Subject: Mechanical Engineering

STUDY OF THE EFFECTS OF SINGLE AND DOUBLE DROPLETS IMPINGEMENT ON SURFACE COOLING

A Thesis

by

HSIN-MIN TSAI

Submitted to the Office of Graduate Studies of
Texas A&M University
in partial fulfillment of the requirements for the degree of

MASTER OF SCIENCE

Approved by:

Chair of Committee,	Jorge L. Alvarado
Committee Members,	Michael Pate
	Yassin A. Hassan
Head of Department,	Dennis O'Neal

August 2011

Major Subject: Mechanical Engineering

ABSTRACT

Study of the Effects of Single and Double Droplets Impingement on Surface Cooling.

(August 2011)

Hsin-Min Tsai, B.S., National Taiwan University, Taiwan

Chair of Advisory Committee: Dr. Jorge L. Alvarado

Spray cooling is a promising technique which is used to remove large amounts of heat from surfaces. It is characterized by uniform heat removal, low droplet impact velocity and better cooling efficiency when compared to other cooling schemes. It can be used in electronic cooling, and other applications. However, due to the multiple impacts of droplets, the film fluid dynamics and morphology are quite complicated. Moreover, the effect of heat transfer under spray cooling is not well understood due to the large number of interdependent variables such as impact spacing, impact angle, droplet diameter, droplet velocity and droplet frequency to name a few. An experimental approach is proposed and used to minimize and control key independent variables to determine their effects on surface temperature and heat transfer cooling mode. The effects of droplet impact angle and spacing on different heat flux conditions are studied. The film thickness is also obtained to further investigate the relationship between the independent variable and the observed heat transfer mechanism.

The study of coherent droplet impingement on an open surface is experimentally characterized using high speed imaging and infrared thermography.

Single stream droplet impingent cooling with different impact angle is also studied. Temperature distribution and impact crater morphology are obtained under different heat flux conditions. Film thickness inside droplet impact craters is measured to understand the relationship between minimum surface temperature and film thickness. Next, double streams droplet impingement cooling with different spacings and impact angles are investigated. The optimum spacing is found to reduce the droplet-to-droplet collision and to minimize splashing, resulting in enhanced heat transfer and better use of the cooling fluid. The film thickness is also measured to understand the relationship between the heat transfer results and the controllable independent variables.

The results and conclusions of this study are useful in understanding the physics of spray cooling and can be applied to design better spray cooling systems.

DEDICATION

To Dr. Jorge L. Alvarado for his inspiration and support

To my family for their unconditional love

ACKNOWLEDGEMENTS

I would like to thank my committee chair, Dr. Jorge L. Alvarado, and my committee members, Dr. Michael Pate and Dr. Yassin A. Hassan, for their guidance and support throughout the course of this research.

Thanks also go to my friends and colleagues and the department faculty and staff for making my time at Texas A&M University a great experience. I appreciate Guillermo Soriano, Ph.D. student, for his guidance throughout this research. I also want to extend my gratitude to Office of Naval Research (ONR) for providing the funding for my research. Finally, thanks to my mother and father for their encouragement and to my girlfriend for her patience and love.

NOMENCLATURE

A	Area
C	Heat capacity
D	Digital count of infrared camera
d	Diameter
d_{32}	Sauter-mean diameter
f	Frequency
h	Heat transfer coefficient
h_{fg}	Latent heat of vaporization
I	Current
k	Thermal conductivity
L	Distance between droplets
m"	Mass flow rate
n	Refractive index
Nu	Nusselt number ($(hd)/k$)
P	Power
q	Heat
q"	Heat flux
Q"	Volumetric flow rate
Re	Renolds number ($(\rho vd/\mu)$)
s	Droplet spacing

St	Strouhal number ($(fd)/v$)
T	Temperature
t	Liquid film thickness
u	Uncertainty
V	Voltage
v	Velocity
W	Irradiance
We	Weber number ($(\rho v^2 d/\sigma)$)
β	Droplet spreading ratio
η	Fluid cooling efficiency
θ	Droplet impact angle
μ	Dynamic viscosity
ρ	Density
τ	Transmissivity

Subscript:

d	Droplet
j	Jet
l	Liquid
s	Solid
v	Vapor

TABLE OF CONTENTS

Page

Page

LIST OF FIGURES

Page

Page

Page

Page

Page

LIST OF TABLES

Page

1. INTRODUCTION

1.1. Motivation

In fast growing industries, the requirement for high speed data processing, large components production, and better equipment working efficiency are increasingly needed. Upon these demands, a large amount of heat is being generated which should be managed in an efficient manner. Some innovative cooling techniques are required to improve the efficiency, reliability and performance of new hardware instruments. Conventional air cooling and water cooling can handle heat flux between 5 and 20 W/cm^2, which may not satisfy existing requirements. Thermal management techniques such as jet cooling, spray cooling and pool boiling have the potential to dissipate high heat flux [1]. Several researchers [2-4] have shown that heat flux over $100W/cm^2$ can be dissipated using either technique. However, spray cooling has been found to have better heat transfer performance because it provides thinner film thickness and smoother wetted surface than other techniques.

Spray cooling has been studied intensely in last decade for different applications. It is widely used in many fields including metallurgical industry for fast cooling, nuclear industry to cool the fusion components [5], gas turbine industry for cooling turbine blades, and ceramic industry for thermal tempering. The present research of spray

---

This thesis follows the style of IEEE Transactions on Components and Packaging Technologies.

cooling focuses on the thermal control of a surface under constant heat flux. The thermal control is done by maintaining both low and uniform temperature along the wall surface. As mentioned above, spray cooling can provide thinner film thickness than other phase change process such as pool boiling. For most spray cooling cases, heat transfer is dominated by conduction and convection through the liquid film. Therefore, higher heat flux could theoretically be maximized by reducing the liquid film thickness because the thermal resistance and thermal boundary layer can be reduced when the liquid film thickness is reduced.

Even though spray cooling has certain advantages including uniform heat removal, the basic physical phenomena of this cooling technique is still not well understood. Due to the large number of experimental variables such as spray angle, flow rate, droplet velocity, droplet size, droplet frequency and impact spacing, the coupled heat transfer-fluid dynamic behavior still is complicated and difficult to understand by considering all the above variables simultaneously. The main mechanisms which drive heat transfer performance in spray cooling are not clear yet. In this project, the physics of single and double droplet cooling has been studied by reducing and controlling the number of variables necessary to comprehend their corresponding roles in surface cooling.

1.2. Objectives

The specific objectives of this research were to study the heat transfer effects of single stream droplet impact angle, double stream droplet impact spacings and angles

under different heat flux conditions. An infrared camera was used to capture the whole temperature map within the region of interest. The morphology inside and between impact craters was also observed using high speed imaging. Also, it was found that a lesser amount of cooling fluid could be achieved by controlling the spacing between two droplet streams. The film thickness was also measured by using the laser light total reflection technique [6]. By observing the droplet impingement mode while the droplet spacing was varied, it became obvious that droplet impact spacing was indeed an important variable that should be considered in spray cooling applications.

1.3. Organization of this work

Section 2 provides the literature review of jet cooling, spray cooling and single droplet cooling. The present research is based on the knowledge gap between these former research studies. Section 3 describes the experimental set-up used to perform heat transfer and visualization experiments. The fluid delivery system, droplet generation system, positioning system as well as data acquisition are discussed. Section 4 presents the relevant results including effects of varying impact angle, impact spacing and film thickness on heat transfer performance.

2. LITERATURE REVIEW

2.1. Spray cooling review

Spray cooling occurs when liquid is forced through a small orifice and broken into a dispersion of droplets which then impact onto a heated surface. Droplets spread on the surface and form a thin liquid film, removing large amounts of heat at relatively low temperatures due to the latent heat of the evaporation in addition to single phase convection effects. Figure 1 shows the four typical heat transfer mechanisms that can be encountered in spray cooling. Forced convection dissipates heat in the radial direction, while the fluid remains in the liquid phase. Boiling nucleation occurs at the surface where vapor bubbles form. Secondary nucleation is caused by entrained air bubbles formed by the droplet impingement on the film, generating nucleation sites for heterogeneous nucleation. Film evaporation is caused by the liquid phase change which occurs at the film-ambient air interface.

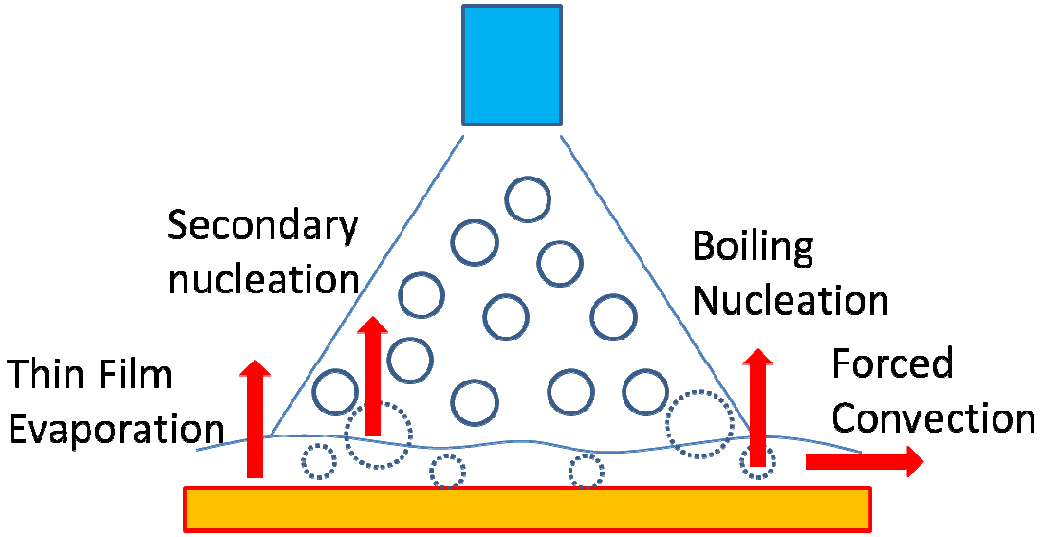

Figure 1 Main heat transfer mechanisms in a spray cooling system

Spray cooling nozzle can be categorized as hollow-cone, full cone, single spray nozzle, array spray nozzle, and gas-atomizing nozzle. Sprays typically consist of a wide range of droplet sizes. The parameter that is generally used to characterize spray is the Sauter mean diameter, d_{32}, the droplet diameter with the same volume-to-surface area ratio as the entire spray:

$$d_{32} = \frac{\sum n_i d_i^3}{\sum n_i d_i^2} \quad (1)$$

The droplet velocity exiting the nozzle in liquid atomized sprays can be estimated from Ghobane and Holman [7]:

$$V_0 = \left[V_{tube}^2 + \frac{2\Delta P}{\rho_l} - \frac{12\sigma}{\rho_l d_{32}}\right]^{1/2} \quad (2)$$

Weber number is a dimensionless number used in the analysis of spray cooling studies. Weber number is defined it as the ratio of the fluid's inertia to its surface tension.

$$We = \frac{\rho v^2 d_{32}}{\sigma} \quad (3)$$

where ρ is the density of the fluid, v is the velocity and d_{32} is the Sauter mean diameter. Weber number is useful in analyzing the thin film flows and formation of droplets and bubbles.

Hsieh and Tien [8] studied spray cooling on a flat plate in the non-boiling regime. The average Nusselt number was calculated based on the heat flux along the center and the side length (L) of the plate. It was found that Weber number and droplet size had a strong effect on heat transfer rate as shown in Equation 4.

$$\overline{Nu_L} = 933We^{0.36}\left({}^{d_{32}}/_{d_0}\right)^{0.25}\left({}^{\Delta T}/_{T_s}\right)^{0.027} \quad (4)$$

where d_0 represented the spray nozzle diameter, ΔT represented the temperature difference between the fluid and the surface. From the equation, higher heat removal rate can be obtained with large Weber number and nozzle diameter. Nevertheless, Soriano (2011) studied multiple droplet impingement and determined that Weber number was not strongly correlated to Nusselt number as volumetric flow rate. Soriano's work made evident that spray cooling correlations should consider variables such as volume flow rate, and droplet spacing before correlating non-dimensional physical variables to Nusselt number or any other indicator of heat transfer performance.

2.1.1. Sparse and dense spray

Horacek et al. [9] investigated the effect of nozzle-to-heater (vertical) spacing on heat transfer. A 96-microheater array with total area of 0.49 cm^2 was used. The heat transfer across the heater was found to be more uniform for higher nozzle distance while the total heat flux remained the same. This meant that sparse spray provides more uniform heat flux. Two nozzles were used to study the effects of droplet collisions on heat transfer. The nozzle height was varied while the nozzle horizontal spacing was fixed. It was found out that there was an optimum droplet height for maximum heat flux. However, the optimum nozzle spacing as well as the droplet spacing was not investigated in the study. The research also found that heat flux is strongly related to the contact line length rather than the wetted area. However, the study did not consider the effects of important spray variables such as droplet velocity, individual droplet impact angle, and individual droplet spacing within the area of impact.

Chen et al. [10] conducted a study to understand spray characteristics in water-based spray cooling. The effect of four independent parameters including droplet Sauter-mean diameter (d_{32}), droplet velocity (V), droplet density (n) and droplet flux ($N=n*V$) on liquid efficiency usage at CHF (critical heat flux) were studied. They found that as mean droplet flux increases, fluid efficiency at CHF reduces indicating that denser sprays not necessarily result in better cooling. For fixed mean droplet flux, as the droplet density reduces and velocity increases, CHF increases indicating that droplet velocity is a dominating factor in heat transfer. The higher droplet velocity helps droplet wetting of the surface, thereby, increasing the CHF and fluid efficiency. In other words, the sparse

spray provides better heat transfer performance under constant droplet flux. The conclusion of that study contradicts with observations made by Estes and Mudawar [11]. They claimed that CHF only depends on the surface wetted area. The maximum heat flux occurs when the entire surface is just covered by fluid. The density of the droplet does not affect the CHF. Therefore, a detailed study is needed to understand when sparse or dense sprays are more favorable.

Pautsch et al. [12] studied the effects of multiple nozzle arrays of spray cooling on heat transfer. The cooling performance was determined by spray efficiency. The spray efficiency is defined by the ratio of CHF to the heat transfer capability of the fluid, as shown in Equation 5.

$$\eta = \frac{q^{"}}{m^{"}[c_p(T_{sat}-T_{spray})+h_{fg}]} \quad (5)$$

Spray efficiency is limited by the area first exposed to CHF. This area often occurs at the center region of the heater due to flow interactions from neighboring nozzles. Moreover, there could exist a stagnation region in the liquid film between neighboring spray zones at the surface where heat transfer is adversely affected. The authors suggested that heat transfer performance is sensitive to nozzle spacing and the arrangement of spray nozzles.

A similar spacing study was conducted with jet impingement cooling. Since a very thin layer is formed under a jet, a very high heat transfer coefficient is achieved in this region. However, as the fluid flows outward, the liquid film thickness increases rapidly due to the stagnation of the fluid, and heat transfer rate is then reduced. This feature is undesirable for electronic chip cooling which need highly uniform temperature distribution. Typically, chip reliability decreases about 10 percent for every 2°C

increases in the operating temperature [13]. Hence, multiple jets or array of jets are used to reduce the temperature variation. With multiple jets, the interaction between jets and the nozzle arrangement becomes crucial. Martin [14] studied jet arrays and stated that the higher the number of jets in the array, and the smaller the jet diameter, result in higher heat transfer rate.

2.1.2. Inclined impact angle

Schwarzk of et al. [15] used a single spray nozzle to cool a heated surface using PF5060 at a flow rate of 22 ml/min. The inclination angle was varied between 0° and 60° with the nozzle fixed at 1.4 cm from the center of the target. The cooling capability remained the same and dropped off significantly when the angle exceeds 40°.

Aguilar et al. [16] studied the effect of impact angle on heat flux and overall heat extraction during cryogenic spray cooling. It is shown that angles as low as 15° has an insignificant impact (<5%) on surface temperature, heat flux (*q"*) and overall heat extraction (*Q*). Only exaggerated angle of 85° normal to the surface results in 10% lower heat flux and 30% lower heat extraction with respect to the maximum values measured when the nozzle is aimed normal to the surface.

Visaria and Mudawar [17] studied the effects of spray inclination on two-phase cooling and critical heat flux. It was noticed that inclination angle has little effect on single phase and nucleate boiling regions of the boiling curve. However, CHF decreases appreciably with increasing inclination angle. The impact area has an ellipse form for inclined spray impact, which reduces rapidly with increasing inclination angle. The

lowest volumetric flux was found along the farthest downstream point of the impact point. CHF should occur at the lowest volumetric point theoretically. However, the horizontal downstream flow compensated for the weak volumetric flux (less dense flow near the downstream region) which helped avoid dryout in that region. In the study, CHF occurred along the end points of the minor axis of the impact ellipse (perpendicular to the impact line) as shown in Figure 2.

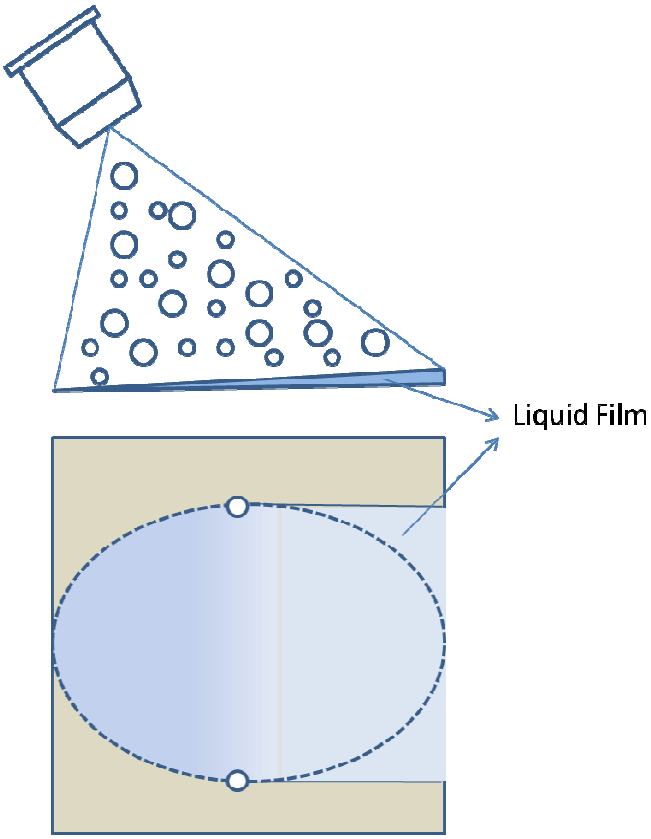

Figure 2 Scheme of inclined spray impact pattern from side and top view

When multiple nozzles were used to cool a larger surface, stagnation regions between nozzles where liquid accumulates formed. Silk et al. [18] studied the impact of inclined 2×2 array nozzle spray cooling and noticed that heat transfer rate increases within the experimental range from 0° to 45°. It was speculated that inclined sprays promote better liquid drainage from the heated surface through elimination of the stagnation zone, and may have been the reason for the observed increases in heat transfer. The effect of inclined angle on fluid drainage between sprays should be further investigated.

The mechanisms of heat transfer during spray cooling are very complicated due to its dependence on many factors such as droplet size, density and velocity. Other important factors are impact angle, impact spacing, surface roughness and nozzle geometry. It is difficult to vary each parameter independently so their effects cannot be easily understood and quantified.

2.2. Single droplet impingement cooling review

Most research studies in the area of single droplet impingement have used pressurized gas to produce droplets with large variations in droplet diameter, frequency and velocity. A piezo-electric droplet generator has been used to provide a better way to control those parameters. A droplet generator is able to independently control the droplet size, rate of formation and distance between droplets. Spreading ratio, β, is defined as the ratio between droplet diameter and the spreading diameter (impact crater diameter). Yang et al. [19] studied the droplet spreading ratio and postulated a correlation for the

droplet spreading ratio as a function of the Weber number and Reynolds number as shown in Equation 6:

$$\frac{We}{2} = \frac{3}{2}\beta^2\left\{1 + 3\frac{We}{Re}\left[\frac{\mu_{drop}}{\mu_{wall}}\right]^{0.14}\left[\beta^2\ln(\beta) - \frac{\beta^2-1}{2}\right]\right\} - 6 \quad (6)$$

Healy et al. [20] confirmed that this equation provides accurate prediction of the spreading ratio.

Droplet impingement cooling exhibits the same heat transfer regimes seen in pool boiling. The four heat transfer regimes are as follows:

1. Single phase convection ($T_w < T_{sat}$): Heat transfer occurs mainly by conduction and convection without phase change. There is a linear relation between heat flux and surface temperature.
2. Nucleate boiling ($T_{sat} < T_w < T_{CHF}$): Vapor bubbles forms near the wall and moves up to the liquid-air interface by buoyant force. Heat is removed by vaporization which increases with surface temperature up to a maximum at the critical heat flux (CHF) temperature. [21]
3. Transition ($T_{CHF} < T_w < T_{Leidenfrost}$): As the vaporization rate increases, an insulating vapor layer forms between the liquid and solid. The heat flux decreases down to local minimum at the Leidenfrost temperature [22].
4. Film boiling regime ($T_w > T_{Leidenfrost}$): A stable vapor layer forms which prevents contact between the droplet and the surface. The heat transfer is conduction through the vapor layer and radiation [23].

Most of the spray cooling research has been done at the single phase and nucleate boiling regimes. The regimes are quite complex because hydrodynamic and thermal

effects are conjugated. Stream of monodispersed droplets provide a more simplified approach in understanding the basic characteristics of droplet cooling. Several investigators have studied t droplet impact cooling.

Sellers et al. [24] studied heat transfer rate for precisely placed water droplet on a heated surface. The continuous stream of water was formed at the single hole in the orifice plate, and was decomposed into small droplets by a piezoelectric droplet generator. The drops were charged as they passed between two electrodes, and they were subsequently deflected by two sets of charged orthogonal plates. The deflection process controlled the path of the droplets and therefore the flight of the droplets could be directed in two dimensions to completely cover the heater surface in a pre-determined pattern. The droplet spacing ratio (S = s/D) is defined as the ratio of the centerline distance between adjacent drops on the surface to the diameter of the drop after it hit onto the heater surface. The maximum critical heat flux occurs when the drops were placed just beside one another (S = 1) and formed a uniform, thin film once they spread on the surface. For a single stream impacting a single location (S = 0), the correlation for the dimensionless critical heat flux is determined to be a function of Weber number and Strouhal number (Equation 7):

$$q_{CHF} = 1.1145 We^{-0.1202} St^{-0.1431} \quad \text{for } S = 0 \qquad (7)$$

where

$$23.0 < We < 202$$

$$0.047 < St < 0.58$$

When droplets impacted at different locations (S > 0), the correlation is expressed in terms of an additional dimensionless group, which is the droplet spacing divided by the length of the heated surface (s/L):

$$q_{CHF} = 0.8382We^{-0.0826}St^{-0.1654}(\frac{s}{L})^{0.2391} \quad \text{for } S > 0 \qquad (8)$$

where

$$21.6 < We < 202$$

$$2.6 \times 10^{-5} < St < 0.30$$

$$8.5 \times 10^{-3} < \frac{s}{L} < 0.47$$

Soriano [25] investigated the effect of single and triple stream droplet diameter, frequency and velocity on the heat transfer rate. It was found that spreading of the droplet is smooth at Weber number below 240. CHF increases as the Weber number increases in the spreading mode. At Weber numbers above 380, spreading of the droplets results in splashing. In the cases of splashing, heat flux decreases with Weber number. He also confirmed Sellers [26] work which correlated the effect of droplet velocity, diameter and frequency on critical heat flux. Table 1 shows the correlation for Sellers and Guillermo's work.

$$qc^{"} = Constanct * v_d^a * d_d^b * f^c \qquad (9)$$

Table 1 Critical heat flux correlation for droplet velocity, diameter and frequency

	a	b	c
Sellers	-0.0973	2.737	0.8569
Soriano	-0.169	2.772	0.904

In the case of triple (collinear) stream impingement, the key factor for the heat transfer is the horizontal spacing between droplets. For small impact spacing, the splashing of fluid reduces the heat transfer performance. From triple stream experiments, it seems that impact craters should not be deformed in order to maintain the thin film and wetted area. In the study, only three vertical impact spacing cases were tested. The effect of different impact spacing with different impact angle on fluid collision and accumulation should be studied. Moreover, the minimum surface temperature as well as temperature distribution should be determined to fully understand the effect of droplet impingement on surface cooling.

Shedd and Pautch [6] used the total light reflection technique to measure local fluid film thickness produced by sprays. They used a transparent ITO coating as heater with a 0.5 mm thick glass die deposited on the other side of the heater. When the scatter light hit an interface at incident angle less than the critical angle, most of the light is transmitted and small part is reflected. At the critical angle and above, all light is reflected back, forming a light ring around the light source point. The diameter of the ring is proportional to the thickness of the fluid film. They found that film thickness remains constant when a heat flux of 15 W/cm^2 is applied, indicating that heat transfer mechanism is dominated by single-phase convection. However, the correlation between film thickness and surface temperature was not investigated in this study.

2.3. Identification of gaps in current knowledge base

In the parametric study conducted by Schwarzk [15], Aguilar [16] and Visaria [17], spray inclined angle has little effect of the heat transfer in the single phase region. Silk [18] found that for array of nozzles, heat transfer increases as the impact angle increased from 0° to 45°. The effect of fluid drainage seems to play an important role on heat transfer. However, most recent papers [15-18] provided no detailed impact crater images at high speed to determine how fluid dynamics affect the thin film region. Understanding how single and double streams affect the fluid dynamics can be used to explain the spray cooling phenomena better.

As for the study of droplet spacing, Horacek [9] claimed that sparse spray provides more uniform heat flux while maintaining the same total heat flux. Chen et al. [10] also indicated that the sparse spray provides better heat transfer performance under constant droplet flux. On the other hand, Mudawar and Estes [11] claimed that the spray density does not affect the heat transfer. The droplet impact spacing issue is still causing controversy. The fluid interaction between droplets and the surface temperature profile has not been fully understood yet. Therefore, the optimum spacing is a crucial issue which needs to be investigated.

The film thickness within the crater for single stream vertical impact was measured by Soriano [25] under different heat flux conditions; however, the temperature profile within the crater was not correlated to the film thickness. The relation between film thickness and wall temperature in single and multiple streams impact cooling have

not been found yet. The fluid dynamic and impact crater morphology for different impact angle and spacing is still need to be investigated.

3. EXPERIMENTAL SETUP AND PROCEDURE

In order to achieve the research project objectives, an experimental setup was designed, built and calibrated. The experimental setup consisted of four main systems: fluid delivery system, positioning system, heater system and data acquisition system as shown in Figure 3 and Figure 4.

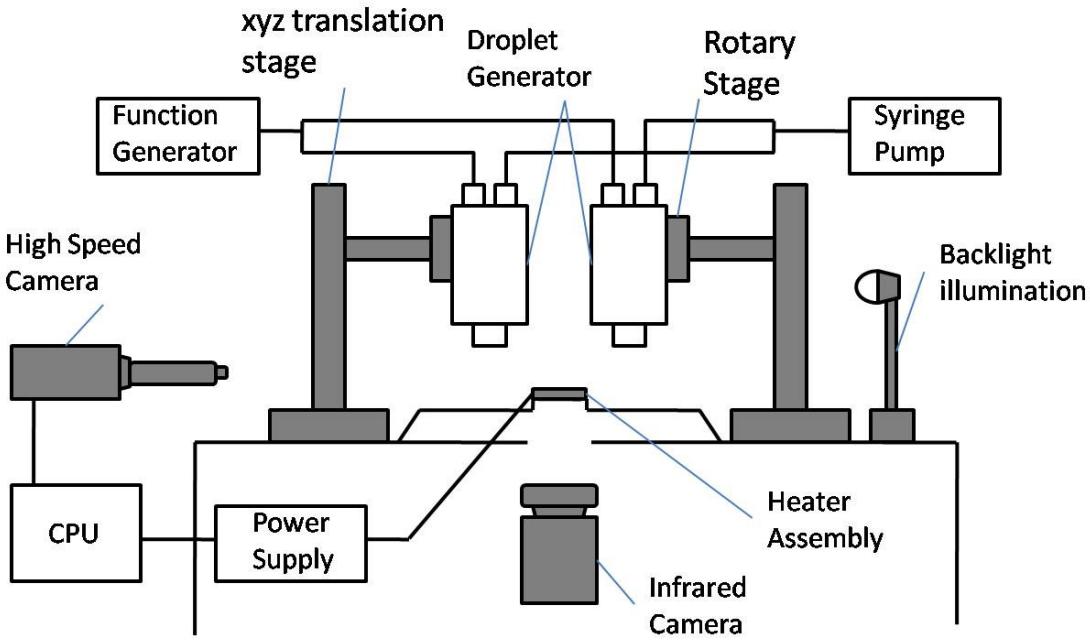

Figure 3 Experimental apparatus I

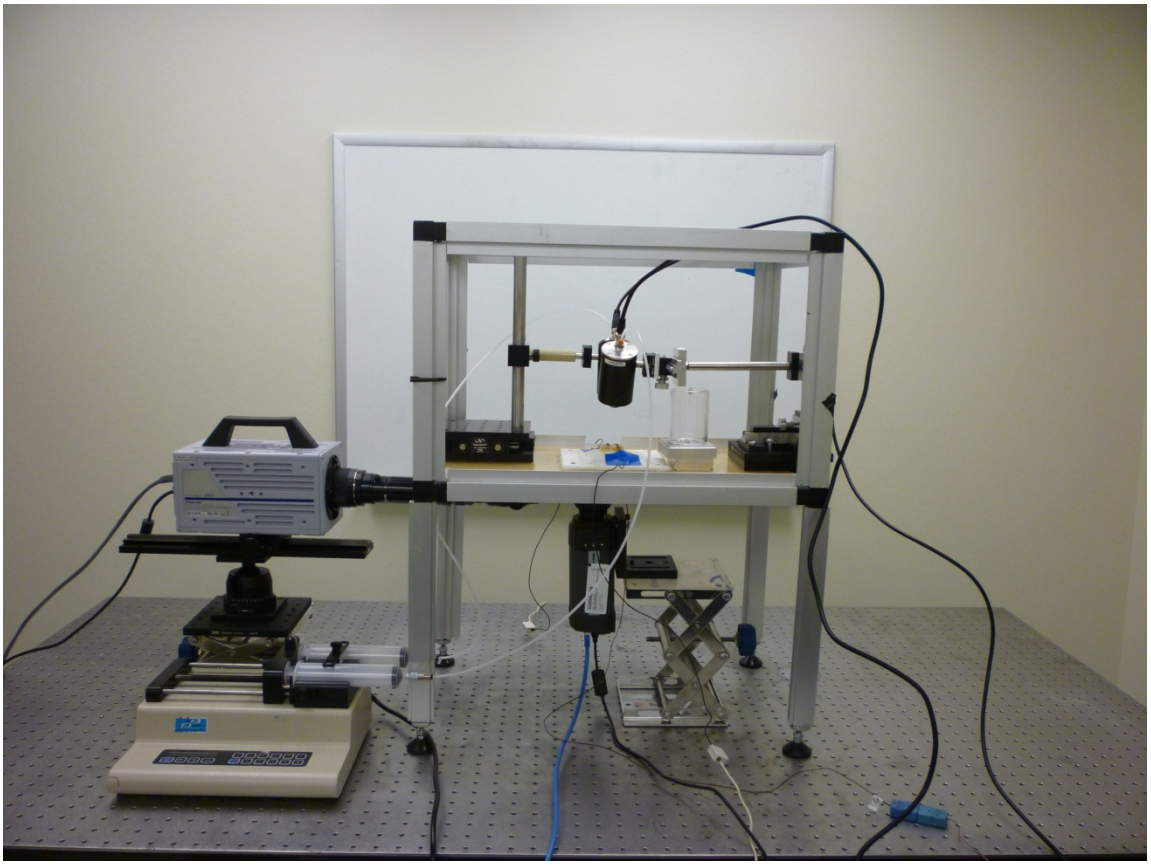

Figure 4 Experimental apparatus II

3.1. Fluid delivery system

In this study, 3M ™ Novec ™ Engineered Fluid HFE 7100 was used as the cooling fluid. It is a product made by 3M and is usually used for electronic cooling, cleaning or lubricant deposition. Table 2 depicts the specification of the fluid. The low saturation point (61°C) makes it capable for the two-phase heat transfer under some operation cooling range for electronic device.

Table 2 HFE-7100 properties specified at 25°C

Saturation Pressure (atm)	1
Density (g/ml)	1.52
Boiling point (°C)	61
Freeze point (°C)	-135
Latent heat (J/g)	111.6
Liquid specific heat (J/kg-°C)	1183
Surface tension (dynes/cm)	13.6

A syringe pump was used as the fluid delivery source. The pump can hold two parallel syringes. Two syringes with volume of 120 ml each were used. The fluid was always filtered using a 20 μm filter before filled into the syringes. The filter was used to prevent tiny particles from blocking the hole of the orifice plate. The fluid was delivered using a plastic tube with inside diameter of 1.59 mm. The other end of tube was connected to the piezoelectric droplet generator from TSI, model MDG100.

3.1.1. Single droplet stream system

A 150 μm round aperture with extra heavy substrate (National Aperture Inc.) was placed at the exit of the droplet generator (Figure 5). Mono-size droplets were generated upon the principle of Rayleigh breakup mechanism. The droplet generator was also connected to the function generator, BK Precision Model 4011A. The function generator

was used to provide square wave signal of frequency from 3700 Hz to 6500 Hz to perturbate droplet formation in a predictable manner. The fluid jet was been broken up into monodispersed droplets. The size of the droplet was determined by the frequency, flow rate and size of orifice plate. The mechanism of the droplet formation is shown in Figure 6.

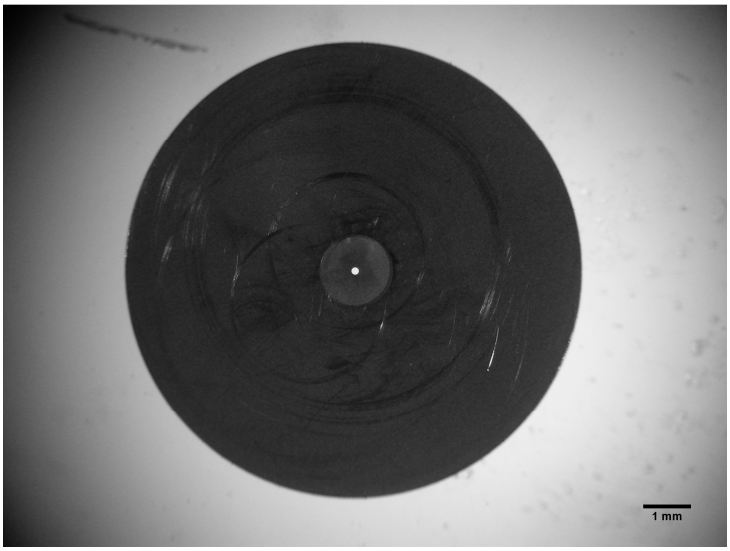

Figure 5 Single orifice plate with diameter of 150 µm

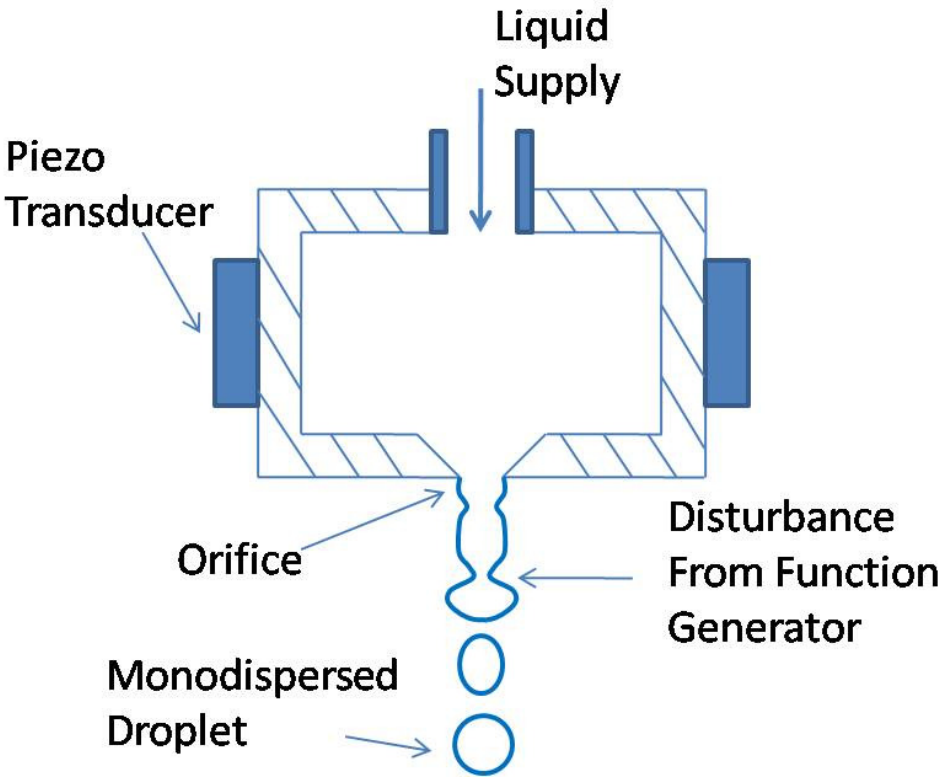

Figure 6 Mechanism of the droplet formation

3.1.2. Double droplet stream system

A double-orifice plate with extra heavy substrate was placed at the exit of the droplet generator. Two sizes of the orifice plate were used in this study. One has a diameter of 150 µm with 500 µm center-to-center distance, while the other one has a diameter of 150 µm with 750 µm center-to-center distance (Figure 7).

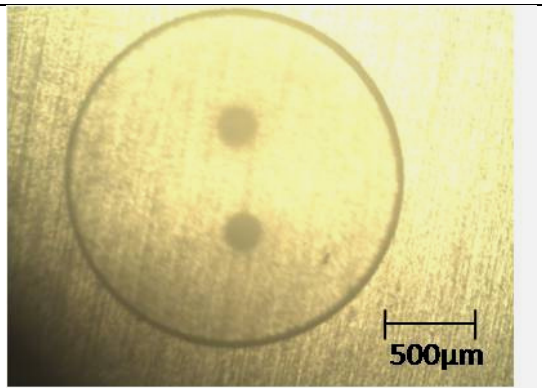

(a)

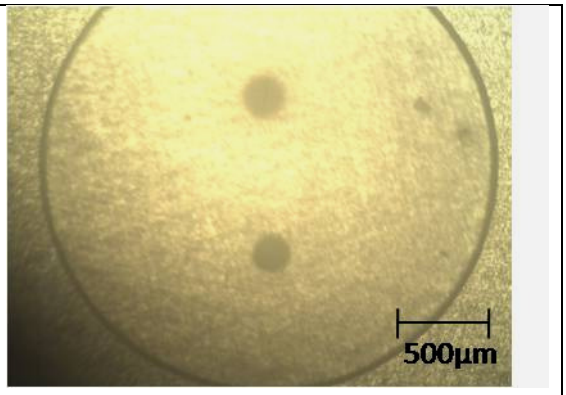

(b)

Figure 7 Double orifices plate with diameter of 150 µm (a) 500 µm center-to-center distance (a) 750 µm center-to-center distance

In theory, two streams of droplet should be parallel to each other. However, due to the bending moment exerted by the droplet generator cap, the flat orifice plate was been experienced a slightly curvature. There was 1° deviation between two streams with respect to the vertical direction of the orifice exit toward each other. Due to this phenomenon, the actual impact spacing was not exact the same as the orifice outlet spacing. The actual impact spacing can be slightly changed through adjusting the drop height. For the orifice plate with 750 µm center to center, the impact spacing can be adjusted from 500 µm to 650 µm in a drop height changed from 6 cm to 4 cm. For the orifice plate with 500 µm center to center, the impact spacing can be adjusted from 400 µm to 300 µm in a drop height changed from 4 cm to 6 cm. The velocity difference due to the gravitational effect was found to be less than 4%. Therefore, the velocity was assumed be constant through the experiment.

3.2. Positioning system

The droplet generator was hold and precisely positioned by a series of mechanical devices. A xyz translation stage was used to position the droplet generator accurately. Two sets of stages were used to control the droplet impact spacing independently. Droplet spacing was controlled by adjusting the x and y direction of the positioning stage. The spacing was measured by using the high speed images taken from below. By using two sets of translation stages, the spacing can be varied from 0 to 3000 μm under the minimum 25° impact angle (due to the setup limitation). For the 0° (vertical) impact, the droplet impact spacing was controlled by using different orifice plate with different center-to-center distance holes.

In order to control the impact angle, a rotary stage was connected between the translation stage and droplet generator. The angular control is 20 arcmin per vernier scale. The impact angle was measured by using the high speed image taken from side of the heater surface. Impingement angle was varied within the range from 0° to 45°.

3.3. Heater system

Zinc-Selenide was chosen as the substrate of the heater due to its high transmissivity in the optical range (0.6-20 μm). Morphology of the impact crater can be observed through the transparent heater. The dimension of the substrate is 15×10 mm and the thickness is 0.782 mm. A 100-nm thick Indium Tin Oxide (ITO) coating with a surface quality 60-40 on top of the substrate was used as heater. The ITO was chosen

because of the high transmissivity in the optical range. The electrical conductivity of the ITO makes it suitable coating and heater. Two wires were attached to the edges of the heater using the electrical conductive epoxy. The effective area was reduced to 0.9 mm^2 once the wires were attached. Wires were connected to a 1500 W power supply (Lambda GEN600-2.6). The power supply was controlled thorough a PC using the Microsoft Hyperterminal version 5.1. A Teflon® sample holder was used to secure the heater assembly. An adiabatic (insulating) epoxy was used to connect the heater and the holder, and to prevent the fluid leaking down to the heater. A K-type thermal couple was attached beneath the holder to read the reflective temperature. The estimated uncertainty in heat flux measurement was ±1.24 W/cm^2. Detailed calculations of the uncertainty analysis are shown in Appendix A. The heater system is shown in Figure 8.

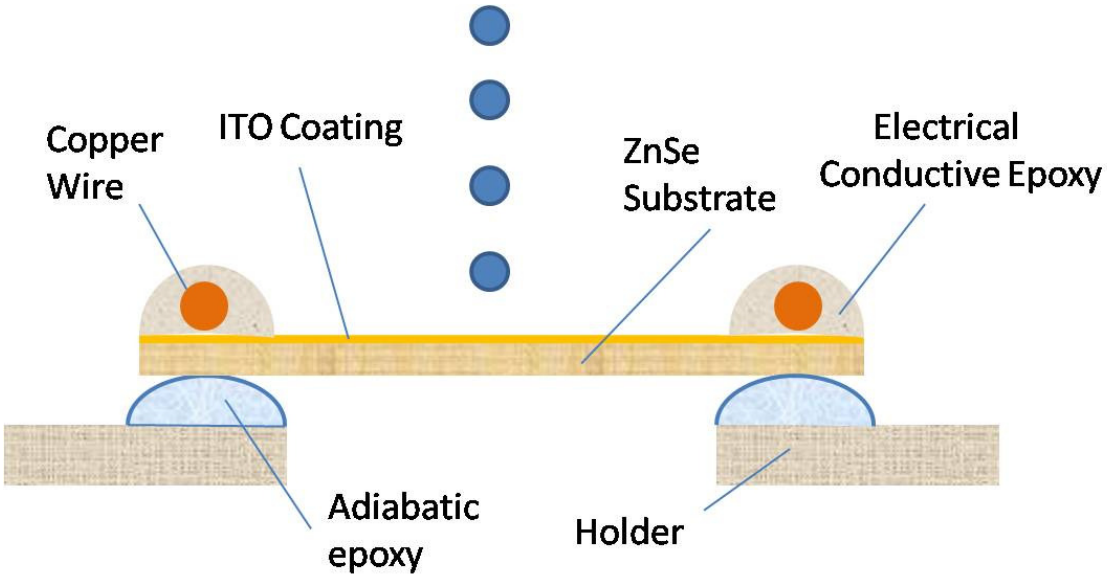

Figure 8 Heater system setup

Temperature was measured using an infrared camera (FLIR A325) located below the heater. The working distance of the lens is 79 mm and the field of view is 32 mm by 24 mm. The resolution of the lens is 100 μm per pixel, and the camera speed was set to 60 frames per second. The temperature range of the camera was between 0°C and 350°C. The temperature was obtained using the average value of 200 frames data. The uncertainty of the temperature reading was ± 1.6°C at 55°C and ± 0.8°C at 40°C as explained in appendix A. Figure 9 depicts a sample of an infrared image for a single stream impact.

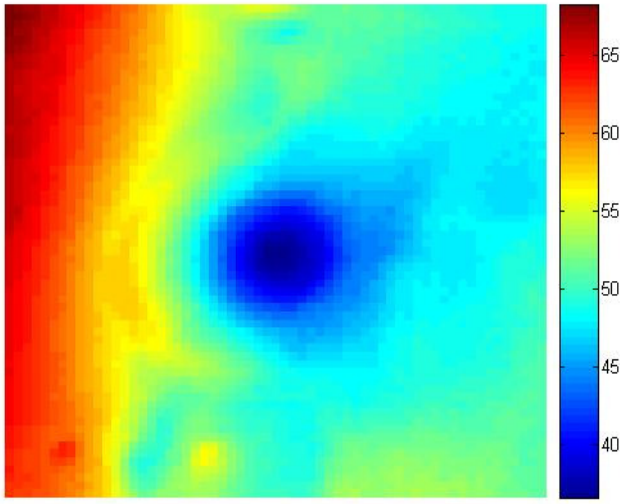

Figure 9 Infrared image for single stream under flow rate 150 ml/hr, heat flux 13.1W/cm^2

High speed images were captured using a high speed camera, Photron SA3, with a maximum speed of 60,000 frames per second. The maximum view of vision is 1024×1024 pixel. The resolution depends on the lens and frame rate. High resolution

lens were used in this research (zoom 6000 series lens Navitar). The camera can be located from either side of the heater to get a view from top or bottom using 45° mirror to capture images from below. A backlight with 250 W was used to illuminate when the high speed camera was in operation. The whole set up is shown in Figure 10.

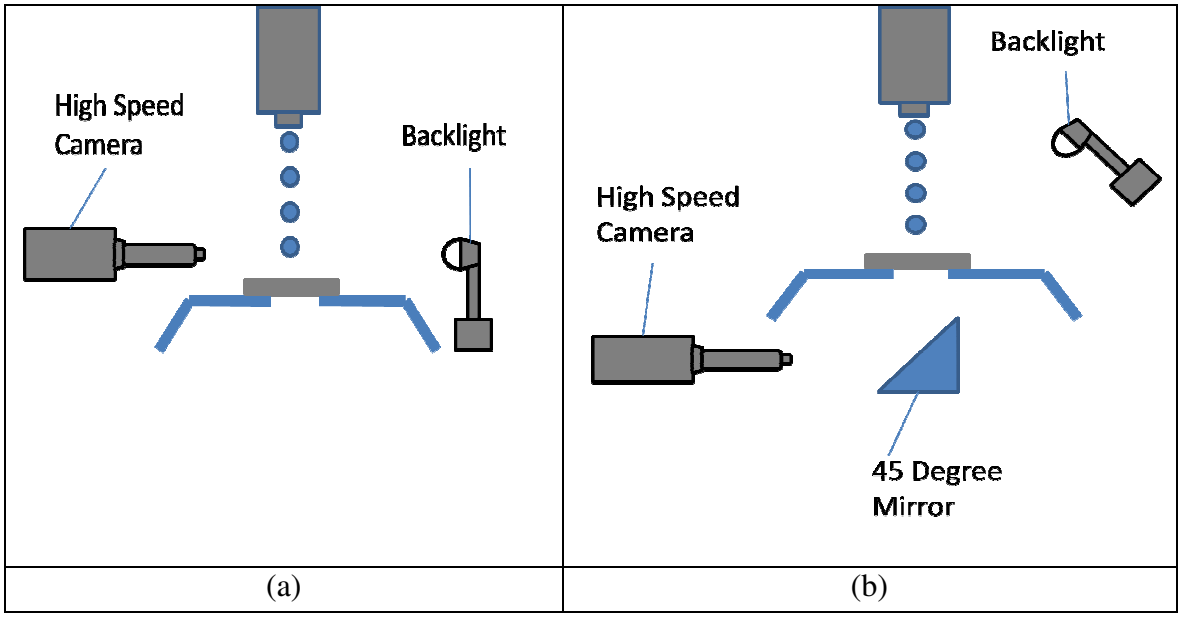

Figure 10 High speed camera setup from (a) side (b) below the heater surface

3.4. Data acquisition system

The Thermal Vision Examine IR was used as software with the infrared camera. The temperature map was calculated by importing variables such as emissivity, measure distance, room temperature, reflective temperature and relative humidity. The raw temperature data were exported as comma separated values (csv) file. Some Matlab codes were developed to get the temperature profile which is interested in.

High speed images were recorded by Photron FASTCAM Viewer which is part of the high speed camera system. Images were further processed by the software Image J to be able to determine crater and droplet sizes optically.

The droplet diameter and velocity were measured using a magnification of 3.94 μm/pixel. The uncertainty of the diameter was ±7.5 μm as shown in appendix A. The experimental value was compared to the theoretical value given by Equations 10 and 11:

$$d_d = \left(\frac{6\dot{Q}}{\pi f}\right)^{1/3} \quad (10)$$

$$v_d = \left(v_j^2 - \frac{12\sigma}{\rho d_d}\right)^{1/2} \quad (11)$$

where $\dot{Q}$ is the flow rate, f is the droplet frequency, v_j is the outlet jet velocity and σ is the fluid surface tension. The experimental values are within 10% compared to the theoretical value.

The impact images were captured by the high speed camera in two ways. The first view was from the top of the surface at 35° inclination angle. The second view was from below using a 45° mirror. Samples of impact images are shown in Figure 11. The diameter of the impact crater can be measured using images taken from below. The magnification of the view from below is 3.94 μm/pixel and the uncertainty of the diameter measurement was estimated to be ±24 μm (see Appendix A).

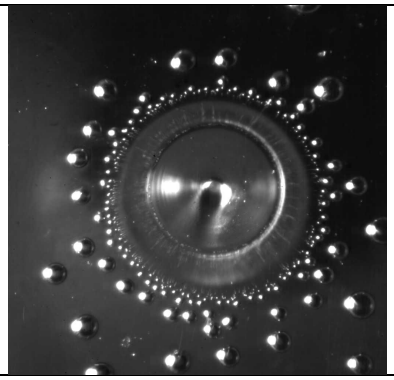

(a)

(b)

Figure 11 Typical single stream impact image from (a) below (b) top for flow rate of 150 ml/hr without heat flux

3.5. Film thickness measurement setup

The film thickness technique was developed Shedd et al [6]. The technique is based on Snell's law. Snell's law predicts that when light travels from a medium with higher refractive index to a medium with lower refractive index, some of the light would refract and some would reflect, depending on the incident angle. When the incident angle is large, most of the light will be refracted. When the angle reduces to the critical angle, all the light will be reflected by the medium boundary. The critical angle between different mediums can be calculated using Equations 12 and 13.

$$\theta_{cvl} = \arcsin\frac{n_v}{n_l} \quad (12)$$

$$\theta_{cvs} = \arcsin\frac{n_s}{n_v} \quad (13)$$

where θ_{cvl} is the critical angle between air and liquid, θ_{cvw} is the critical angle between air and substrate, n_v, n_l and n_s are the refractive index of air, fluid and substrate

respectively. The effect of a thin opaque coating on the bottom of the heater and the ITO coating on top were negligible due to the thin thickness of each layer. This technique is applicable if the refractive index of the fluid above the heater surface is known. The value of refractive index for ZnSe for a wavelength of 532 μm is 2.69. The refractive index for HFE 7100 for a wavelength of 532 μm is 1.27. Figure 12 shows the light path at the critical angle and the geometric relations for the case (a) without the liquid film and (b) with the film above the surface. The substrate thickness can be calculated using Equation 14:

$$t_s = \frac{R_s}{2\tan\theta_{cvs}} \quad (14)$$

The film thickness can be obtained using Equation 15:

$$t_l = \frac{R}{2\tan\theta_{cvl}} - \frac{t_s \tan\theta_{cvs}}{\tan\theta_{cvl}} \quad (15)$$

The light source was a 10 mW laser with a 532 nm wavelength focused at the center of the impact point. The bottom of the substrate was slightly coated with a thin layer of paint to provide a diffusive surface for the substrate. The images were captured by the high speed camera Photron SA3 at a speed of 1000 frames per second at a resolution of 1024× 1024 pixels. This technique is valid for the case when there is no air or vapor bubbles within the thin liquid film since the light path would be highly refracted and diffused if vapor bubbles were present. All the droplet impingement experiments revealed that no bubbles inside the impact crater were present.

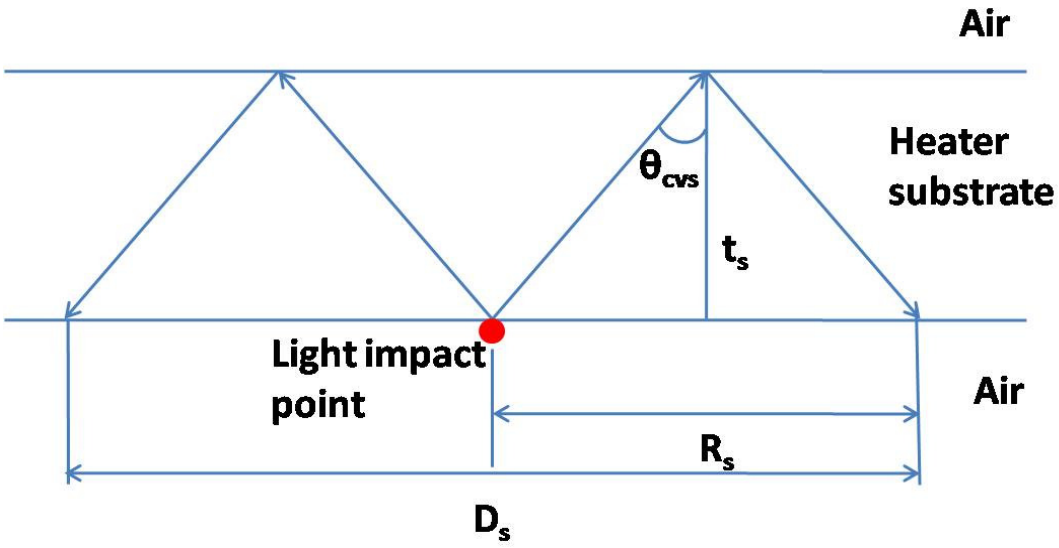

(a)

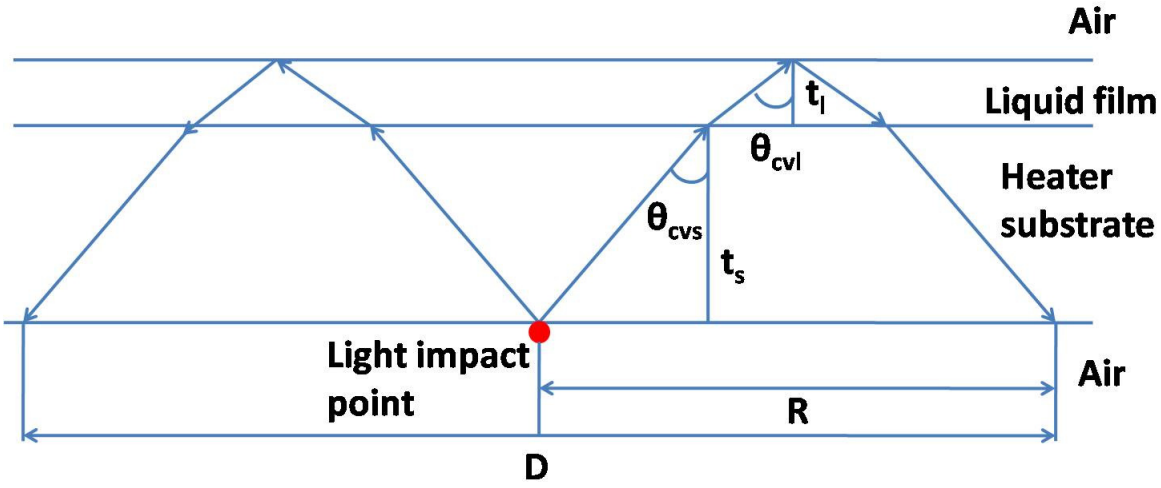

(b)

Figure 12 Film thickness measurement methodology (a) without liquid, (b) with liquid film

Besides, the technique is valid for uniform liquid flat film. If there is a gradient or slope within the film, the light path and the total reflective position will be different. Figure 13 shows the light path through the substrate and tilted fluid film.

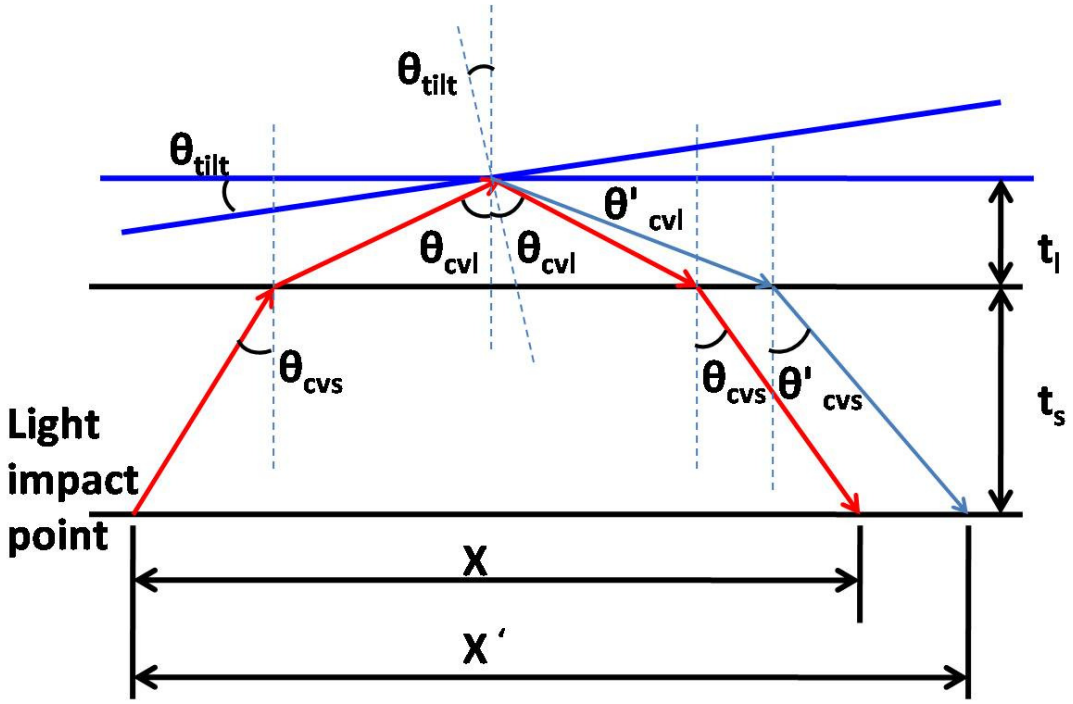

Figure 13 Film thickness methodology for tilted fluid film

The error associated with the tilting of the liquid film can be estimated using the following calculations.

$$x = 2t_s \tan\theta_{cvs} + 2t_l \tan\theta_{cvl} \quad (16)$$

$$x' = t_s \tan\theta_{cvs} + t_l \tan\theta_{cvl} + t_l \tan\theta'_{cvl} + t_s \tan\theta'_{cvs} \quad (17)$$

where x is the distance between total reflection point and the laser impact point for flat film, x' is the distance between total reflection point and the laser impact point for tilted film. θ_{cvs} and θ_{cvl} are the critical angles for flat substrate with no liquid, and air-liquid interface, respectively. By knowing the fluid and substrate refractive index, θ_{cvs} and θ_{cvl} were determined to be 52.0° and 21.8°, respectively. θ'_{cvl} is the reflected angle for the tilted substrate when a liquid layer sits on top of it. θ'_{cvs} is the refracted angle without any liquid film. These values were obtained using Equations 18 and 19.

$$\theta'_{cvl} = \theta_{cvl} + 2\theta_{tilt} \quad (18)$$

$$\theta'_{cvs} = \sin^{-1}\left(\frac{n_l}{n_s}\sin\theta'_{cvl}\right) \quad (19)$$

By assuming the liquid film was reduced to half of its thickness due to the tilting of the surface, θ_{tilt} can be estimated by Equation 20.

$$\theta_{tilt} = \tan^{-1}\left(\frac{t_l/2}{x/2}\right) \quad (20)$$

By substituting Equation 18, 19 and 20 into Equation 16 and 17, x and x' can be obtained. The error associated with the measurement of film thickness as a result of tilting can be determined by Equation 21.

$$\text{Error} = \frac{x' - x}{x} \quad (21)$$

It was found out that when θ_{tilt} was 2.8° and the film thickness error associated with it was less than 5 % when the film thickness was thinner 35 μm. Since most of the film thickness values were within this range, the technique was applicable for the film thickness measurement.

Before measuring film thickness, the thickness of the substrate was measured. This was done by measuring the light ring radius formed when a laser source was transmitted through it without fluid or heat flux condition. The substrate thickness was calculated to be 782.2 μm. This technique was further validated by measuring the thickness directly using a high precision micrometer. Substrate thickness measurement with micrometer was 787.4 ±12.7 μm. Figure 14 shows the image of the ring induced by the laser light without fluid or heat flux.

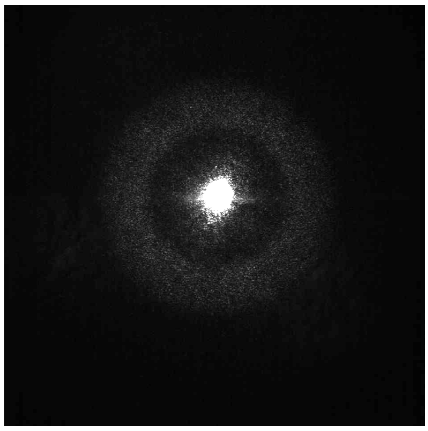

Figure 14 Ring image obtained without fluid flow and heat flux condition

When the fluid was applied to the surface, two rings were obtained. The measurements were taken at a speed of 60 fps for cases in which droplets impact at the frequency of 5200 Hz. It means that each image was composed of approximately 86 droplet impacts. Two rings represented the average of minimum and maximum film thickness during the droplet impact process. The maximum film thickness corresponds to the maximum height of the wave crest produced after each impact with an outward radius direction. The minimum film thickness corresponds to the height of the film before and after the wave motion. The two-ring feature can be seen in Figure 15.

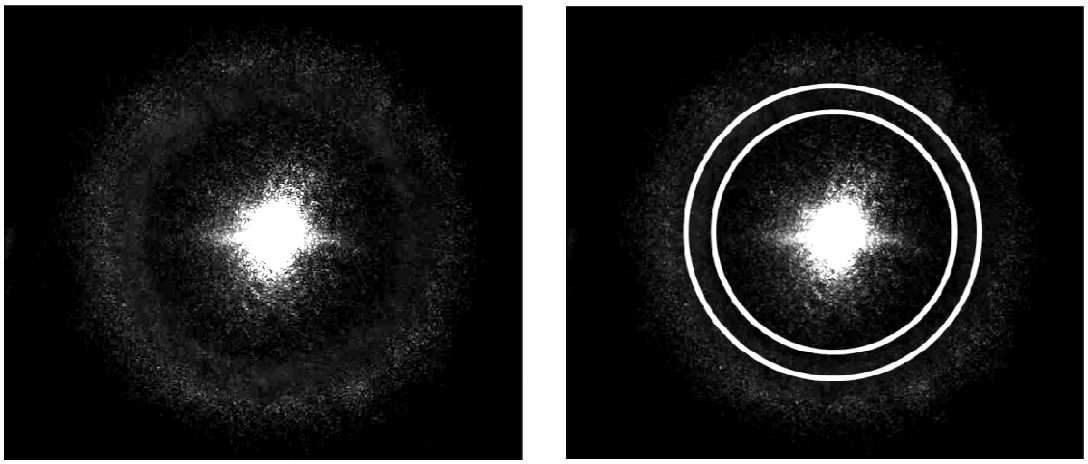

Figure 15 Film thickness for 0° impact, 150 ml/hr, 5200 Hz without heat flux condition

3.6. Single stream experiment

Before running heat transfer experiments, the top surface of the heater was cleaned using isopropyl alcohol and deionized water. The surface was then dried using a pressurized air duster. The surface was further monitored by the infrared camera to

check if there were any hot spots caused by particle contamination or a breakage in the ITO coating. The flow rate of fluid delivery system was set to 150 ml/hr, the frequency was set to 5200 Hz, and the diameter of the droplet was set to 240 μm. The only independent variable was the impact angle. The droplet generator was rotated from 0 to 15, 25, 35 and 45 degree with respect to vertical direction. Absolute velocity was assumed the same for different angles since the vertical distance between the droplet generator and the surface was set to 5 cm above the surface. Film thickness for every impact angle case was measured by the total light reflection technique which was described in the previous section. Surface temperature distribution was also measured using the described IR technique which is explained in greater detail in Section 4.

3.7. Double stream experiment

Double streams impact cooling experiments were performed using two different setups. The first setup consisted of two droplet generators, each with one single-hole orifice plate. The impact angle was fixed at 25° which was the minimum impact angle limited by the setup geometry. Two horizontal spacings were defined for this setup, as shown in Figure 16. The spacing in the x direction (parallel to impact direction) was defined as S_1, while spacing in the y direction (perpendicular to impact direction) was defined as S_2. S_1 and S_2 were varied from 0 to 2400 μm to determine the optimum spacing that could result in lower surface temperature and a more uniform temperature distribution.

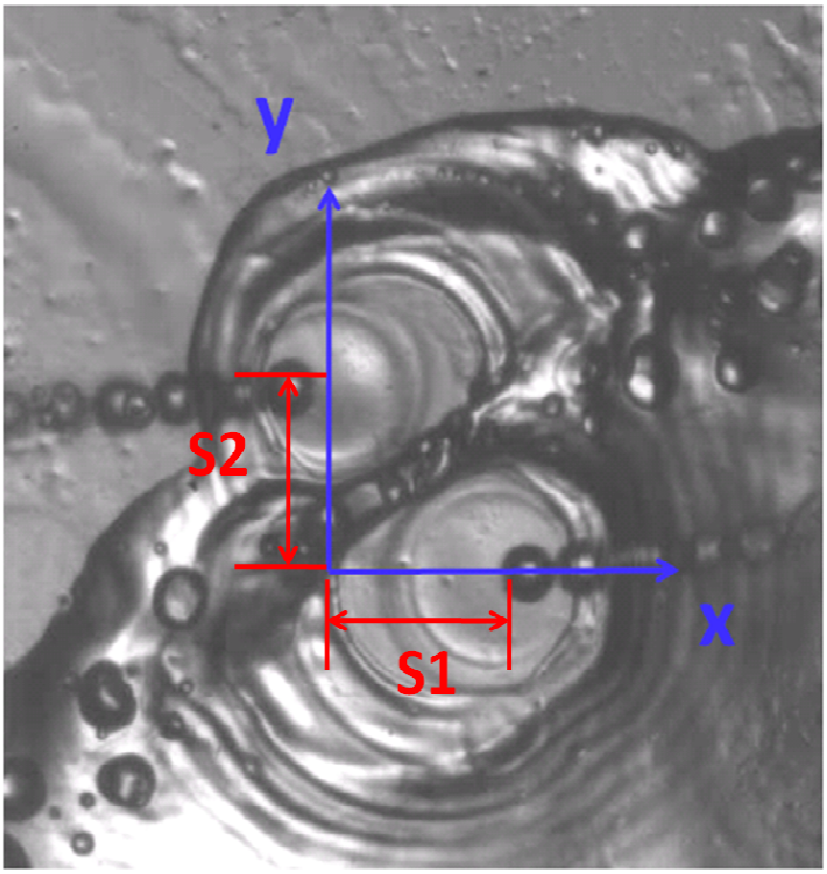

Figure 16 Image for double streams inclined impact at flow rate 150ml/hr and heat flux of 23 W/cm^2

.

The second setup consisted of one droplet generator with a two-hole orifice plate. The spacing was controlled by using different orifice plates with varied center-to-center distances between the adjacent holes as described in section 3.2. A typical impact spacing is shown in Figure 17. The spacing was varied from 330 to 650 μm to observe the effect of spacing on impingement mode within the splashing/spreading transition region. The impact angle was varied from 0° to 45° to study its effect on surface cooling

when two collinear droplet streams hit a surface under constant heat flux. Film thickness was also measured and correlated to surface temperature.

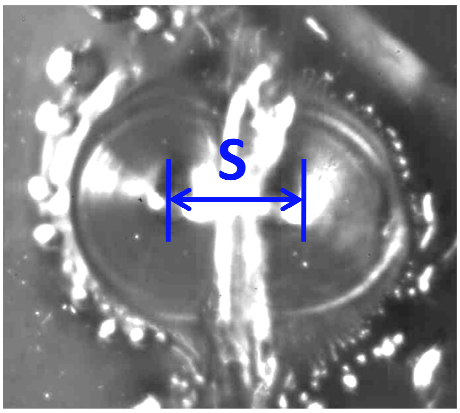

Figure 17 Image for double streams vertical impact at flow rate 150 ml/hr and heat flux of 23 W/cm^2

4. RESULTS AND DISCUSSION

In this section, droplet characterization is presented based on experimental observations. First, single droplet stream with different droplet impingement angle heat transfer results are presented. Crater morphology under effect of different angle and heat flux is also shown. Film thickness was measured and correlated with surface temperature. Then, double streams droplet impingement heat transfer results are presented which considered different spacings, impact angles, and flow rates. Impact crater morphology including crater size and corresponding film thickness when subject to impingement of double streams was also obtained. The relationship between wall temperature and film thickness was further investigated to understand its role in liquid film dynamics during heat transfer.

4.1. Droplet characterization

In order to ensure droplets were monodispersed and uniform throughout all the experiments, droplet velocity and droplet diameter were measured using the already described high speed imaging system. The measured parameters of the droplets for the single stream experiment using HFE 7100 at 20°C, 150 ml/hr, 5200 Hz are listed in Table 3. The diameter and velocity of the droplet were calculated using Equations 23 and 24.

$$d_d = \left(\frac{6\dot{Q}}{\pi f}\right)^{1/3} \quad (22)$$

$$v_d = \left(v_j^2 - \frac{12\sigma}{\rho d_d}\right)^{1/2} \quad (23)$$

where $\dot{Q}$ is the flow rate, f is the droplet frequency, σ is the fluid surface tension, d_d is the droplet diameter and v_j is the initial velocity of the jet calculated using Equation 24.

$$v_j = \frac{4\dot{V}}{\pi d_j^2} \quad (24)$$

The diameter of the jet, d_j was assumed to be the same as the diameter of the orifice plate. The experimental and theoretical values were within 5% which represented a good agreement.

Table 3 Droplet diameter and velocity measurement at a flow rate of 150 ml/hr and frequency of 5200 Hz

	Experimental Value	Standard Deviation	Theoretical Value	Difference
d_d (μm)	240.6	8.7	248.3	3.1 %
v_d (m/s)	2.24	0.04	2.35	4.6 %

4.2. Single stream results

Single stream heat transfer experiments were conducted to determine the effect of impact angle on crown morphology and surface temperature distribution.

4.2.1. Effect of impact angle on crown morphology

The effect of impact angle of droplet impingement has not been studied in detail and only has been considered in the case of spray cooling [24]. In order to determine the effect of impact angle on impact crater morphology, crater images were taken using the high speed camera. The camera was position so images could be capture from the top at 35° with respect to the horizontal plane. The impact area was measured by the image processing software Image J 1.44. Impact area was measured by several steps using Matlab 7.1:

(a) Delineate the edge of the thin film region by increasing the contrast between the thin film region and the crater edge.

(b) Trace the region boundary by using the boundary choice option in Matlab.

(c) Calculate the area within the boundary by using the image area function in Matlab.

Figures 18a and 18b shows the typical image of the impact zone for different impingement angles. In order to further study the impact zone morphology on different heat flux conditions, high speed images were taken from below as shown in Figures 18c and 18d. The resolution of each image was 1024×1024 pixels with a scale of 3.94 μm/pixel. Crater images were taken for different heat flux conditions (0-19.6 W/cm^2).When no heat flux was applied and the impact angle was set to 0° the impact area reached its largest size. The impact crater area reduced as impact angle increased. It was observed that the shape of the crater was round with a relative fixed position for the crater wall for the 0° case. The crater became more elliptical as the impact angle increased. Moreover, the location and shape of the crater wall changed and became

more rugged when the impact angle increased. The boundary of the thin film region became less recognizable for impact angles greater than 35°. The impact area was formed and sustained mainly due to the continuous impact of droplet on the surface. During the droplet impingement process, the vertical droplet momentum was changed to the radial direction as the droplet hit on the surface. At high impact frequency, droplets continuously hit the surface and form a thin film region inside the impact crater. The crater shape can be observed within this thin film region as seen in Figures 18.

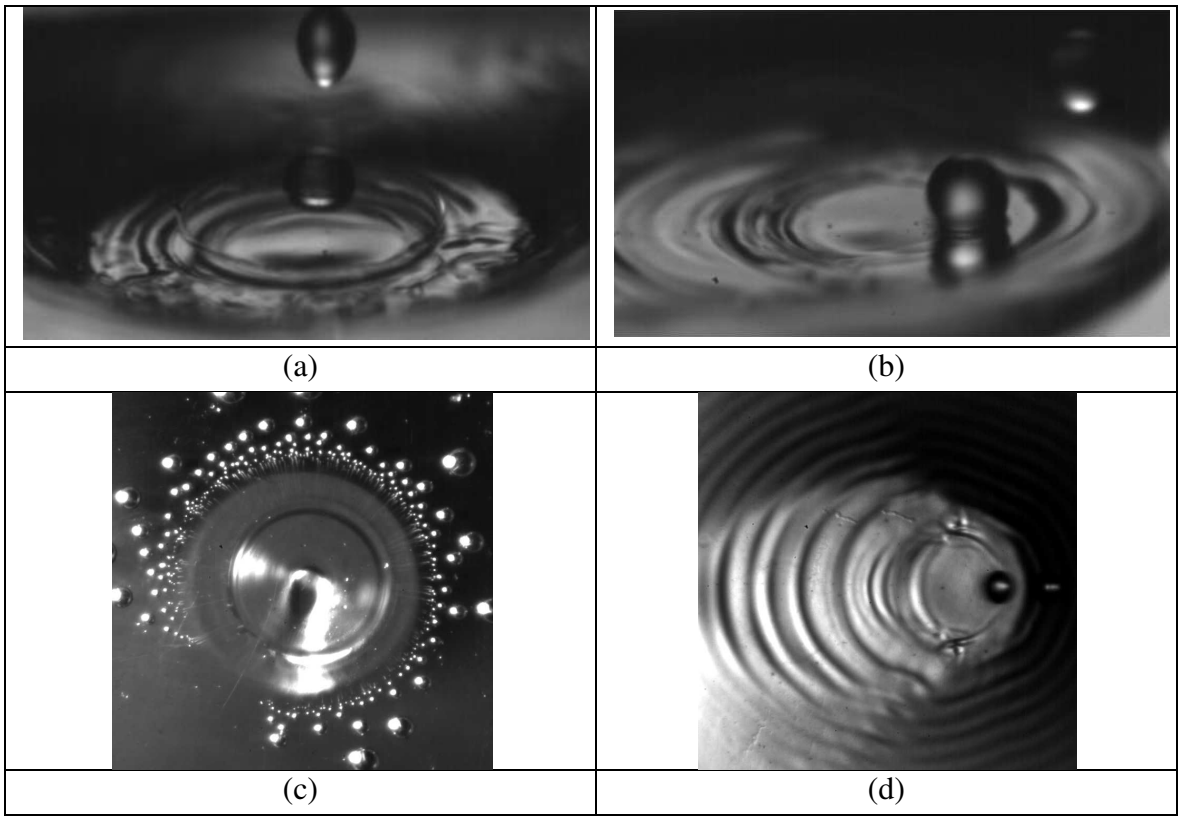

Figure 18 Crater images for (a) 0°, (b) 45° impact angle from top, (c) 0°, (d) 45° impact angle from below without heat flux condition

Figure 19 and 20 show the effect of heat flux on crater area for different impact angles. The crater area increased initially as heat flux increased until it reached a maximum value. An increase of the thin film region can be correlated by a decrease in surface tension as heat flux and surface temperature increases. The surface tension property of fluid HFE-7100 was obtained from 3M and it is shown in Appendix B. In addition, in the case of low and medium heat flux, an increment of the height of the surrounding crater wall was observed resulting in a well defined crown. However, at high heat flux values, the thin film region area reduces due to the formation of bubbles near the crater wall which increases the surface tension around the impingement zone.

Entrapped air bubbles at the edge of the crater were also observed at 0° impact angle. However, fewer or no bubbles were observed at higher impact angles to the resulting lower Weber number in the vertical direction. Also, it may be suggested that less air can be entrained when droplets hit at large angles which seem to have an effect on temperature distribution as discussed below.

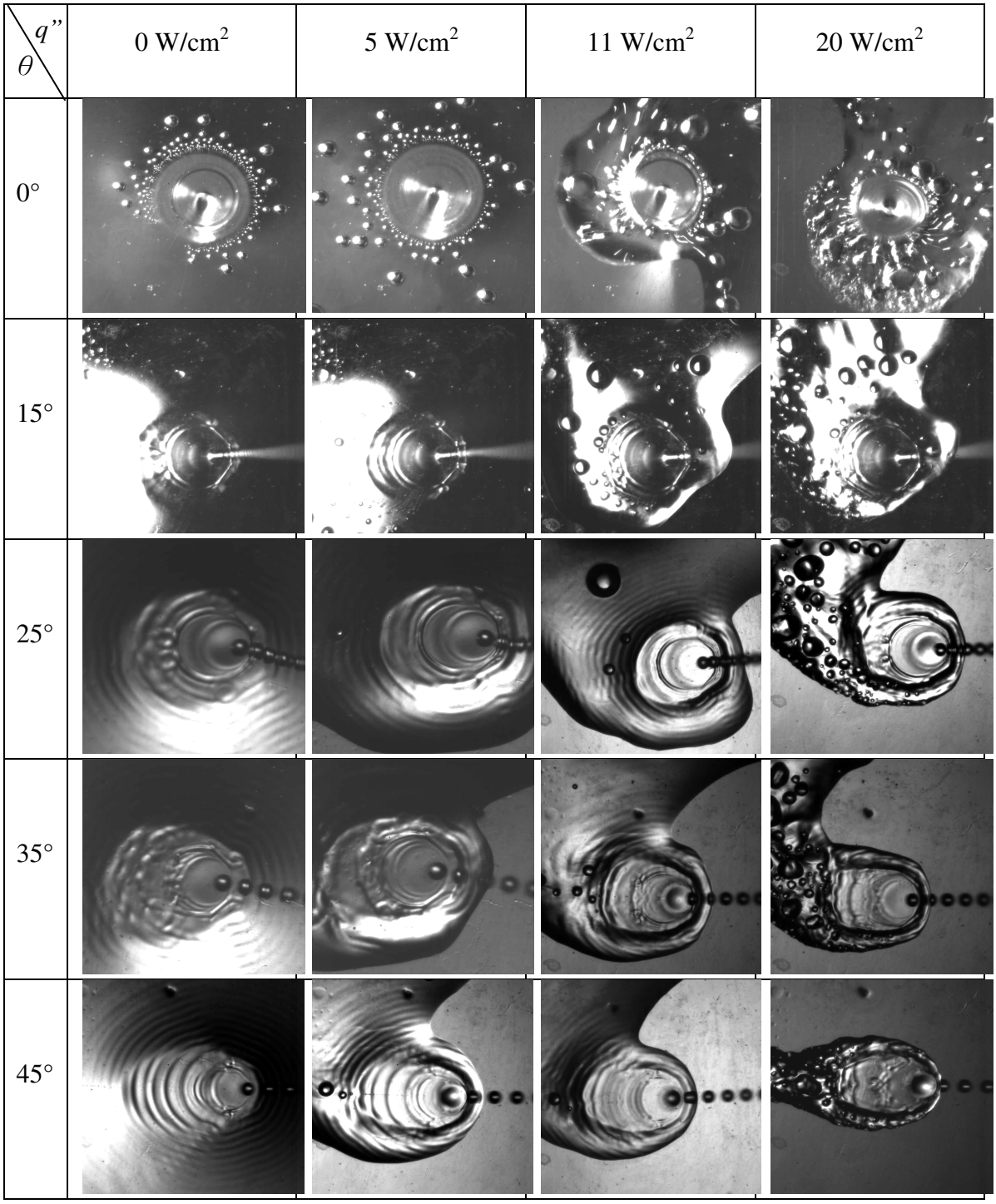

Figure 19 Crater morphology for different impact angles under different heat flux conditions, 150 ml/hr, We =142

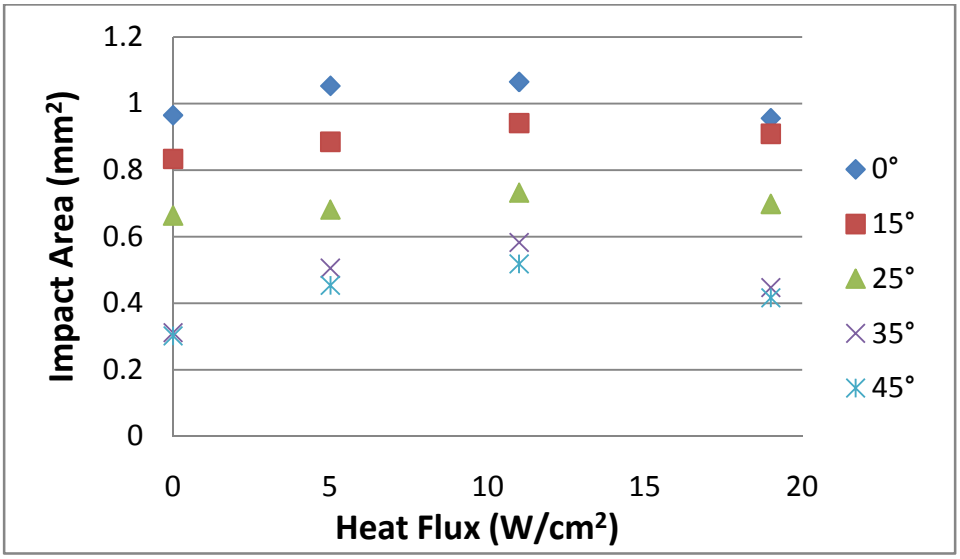

Figure 20 Effect of heat flux and impact angle on impact area

As heat flux increased, crater sizes started to reduce and became more unstable near the critical heat flux. Based on a previous critical heat flux study [25], crater deterioration should occur when the boundary of the liquid film starts to break up. When the film breaks up, the impinging droplets can no longer sustain a complete ring (crater) structure. The temperature then increases rapidly which could result in surface damage.

4.2.2. Minimum surface temperature

Surface temperatures at five different impact angles were measured to determine its effect on heat transfer. Temperatures were compared under three different heat flux conditions: low heat flux (5 W/cm^2), medium heat flux (11 W/cm^2) and high heat flux (20 W/cm^2). The location of the lowest surface temperature is near or at the impact point for all cases. Minimum surface temperatures for different impact angles under different

heat flux conditions are shown in Figure 21. At low heat flux, the minimum temperature difference among all the cases is within 1°C. As heat flux increases, 0° impact angle always shows lower surface temperature than at higher angles. Moreover, as heat flux increases, the difference between the lowest temperature at 0° and the other impact angle cases increases from 3 to 5 °C. This suggests that momentum transfer at the point of impact is highly dependent on impact angle and has a direct effect on heat transfer.

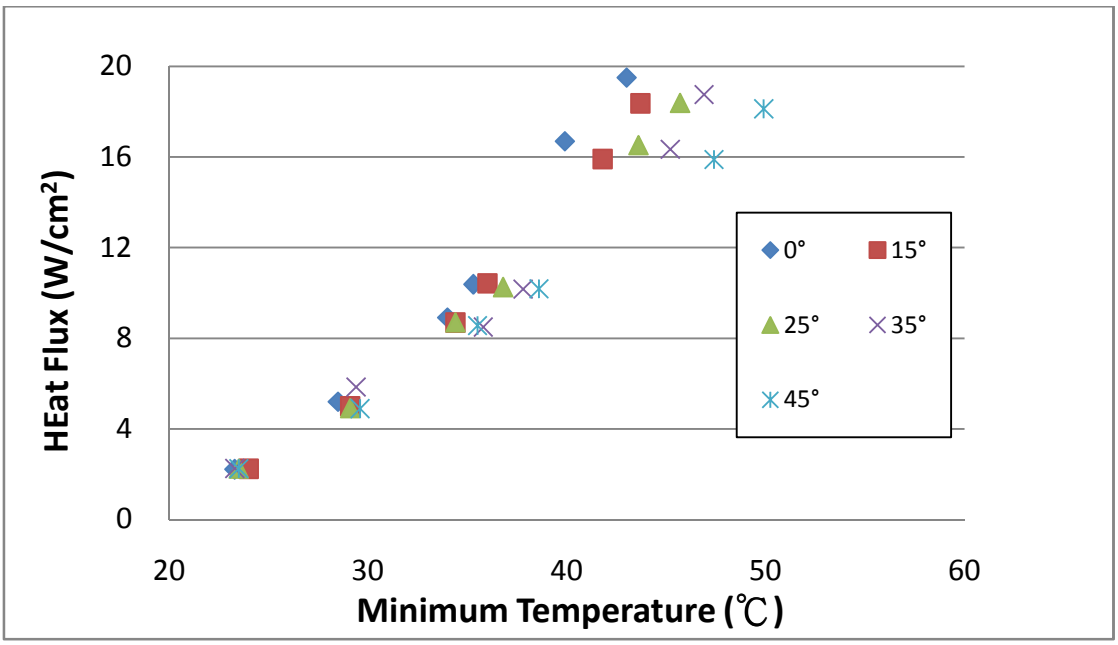

Figure 21 Effect of impact angle on heat flux and surface temperature at 150 ml/hr, We =142

Different impact angle were considered when conducting the heat transfer experiments In order to determine the effect of impact angle on temperature distribution, two temperature cross section lines through the impact point were selected for analysis

as shown in Figure 22. Figure 22 shows the cross section line parallel and perpendicular to the droplet impact direction. The zero point represents the impact point in each case.

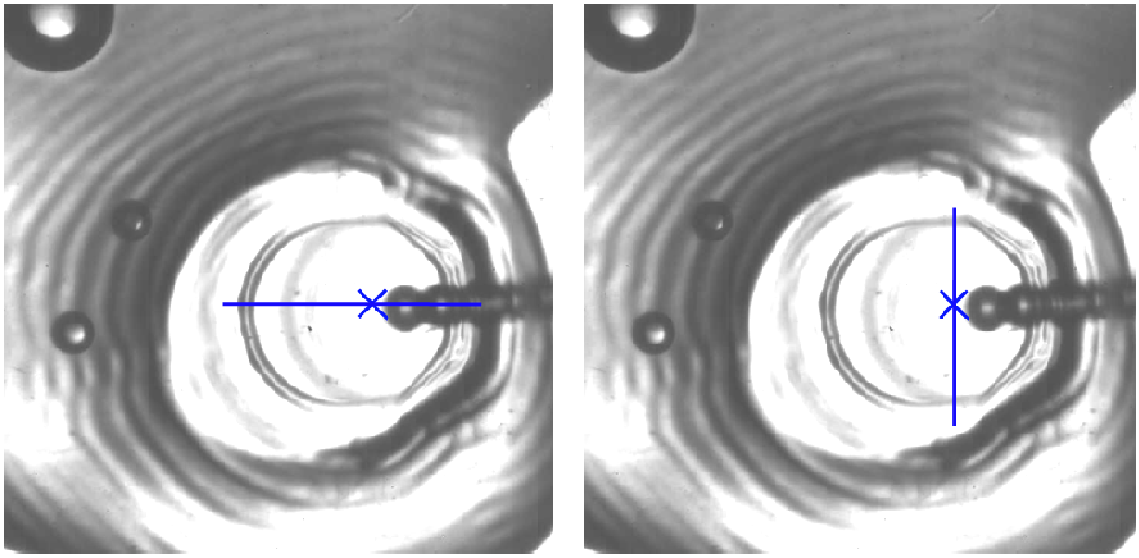

(a) (b)

Figure 22 Position and orientation of temperature profile line (a) parallel and (b) perpendicular to droplet impact direction

Figures 23 to 25 show temperature distributions parallel to the impact direction under low, medium and high heat flux conditions. The effect of impact angle is noticeable as seen in the figures. For the 0° impingement case, the temperature profile is symmetric with respect to the impact point, which exhibits the lowest surface temperature. For other impact angles, the, temperature distribution varies with droplet impact direction. Two directions are defined for all cases: The positive position (0 to 1500 μm) represents the upstream direction with respect to the impact point. The

negative position (0 to -1500 μm) represents the downstream direction with respect to the impact point. It can be observed that temperature slope is flatter in the downstream region (0 to -1000 μm) than in the upstream side. At impact angles greater than 0°, the fluid direction has a clear effect on surface cooling corroborating that single-phase forced convection is the key heat transfer mechanism inside the impact zone, which results in a more gradual temperature gradient in the downstream region. Moreover, it is worth noting that temperature increased significantly in the upstream direction as impact angle increased. On the other hand, temperature distribution in the downstream region shows little sensitivity to impact angle when the heat flux exceeds about 20 W/cm^2. It implies that the heat transfer is obviously weakened in upstream region as impact angle increases.

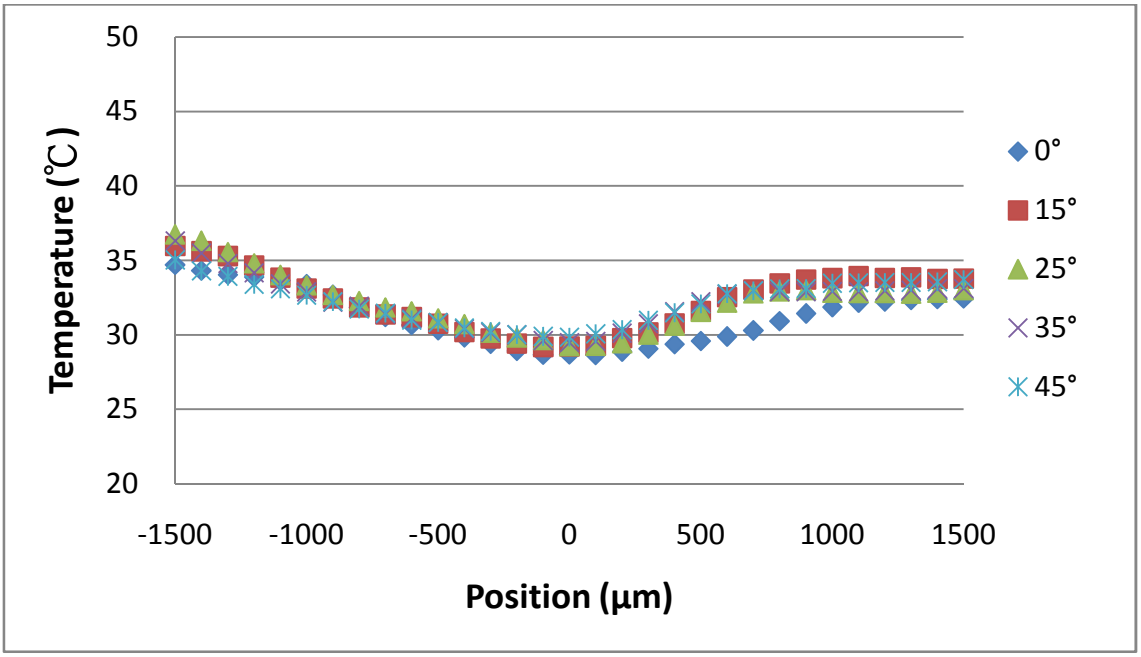

Figure 23 Single stream temperature profile parallel to impact direction at 150 ml/hr, *We* = 142, 5 W/cm^2

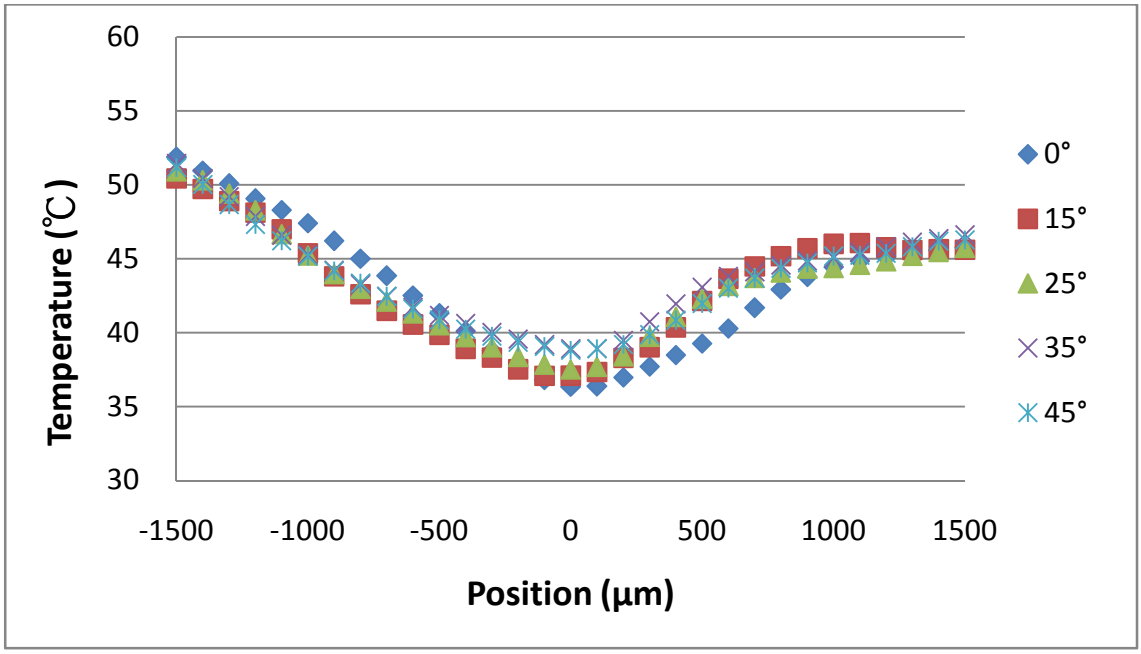

Figure 24 Single stream temperature profile parallel to impact direction at 150 ml/hr, *We* = 142, 11 W/cm^2

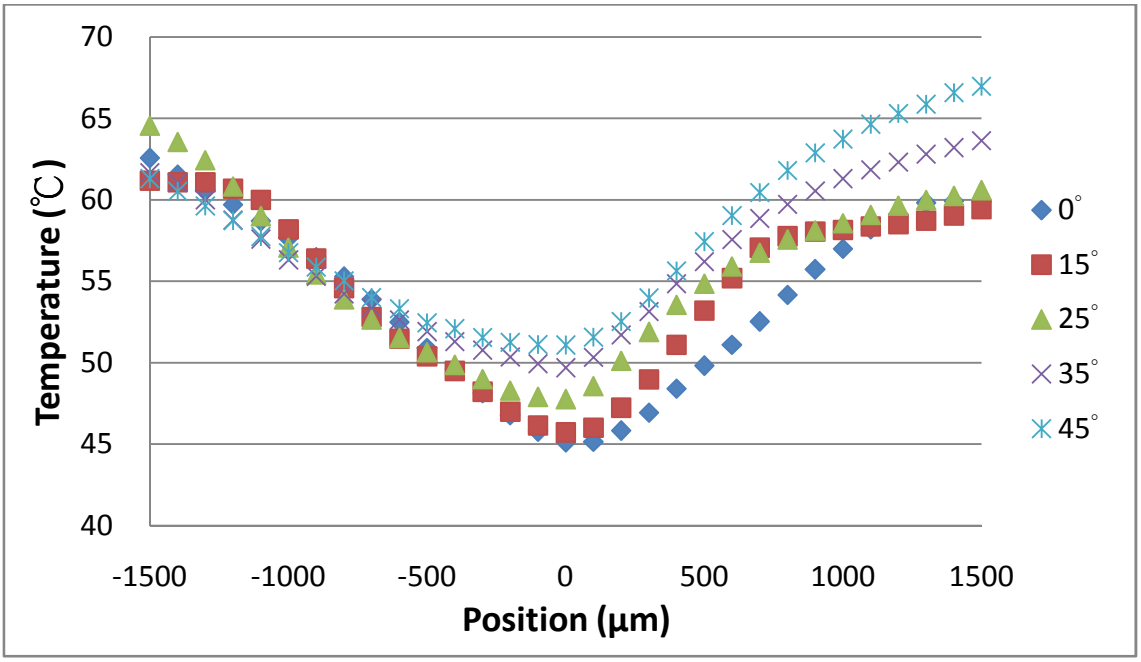

Figure 25 Single stream temperature profile parallel to impact direction at 150 ml/hr, *We* = 142, 19.6 W/cm^2

Temperature distributions perpendicular to the droplet impact direction for low, medium and high heat flux are shown in Figure 26, 27 and 28, respectively. Figures 26 to 28 exhibit that the temperature curves are symmetric regardless of impact angle. The only significant difference is that the whole temperature profile shifts upwardly as impact angle increases. From both orientation temperature profiles, it can be concluded that vertical impact (0°) results in the lowest surface temperature among all impact cases.

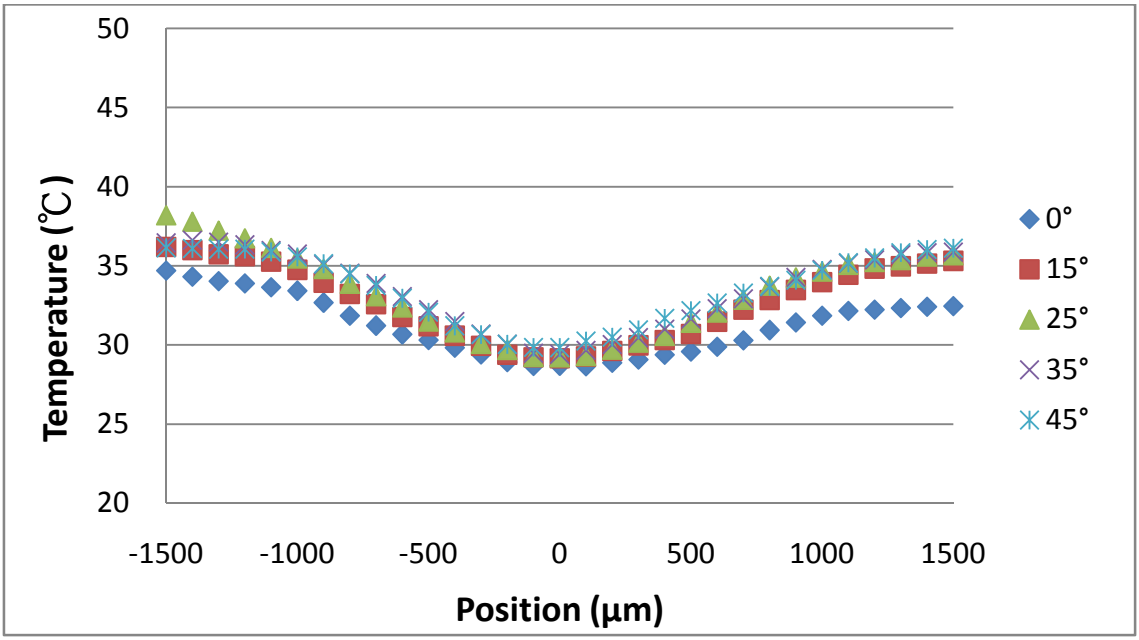

Figure 26 Single stream temperature profile perpendicular to impact direction at 150 ml/hr, *We* = 142, 5 *W/cm*^{2}

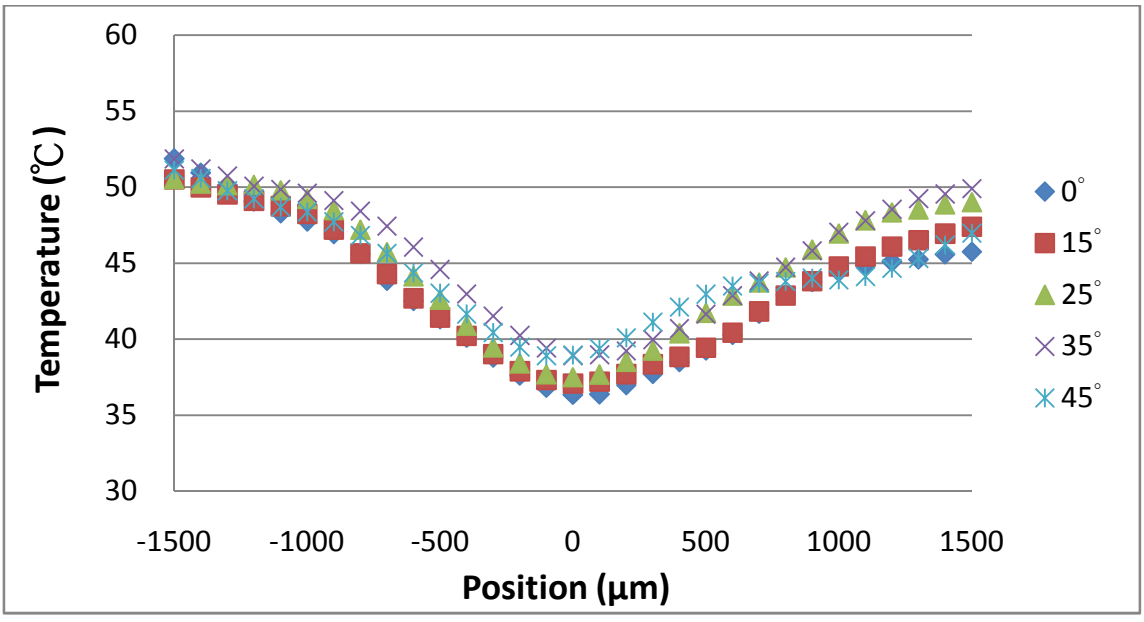

Figure 27 Single stream temperature profile perpendicular to impact direction at 150 ml/hr, *We* = 142, 11 *W/cm*^{2}

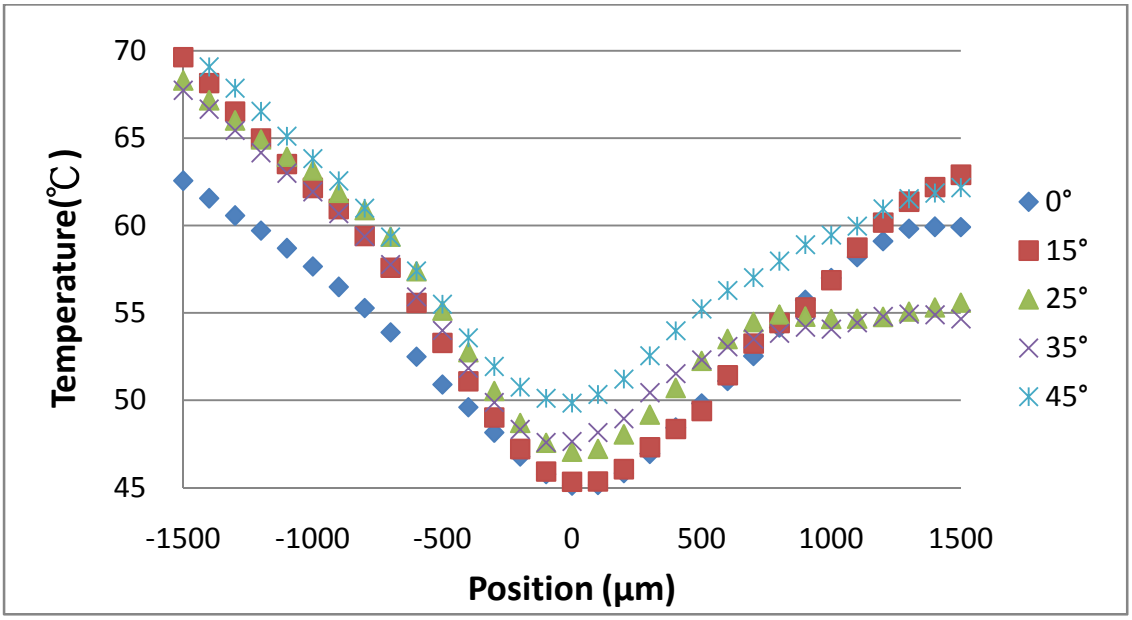

Figure 28 Single stream temperature profile perpendicular to impact direction at 150 ml/hr, *We* = 142, 19.6 W/cm^2

4.2.3. *Film thickness*

After temperature profiles were obtained, film thickness was also determined to further investigate the relationship between film thickness, impact angle and surface temperature. Film thickness data were collected in the following sequence.

1. No heat flux on the surface.

2. Low heat flux of approximately 5 W/cm^2.

3. Medium heat flux of approximately 11 W/cm^2.

4. High heat flux of approximately 20 W/cm^2 near the CHF.

For every impact angle case, four points were chosen for the film thickness measurement at 0°, 30°, 60° and 90° with respect to the droplet impact direction, as

shown in Figure 29. Figure 30 shows the measurement point of different impact angle cases. The red cross represents droplet impact point and blue crosses represent the measurement positions.

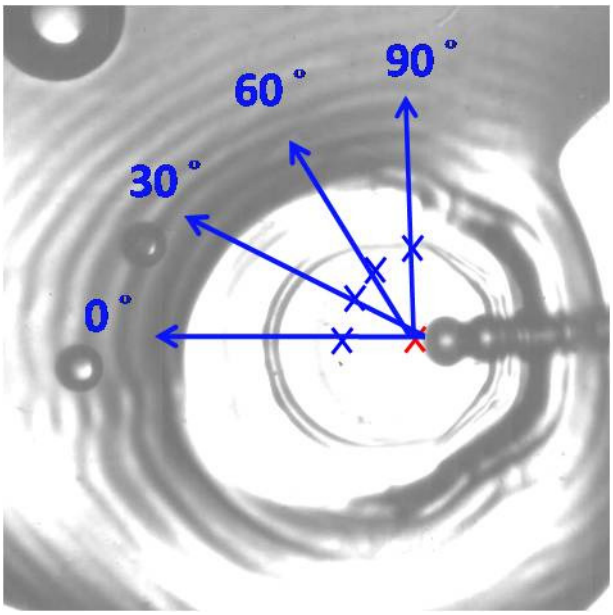

Figure 29 Different measurement positions along different angular orientations

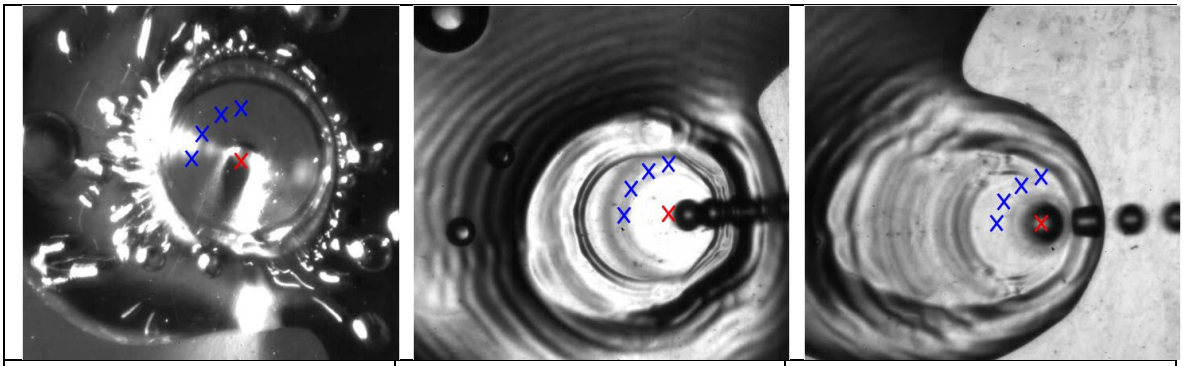

Figure 30 Different measurement positions for impact angles of (a) 0° (b) 25° (c) 45°

Film thickness values for different impact angles at different positions inside the crater are shown in Figures 31 and 32. A variation of standard deviation from 2.68 μm for maximum film thickness with no heat flux to 3.48 μm for maximum film thickness at high heat flux was found. In the case of minimum heat flux, the standard deviation of was 2.24 μm with no heat flux and 2.39 μm at high heat flux condition. It is found out that 0° impact exhibits the thinnest both maximum and minimum film thickness. It implies that vertical (normal) droplet momentum plays an important role on the thin film formation. Moreover, as Mundo et al. [27] indicated, as normal momentum decreases, there will be less energy for corona (crater wall) formation as impact angle increases. In addition, there is no clear thickness difference for different angular (horizontal) orientations for the same impact angle.

In order to correlate film thickness data to surface temperature data, it is important to know the exact location of the film thickness measurement point so the same location can be found of the surface temperature image. By substituting the thickness value in Equation 16, the measurement position (radial distance) is found to be between 340 and 380 μm (depending on the film thickness) away from the impact center. Then, the liquid film inside the crater is assumed to be flat and uniform within this region as data at different measurement points suggest.

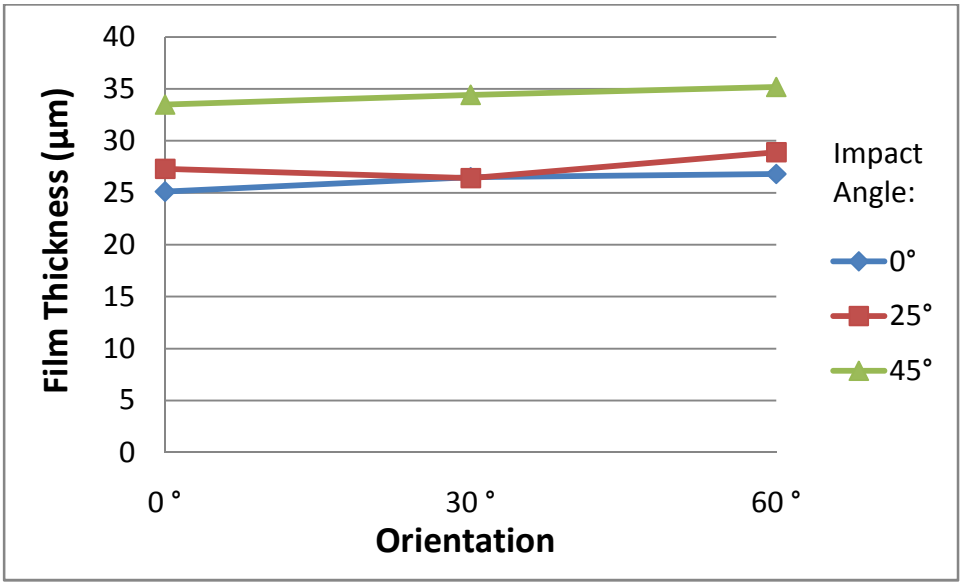

Figure 31 Minimum film thickness for different impact angle at different locations under flow rate 150 ml/hr, heat flux 11W/cm^2

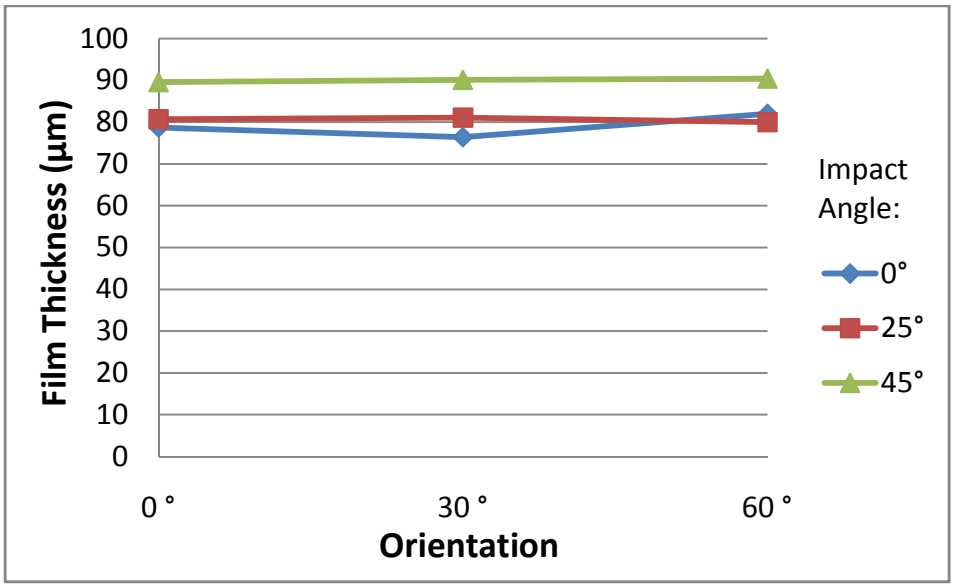

Figure 32 Maximum film thickness for different impact angle at different locations under flow rate 150 ml/hr, heat flux 11W/cm^2

Figure 31 clearly indicates that as impact angle increases the film thickness increases at the measurement points. The maximum and minimum thickness for different angle under different heat flux conditions are compared in Figure 33. The film thickness exhibits a small amount of reduction as the heat flux increases. It can be attributed to the reduction of the surface tension with respect to fluid temperature [28]. The relation between surface tension and temperature for HFE 7100 is listed in Appendix B. According to the data sheet provided by 3M, the surface tension reduces by at least 18.4% for medium heat flux condition, and 28.0 % for high heat flux condition when compared to the no heat flux case. At higher temperatures, the fluid film spreads out easier which results in thinner film thickness due to the reduction of surface tension.

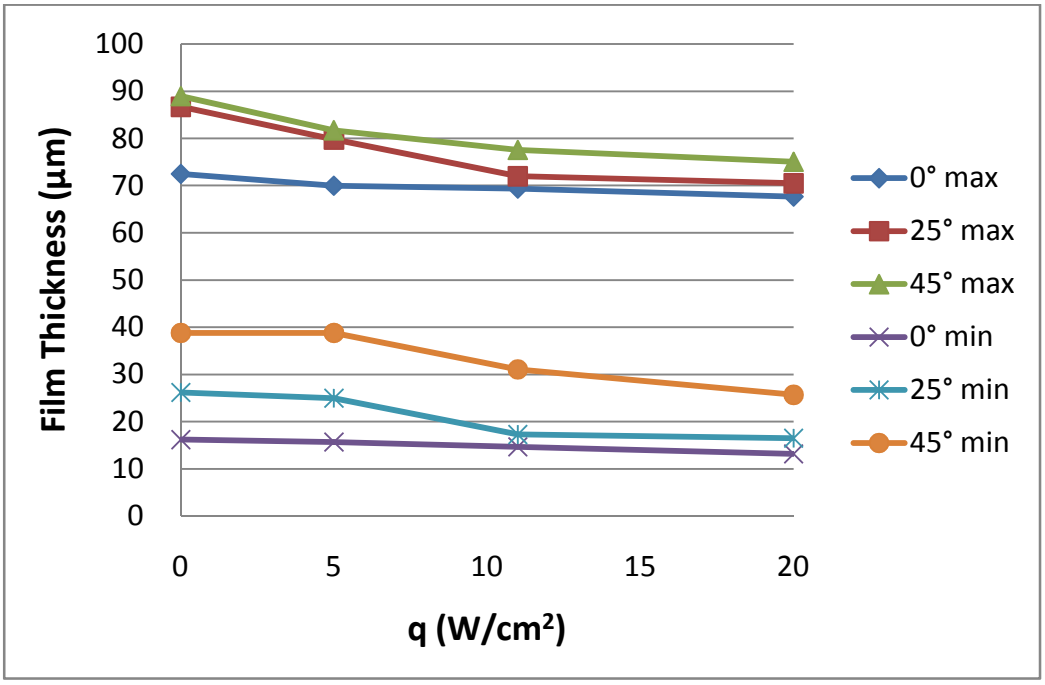

Figure 33 Maximum and minimum film thickness for different impact angle under different heat flux conditions 150 ml/hr, We=142

The film thickness is compared with the minimum temperature shown in Figure 21. It is found that 0° impact angle exhibits the lowest minimum surface temperature as well as the thinnest film thickness. The film thickness values are further compared with surface temperature data at different points. Temperature profiles at different points (orientations) are shown in Figures 34 to 36. Distances from impact center to the film thickness measurement points vary from 340 μm to 360 μm for different orientations. For the 0° impact angle, it can be seen that the temperature is identical for every horizontal orientations (horizontal angle). For impact angles greater than 0°, the temperature distribution shapes vary significantly as impact angle increases. The lowest surface temperature occurs at 0° (horizontal angle), which is the downstream of the impact point. The temperature increases as the horizontal angle increases from 0° to 90° as seen in Figures 34 to 36.

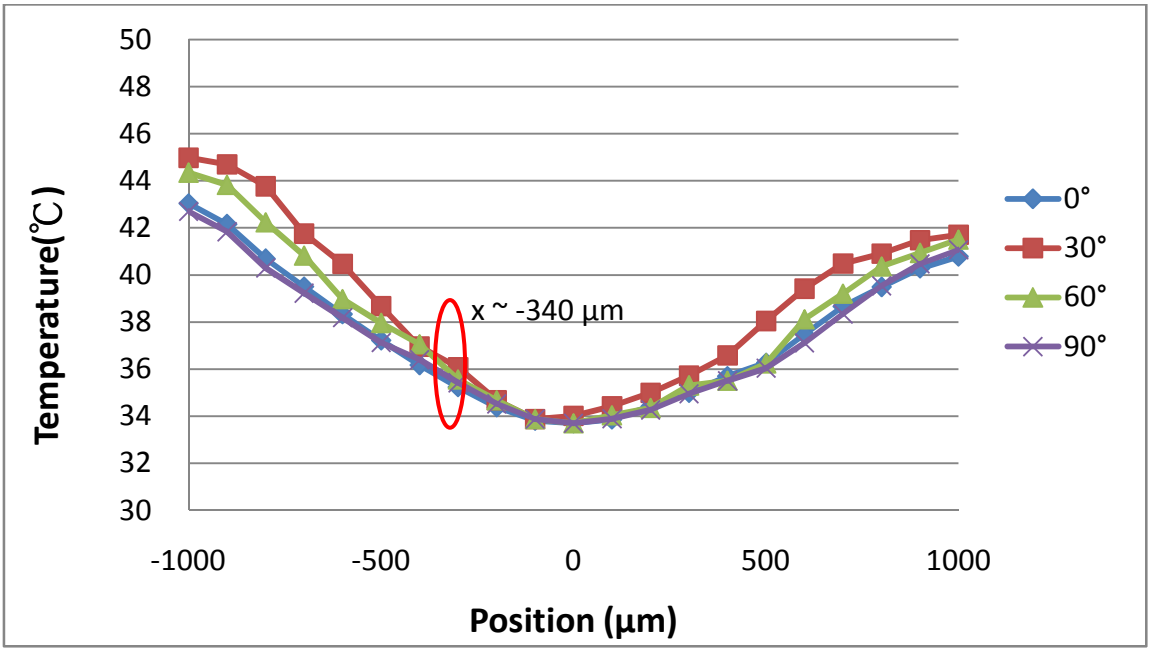

Figure 34 Temperature distribution along different horizontal orientations at 0° impact, 11 W/cm^2, 150 ml/hr, We=142

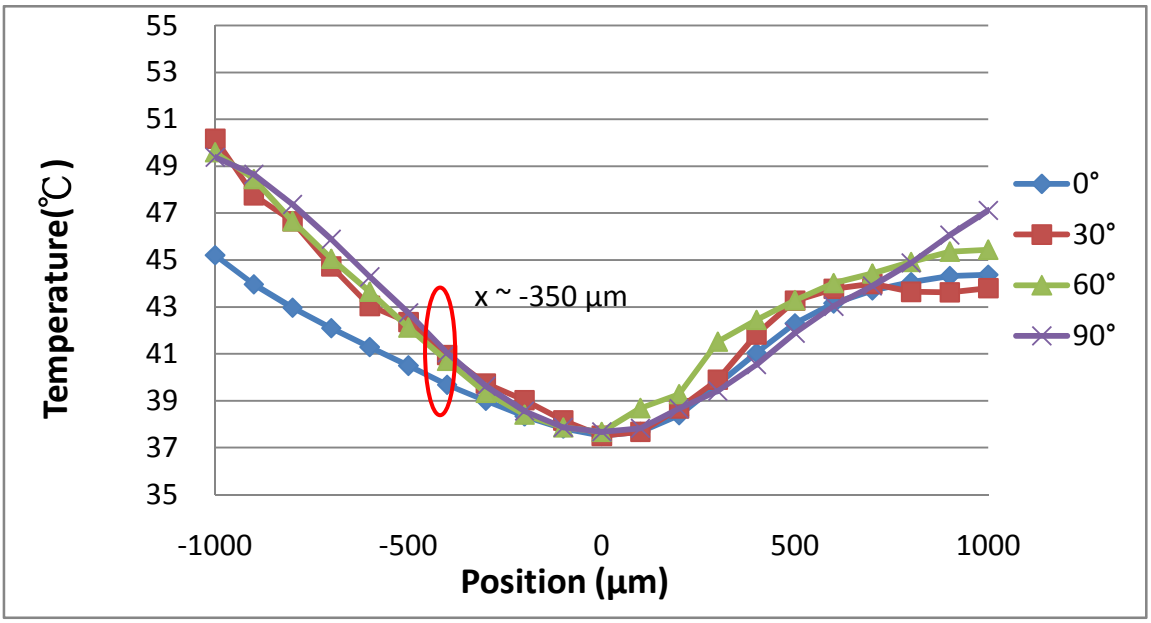

Figure 35 Temperature distribution along different horizontal orientations at 25° impact, 11 W/cm^2, 150 ml/hr, We=142

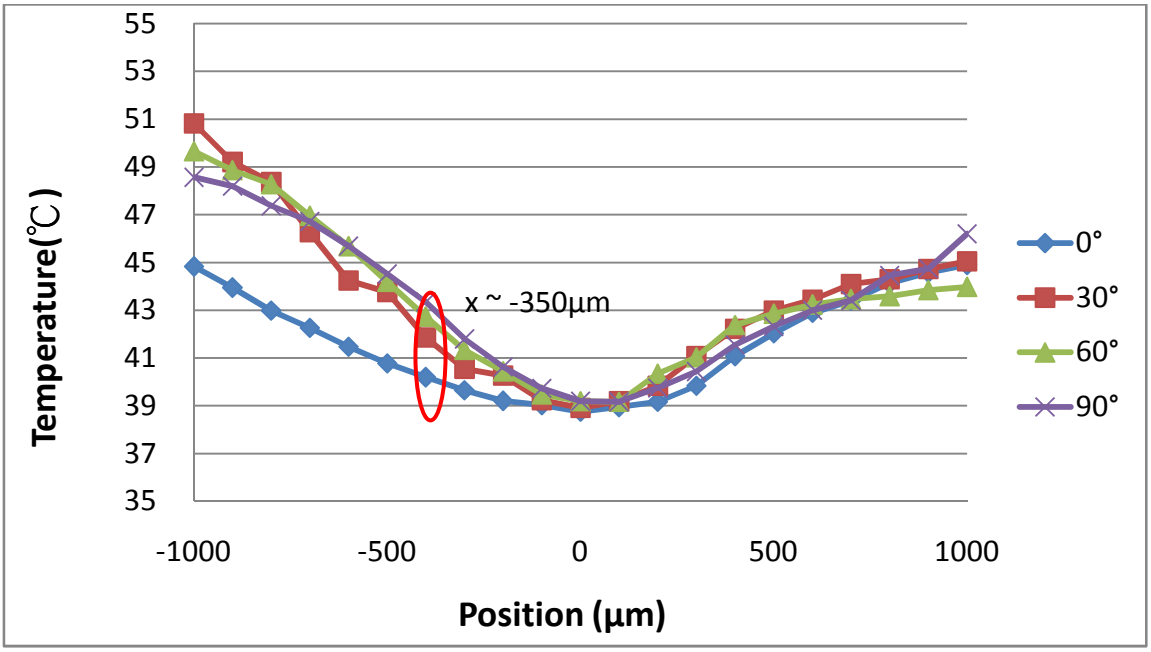

Figure 36 Temperature distribution along different horizontal orientations at 45° impact, 11 W/cm^2, 150 ml/hr, We=142

Figures 37 and 38 show the relation between film thickness and surface temperature at different orientations. Film thickness is found to be constant regardless of orientation (horizontal angle); however, temperature increases as horizontal angles increases for impact angles greater than 0°. This suggests that the tangential velocity depends strongly on horizontal angle since the flow rate and impingement frequency remain unchanged. Tangential velocity gradient and fluid momentum seem to reach a maximum value downstream from the impingement point. Moreover, since no vapor bubbles can be seen within the thin film region, it is evident that single phase forced convection is the main heat transfer mechanism at the surface which helps dissipate a large amount of heat keeping the surface temperature low. Therefore, the surface

temperature is found to be dependent on impact angle as well as the orientation around the impact point.

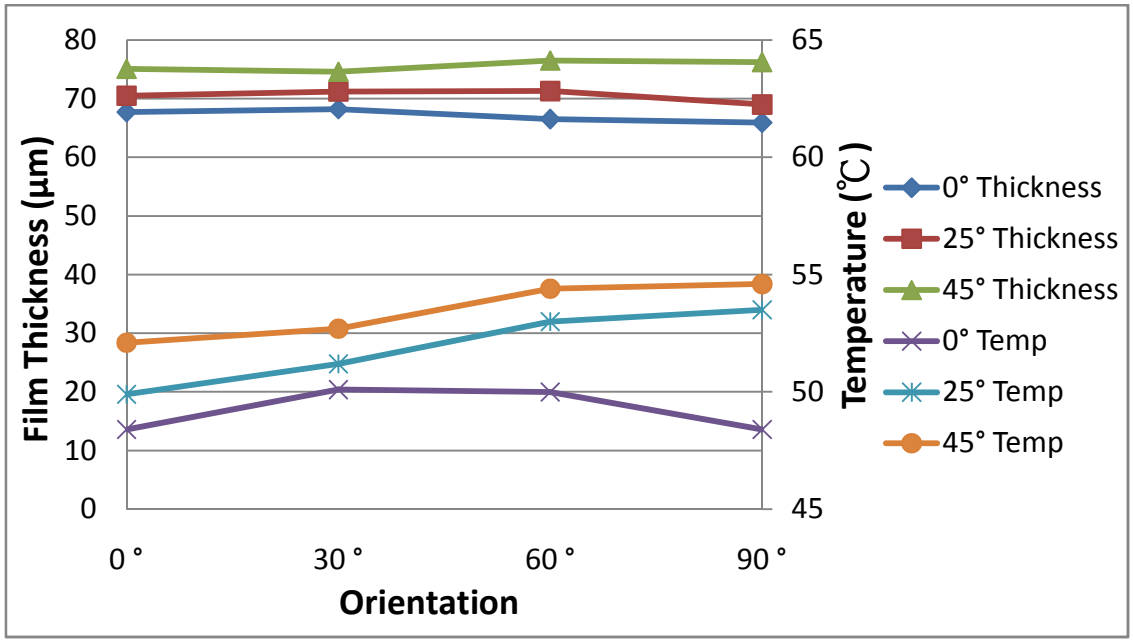

Figure 37 Maximum film thickness and surface temperature with respect to different horizontal orientations, 11 W/cm^2, 150 ml/hr, We=142

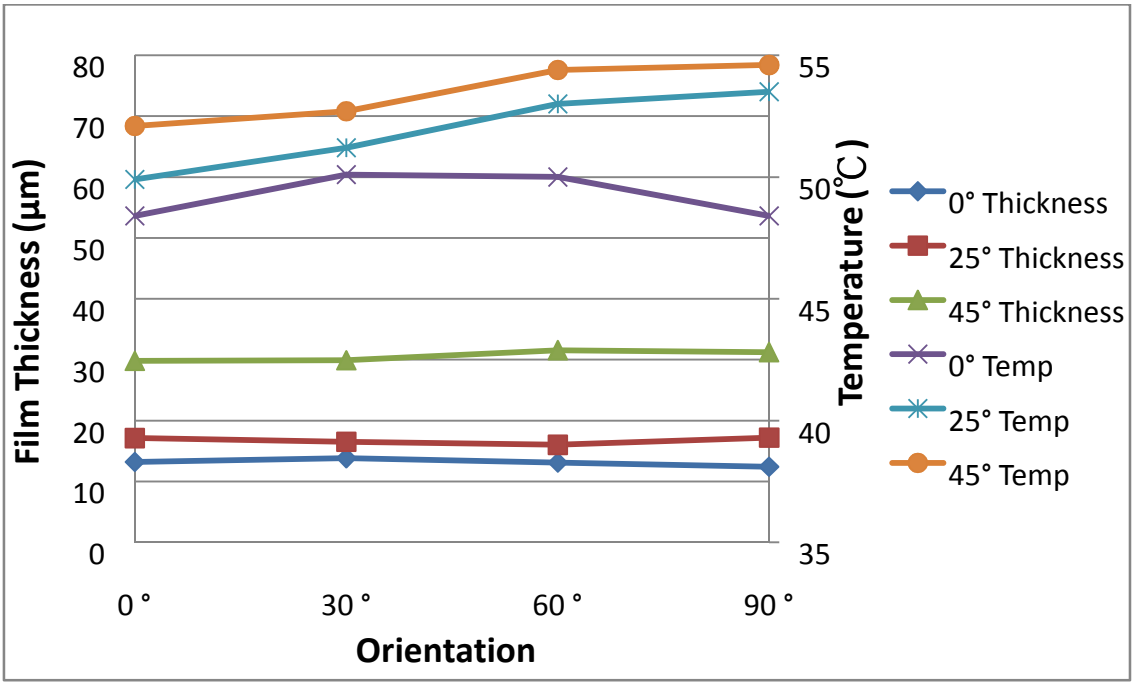

Figure 38 Minimum film thickness and surface temperature with respect to different horizontal orientations, 11 W/cm^2, 150 ml/hr, We=142

4.3. *Double streams results*

Double streams impact cooling experiments were performed using two different setups. The setup systems were described in detail in Section 3. Experimental results are presented in following sections.

4.3.1. Effect of two-dimensional spacing on surface cooling

The first setup consisted of two droplet generators, each with a single-hole orifice plate. The impact angle was fixed at 25°. Two different spacings S_1 (parallel to impact

direction) and S_2 (perpendicular to impact direction) were used as defined in Section 3. Crater images, minimum temperature and temperature distribution are presented for different S_1 and S_2 impact spacings.

4.3.1.1. Crater morphology and minimum temperature

Typical images for different S_1 and S_2 impact spacings are shown in Figures 39 and 40.

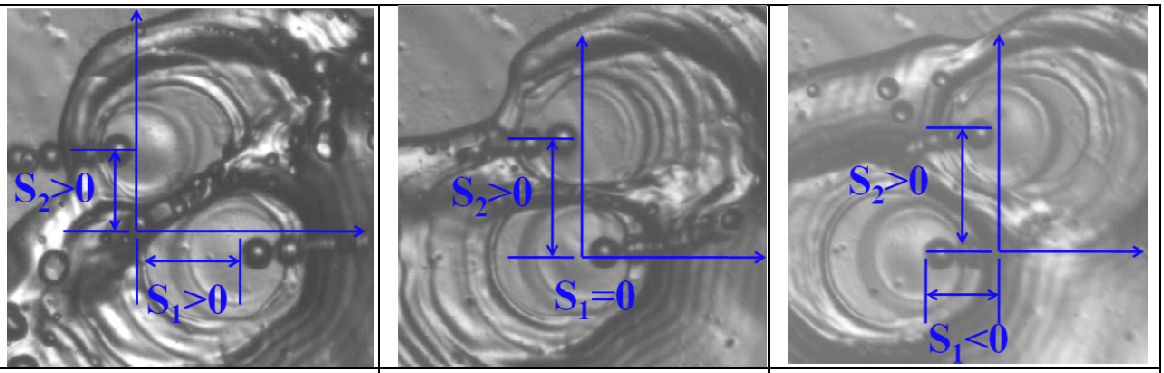

(a) (b) (c)

Figure 39 Typical bottom images for (a) positive S_1 spacing (b) zero S_1 spacing (c) negative S_1 spacing under fixed S_2 spacing, 23W/cm^2, 150 ml/hr, We=142

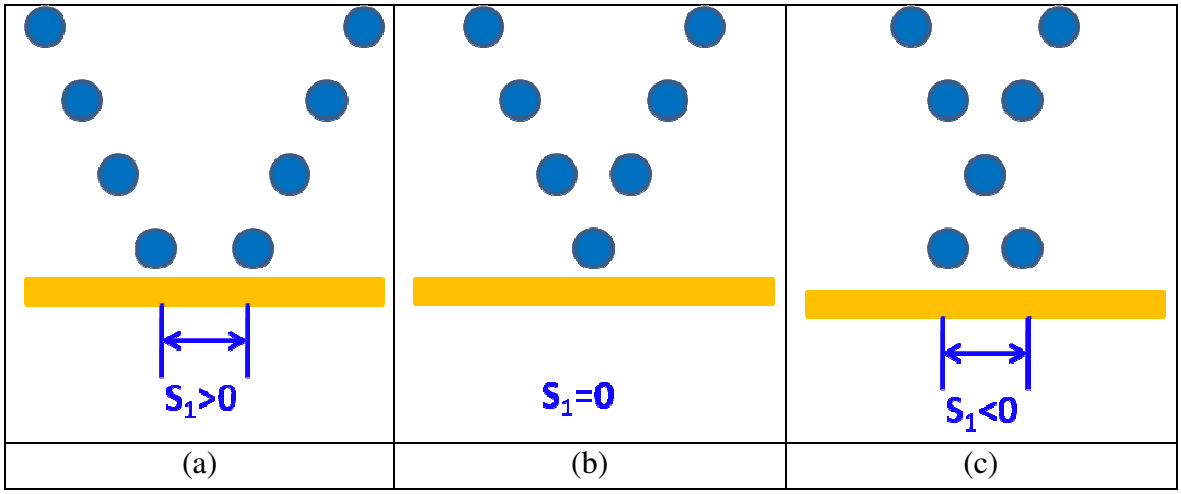

Figure 40 Typical side images for (a) positive S_1 spacing (b) zero S_1 spacing (c) negative S_1 spacing under fixed S_2 spacing, 23 W/cm^2, 150 ml/hr, We=142

Craters deformation is found to be most noticeable when S_1 spacing is positive (Figure 39a) since it results in a direct collision between the two adjacent impact craters. Minimum surface temperature as a function of S_1 and S_2 are shown in Figure 41. It can be seen that minimum temperatures are reached when at zero or negative values of S_1 (droplets fall across each other) because minimal fluid collision occurs. Temperatures are higher at small S_2 and positive S_1 spacings. The higher temperature at positive S_1 may due to the fluid collision caused by the opposing flow. Furthermore, S_2 at 800 μm and 1000 μm exhibit similar temperature data. It can be concluded that the minimum temperature is reached when S_1 is at 0 μm and is independent of S_2 at values of 800 μm or greater. This part of the study helped identify that S_1 should be at the zero and S_2 should be varied from 400 μm to 2400 μm to achieve the best heat transfer performance when using double streams of droplets.

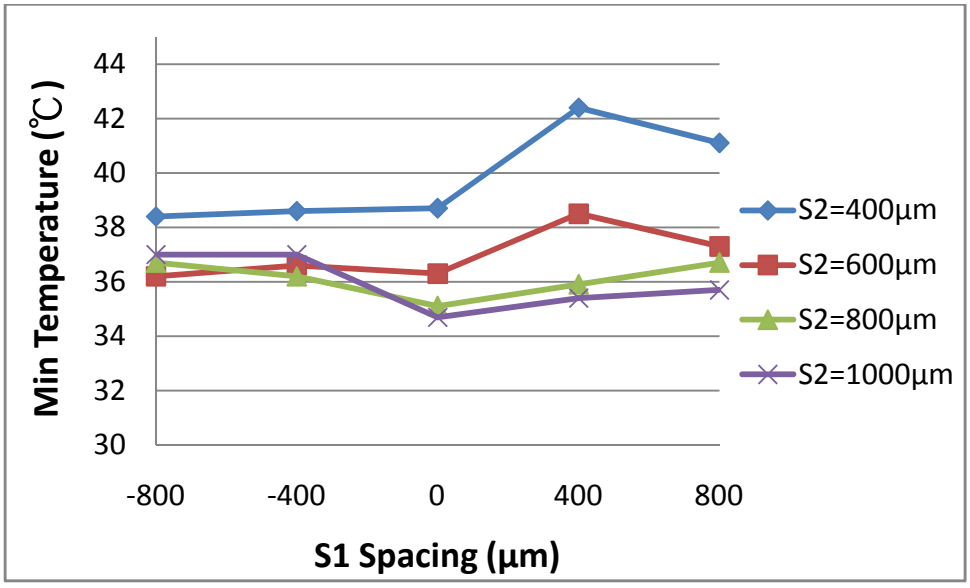

Figure 41 Minimum surface temperature with different S_1 and S_2 spacings at heat flux 23 W/cm^2, 150 ml/hr, We=142

For S_1 at 0 µm, S_2 was varied from 400 to 2400 µm. High speed images were taken both from the top and below of the surface as shown in Figures 42 and 43. It can be seen that when S_2 is at 400 µm, there is fluid collision between craters and some fluid is dissipated through the splashing. This explains why higher temperatures are observed for S_2 at 400 µm as seen in Figure 41. It can also be seen that craters are squeezed and deformed at small S_2. The size of the crater becomes independent when S_2 is larger than 800 µm. This implies that minimum surface temperature inside the crater should become independent of spacing at values larger than 800 µm as corroborated by temperature readings presented in the next section.

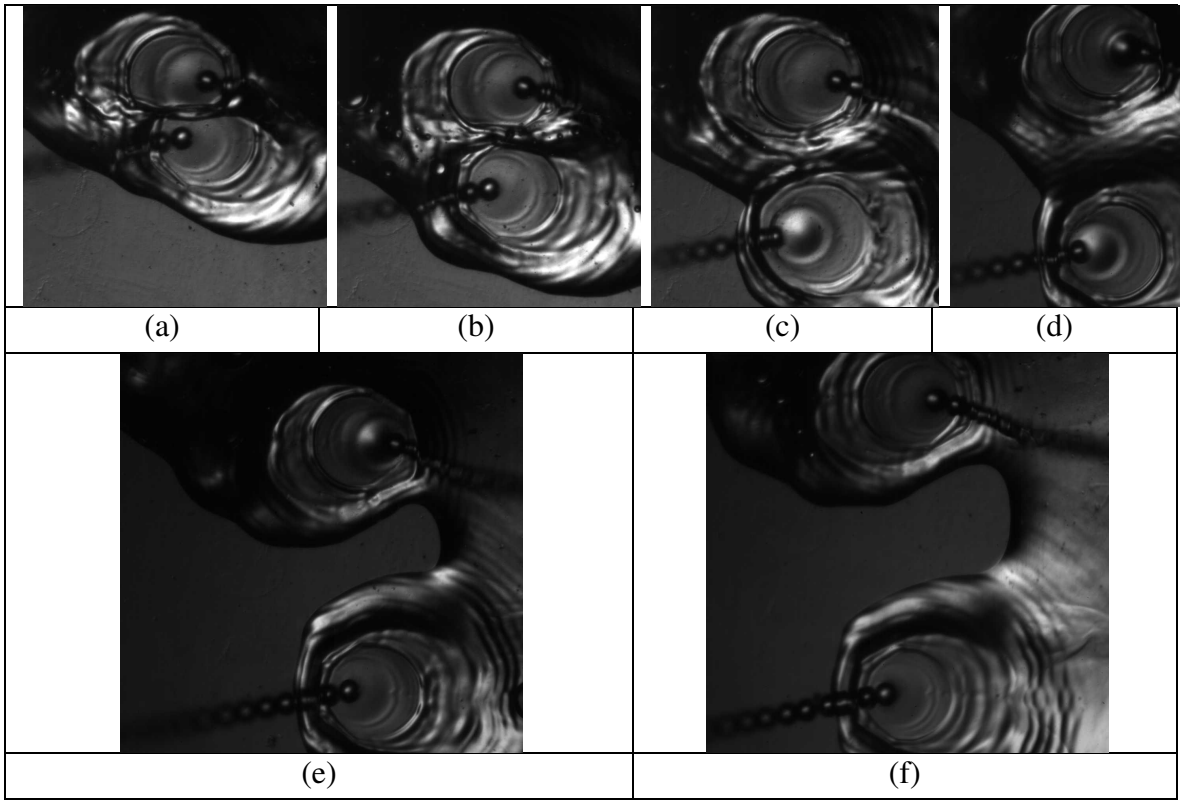

Figure 42 Bottom images for impact spacing (a) 400 μm (b) 800 μm (c) 1200 μm (d) 1600 μm (e) 2000 μm (f) 2400 μm at flow rate 150 ml/hr, heat flux of 23 W/cm^2

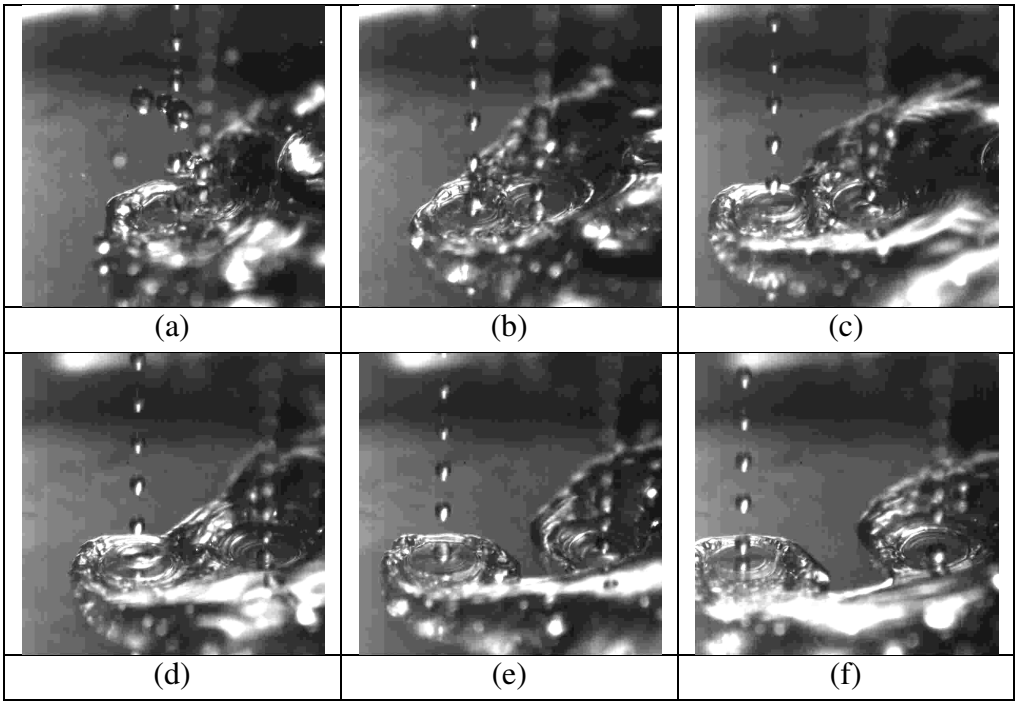

Figure 43 Top view images for spacing (a) 400 μm (b) 800 μm (c) 1200 μm (d) 1600 μm (e) 2000 μm (f) 2400 μm at flow rate 150 ml/hr, heat flux of 23 W/cm^2

Observations were also made at a flow rate of 200 ml/hr and compared as shown in Figure 44. It can be seen that the boundary of the crater appears to be more chaotic, and more entrained air bubbles are found around the crater due to the large flow rate (velocity). Also, a stronger collision between adjacent crater walls is evident at higher flow rate. The well-formed crater is observed when the S_2 is larger than 1200 μm at 200 ml/hr. This confirms that flow rate and fluid momentum have a great effect on crater size and crater deformation.

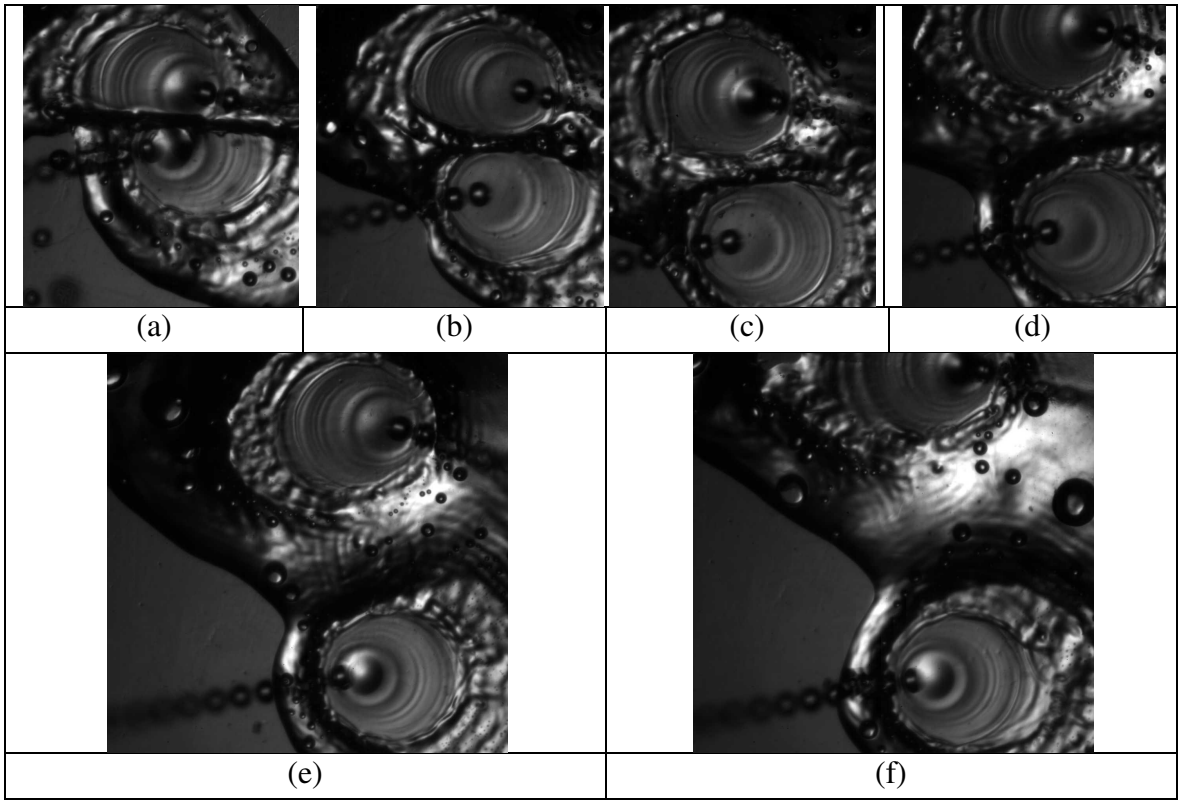

Figure 44 Images for impact spacing (a) 400 μm (b) 800 μm (c) 1200 μm (d) 1600 μm (e) 2000 μm (f) 2400 μm at flow rate 200 ml/hr, heat flux of 23 W/cm^2

It is worth noting that for flow rate of 150 ml/hr, fluid dry out occurs between adjacent craters when the impact spacing increases to 2000 μm as seen in Figures 42e and 42f. However, there is no dry out at flow rate 200 ml/hr for the same spacing and heat flux condition. Therefore, flow rate and spacing are found to be critical physical variables that have a direct effect on the formation of a dryout. Temperature data are presented in the next section which is used to understand the effect spacing and flow rate on the dryout region and heat transfer performance.

4.3.1.2. Temperature distribution profile

Temperature profiles were obtained by using the lowest temperature within each impact crater and perpendicular to the droplet impact direction. Temperature profiles for different spacings at heat flux of 23W/cm^2 are shown in Figure 45. For every spacing case, the minimum temperature is always lower at higher flow rate. The results agrees with Soriano's [25] single stream vertical impingement experiments. He claimed that the surface temperature is dominated mainly by flow rate.

For fixed flow rate, the minimum temperature reduces as the impact spacing increases, and reaches nearly a constant value after a critical spacing value is reached (1200 μm for flow rate 150 ml/hr or 1600 μm at 200 ml/hr flow rate). The temperature data is in good agreement with the crater images captured from below. It is also found that when the impact crater is formed without any deformation or interaction with any neighboring impact crater, the minimum surface temperature is independent of impact spacing.

If the temperature profiles shown in Figure 45 are observed closely, it is evident that after certain spacing has been reached, two local temperature minima appear corresponding to the impact points of two adjacent droplet streams. To further understand the effect of spacing on surface temperature, two variables are defined where T_{max} represents the local maximum temperature between two craters and T_{min} represents the minimum temperature at the impact point. ΔT is defined as the difference between T_{max} and T_{min}. Each variable is clearly shown in Figure 46. Figure 47 shows how ΔT varies with spacing. It can be seen that temperature difference increases as the impact

spacing increases. Since T_{min} remains constant as spacing and ΔT increase, obviously T_{max} increases monotonically with spacing. This suggests that the heat transfer process (i.e. two-phase flow phenomena) taking place in the region between craters is different from the heat transfer process taking place in the thin film region which is assumed to be a single phase forced convection mechanism.

When dryout occurs, the temperature increases rapidly which causes large temperature variation within the surface. Moreover, the temperature difference (ΔT) is smaller for larger flow rates. This indicates that larger flow rate can provide higher heat transfer rate and ensure a uniform temperature distribution within the impact zones.

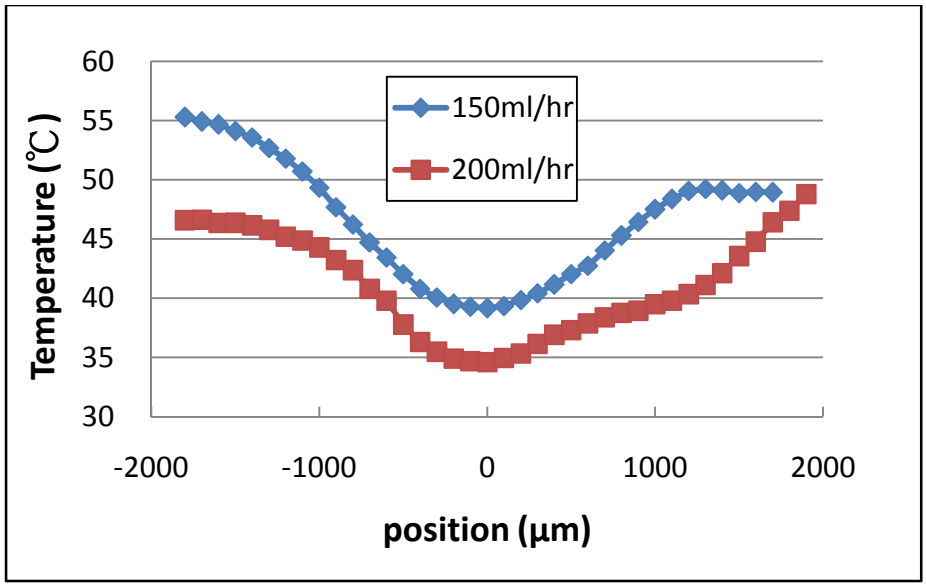

(a)

Figure 45 Temperature profiles for S_2 spacing (a) 400 µm (b) 800 µm (c) 1200 µm (d) 1600 µm (e) 2000 µm (d) 2400 µm at 150 and 200 ml/hr, heat flux of 23 W/cm^2

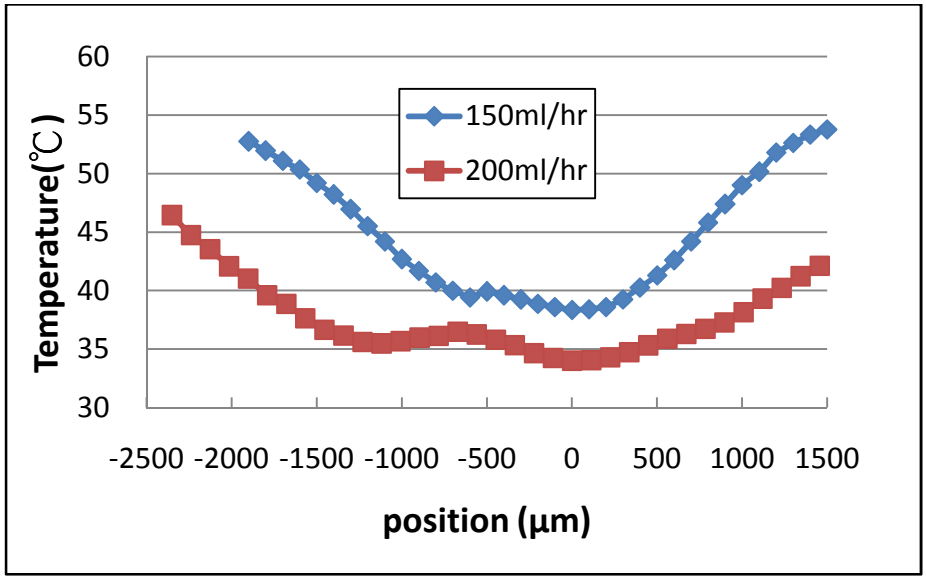

(b)

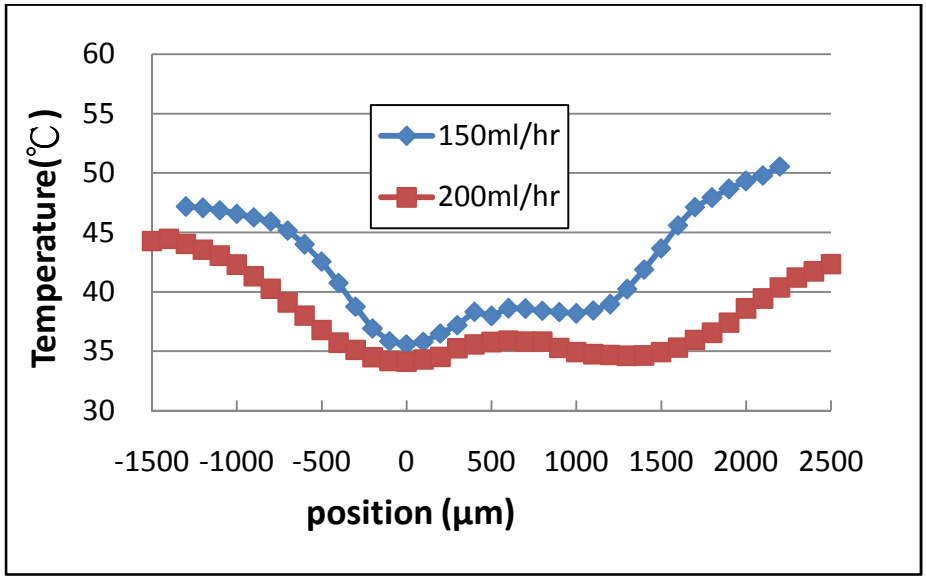

(c)

Figure 45 Continued.

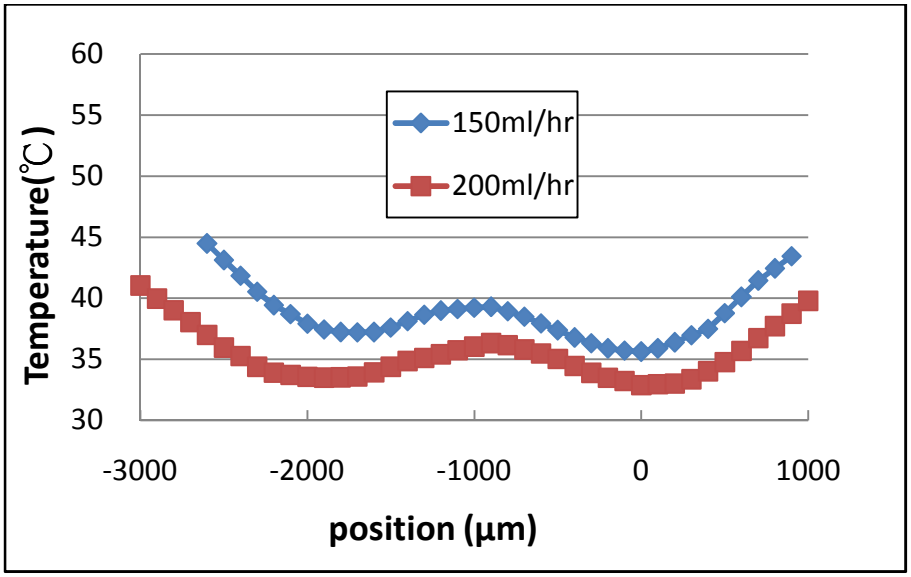

(d)

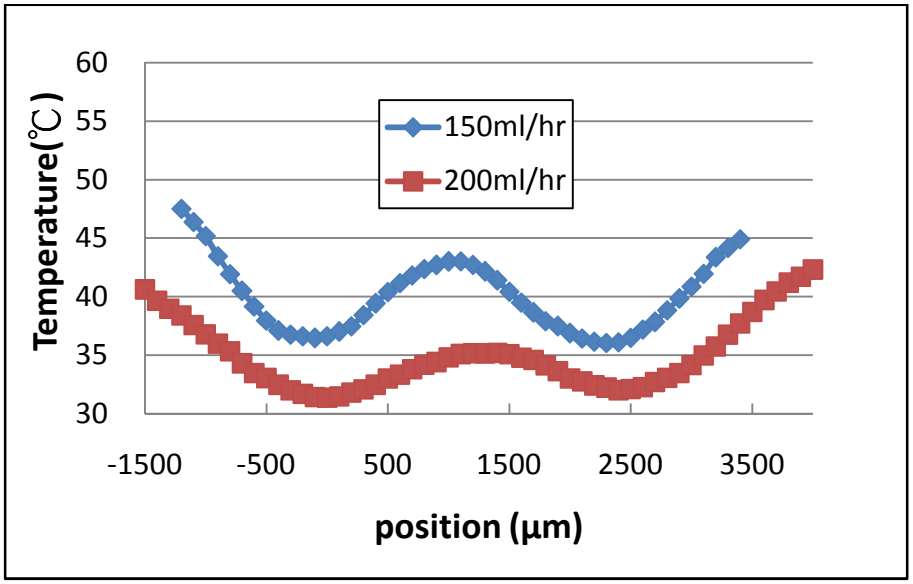

(e)

Figure 45 Continued.

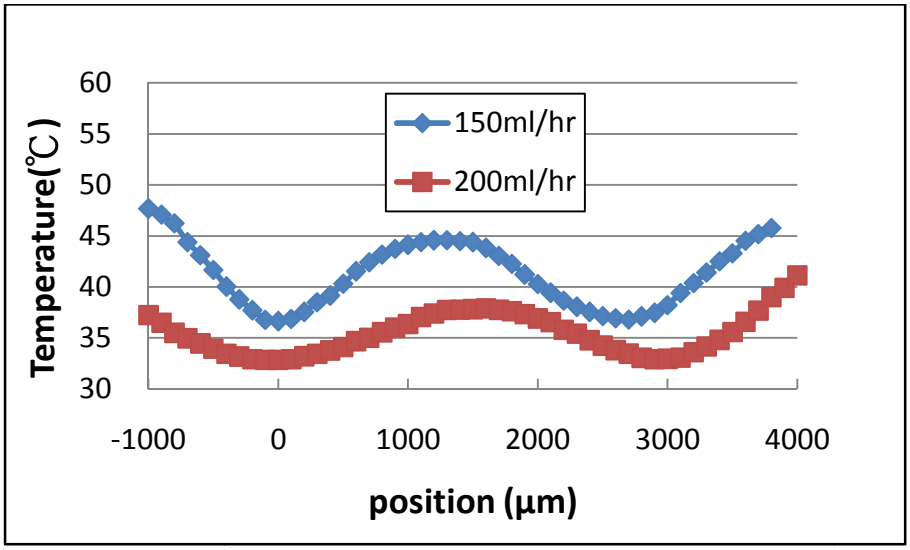

(f)

Figure 45 Continued.

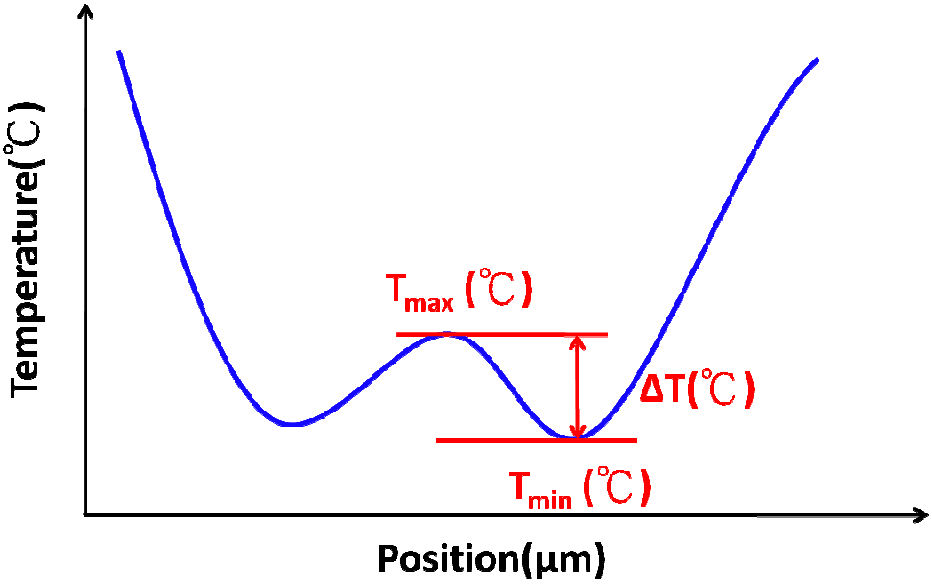

Figure 46 Definition of local maximum temperature, minimum temperature and temperature difference for double stream impact temperature profile

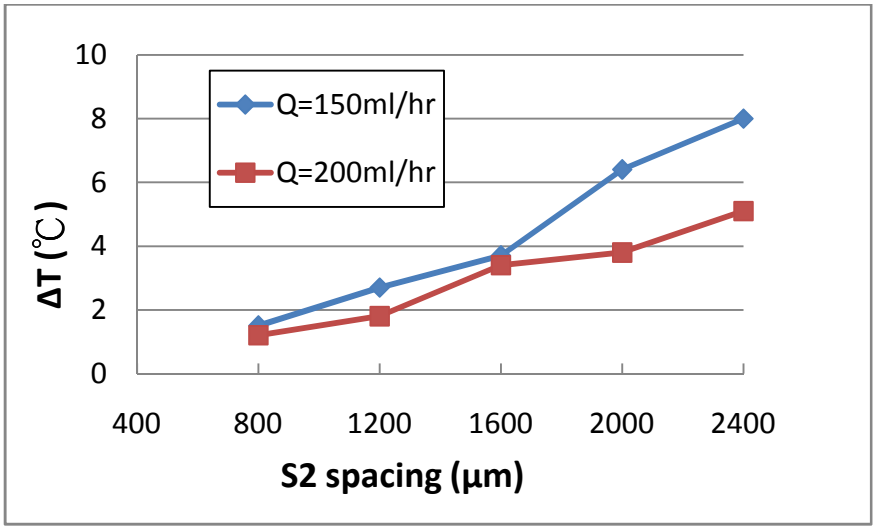

Figure 47 Temperature difference for different spacings

In electronic cooling, it is necessary to keep the low minimum surface temperature while maintaining the uniform temperature distribution to avoid component damage, so that's why it is important to reduce ΔT as much as possible. Therefore, an optimum spacing between adjacent droplet streams should be sought that would result in low ΔT and low T_{min}. Visual observations have revealed that smaller spacing results in fluid collision and higher minimum temperature. On the other hand, larger spacing results in lack of fluid coverage which leads to large temperature variation not tolerable or acceptable in some electronic cooling that could lead to dryout under certain conditions.

Finding the optimum droplet impact spacing is critically important to effectively manage thermal loads. In the past, different studies have revealed that contradictory results including that in some cases sparse sprays perform better than dense sprays and viceversa. Horacek et al. [9] claimed that sparse sprays provide more uniform heat

transfer within the array of heaters. Chen et al. [10] claimed that for the fixed flow rate, as droplet velocity increases and impact spacing increases, the heat flux increases. In other words, they claimed that sparse spray exhibits higher heat flux. In this study, sparse sprays (greater horizontal spacing) result in better heat transfer performance if the flowrate per droplet stream is increased. However, dense sprays (lesser horizontal spacing) perform better if the flowrate per stream is decreased. Therefore, dense and sparse sprays should be characterized thoroughly before indicating which performs better in spray cooling systems.

Mudawar et al. [11] claimed that heat flux depends on the wetted area rather than the spray density. The result in this study agrees with their finding by showing that flow rate is directly related to heat transfer rate. As flow rate increases, the optimum spacing increases and heat transfer enhances as well.

4.3.2. Effect of one-dimensional spacing and impact angle on surface cooling

In the previous section, it became evident that only spacing in the S_2 direction was an important variable. Moreover, from the previous experimental results, splashing occurred when horizontal spacing (S_2) was at or below 400 μm. On the other hand, the height of the contiguous liquid wall reduced when spacing was at 800 μm or greater. Splashing is commonly seen in spray cooling and it is the reason for the low cooling efficiency [12]. When horizontal spacing is increased from 400 μm and 800 μm a transition between spreading-splashing and complete spreading mode takes place which it is worth investigating in future studies to understand its role in cooling efficiency

enhancement [25]. The impact spacing and impact angle were studied simultaneously to determine their effects on film thickness and surface temperature.

The impact images were captured by the high speed camera in two ways. The first view was from the top of the surface at a 35° inclination angle. The second view was from below using a 45° mirror. Figure 48 shows the typical double streams impact images. Two independent variables were used in the study: Impact spacing and impact angle. The impact spacing was varied from 330 to 650 μm and the impact angle was varied from 0° to 45°.

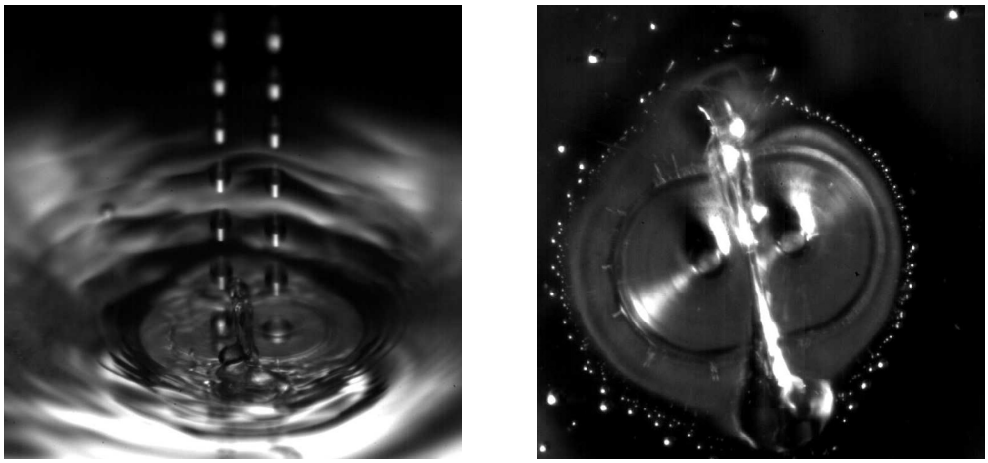

(a) (b)

Figure 48 Typical double streams images from (a) top (b) below the surface without heat flux condition

4.3.2.1. One-dimensional impact spacing effect

In order to study the spacing effect within the transition region (400 – 800 μm), the horizontal impact spacing of 330 μm, 550 μm, and 650 μm were considered. The

images from top and below the surface are shown in Figures 49 and 50. It can be seen that splashing occurs at a small spacing of 330 μm. The level of splashing is reduced and transformed to more complete droplet spreading as spacing increases. Craters are deformed for all three spacing cases as seen in the figures; however, the crater deformation becomes less pronounced and the impact area increases as the impact spacing increases.

	S_2= 330 μm	S_2= 550 μm	S_2= 650 μm
q= 0 W/cm^2	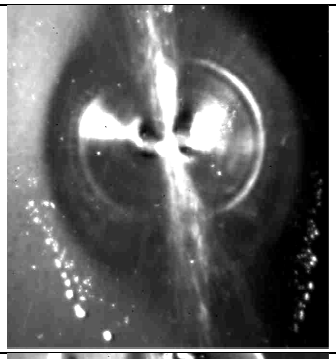	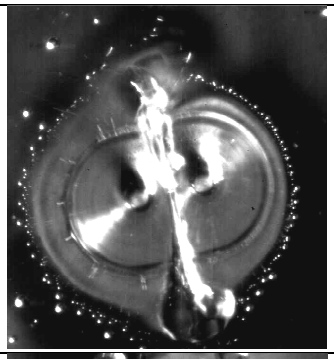	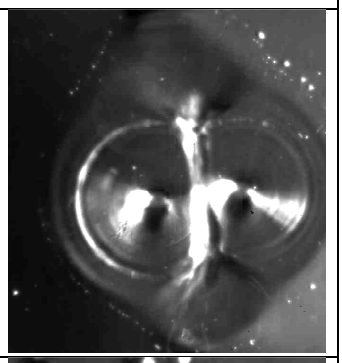
q= 23 W/cm^2		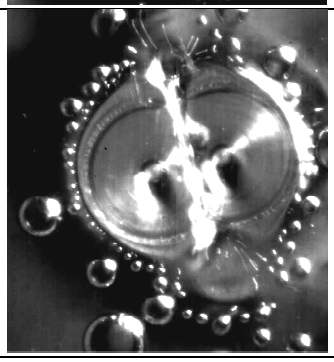	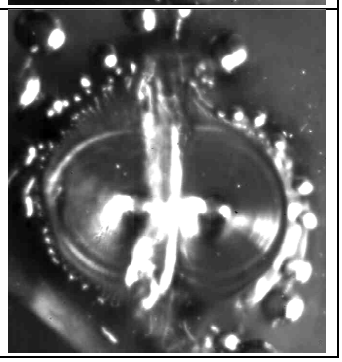

Figure 49 Impact images of double droplet streams from below for spacing 330 μm, 550 μm and 650 μm, 150 ml/hr, We =142

	S_2= 330 μm	S_2= 550 μm	S_2= 650 μm
q= 0 W/cm^2		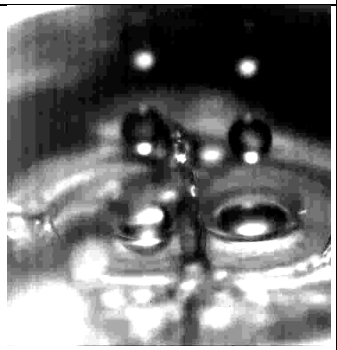	
q= 23 W/cm^2	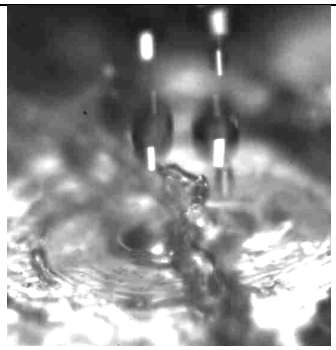		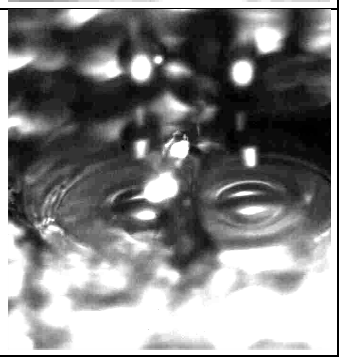

Figure 50 Impact images of double droplet streams from top for spacing 330 μm, 550 μm and 650 μm, 150 ml/hr, We =142

The heat transfer data of different spacings are shown in Figure 51. Figure 51 shows that minimum wall temperature is higher at smaller impact spacing. Images from the top shows that some of the impact crater was deformed, collided and splattered into the ambient air for small spacing cases. As the impact spacing increases, the level of splashing gradually diminishes into complete spreading. As seen in previous studies, spreading mode results in the reduction of minimum temperature [25]. All the observations indicate that when the spacing is larger than 800 μm, each impact crater is well formed and the impinging droplets completely spread on the surface. At that point, the temperature within the crater is no longer affected by the adjacent crater.

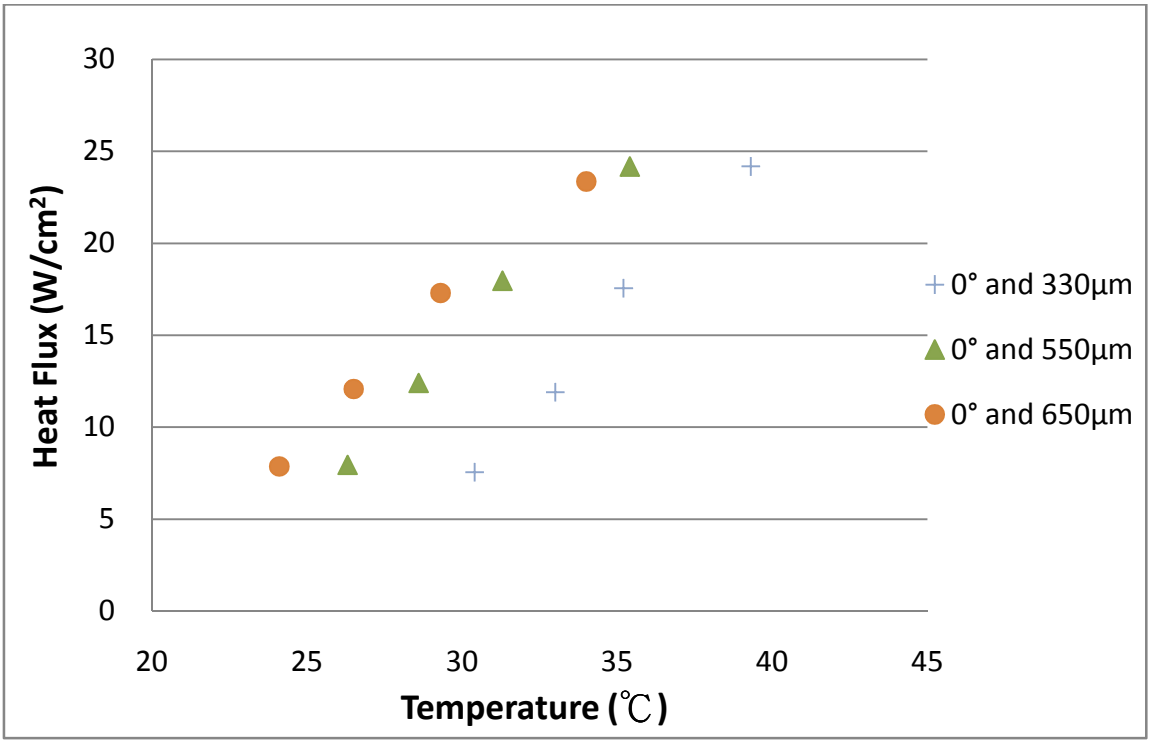

Figure 51 Minimum wall temperature of double droplet stream with different 0° impact spacings under different heat flux conditions

One-dimensional temperature profile across two adjacent impact centers was obtained as shown in Figure 52. It is observed that at spacing of 650 μm exhibits the lowest temperature. Also, the temperature curve is flatter within the impact region at larger spacing. As seen in Figure 49, there is less deformation of the impact craters at spacing 650 μm compared to the smaller spacings. Droplets can be spread out with less collision and form a thinner film all the way around the impact point. Therefore, thinner fluid film results in lower temperature distribution within the impact area.

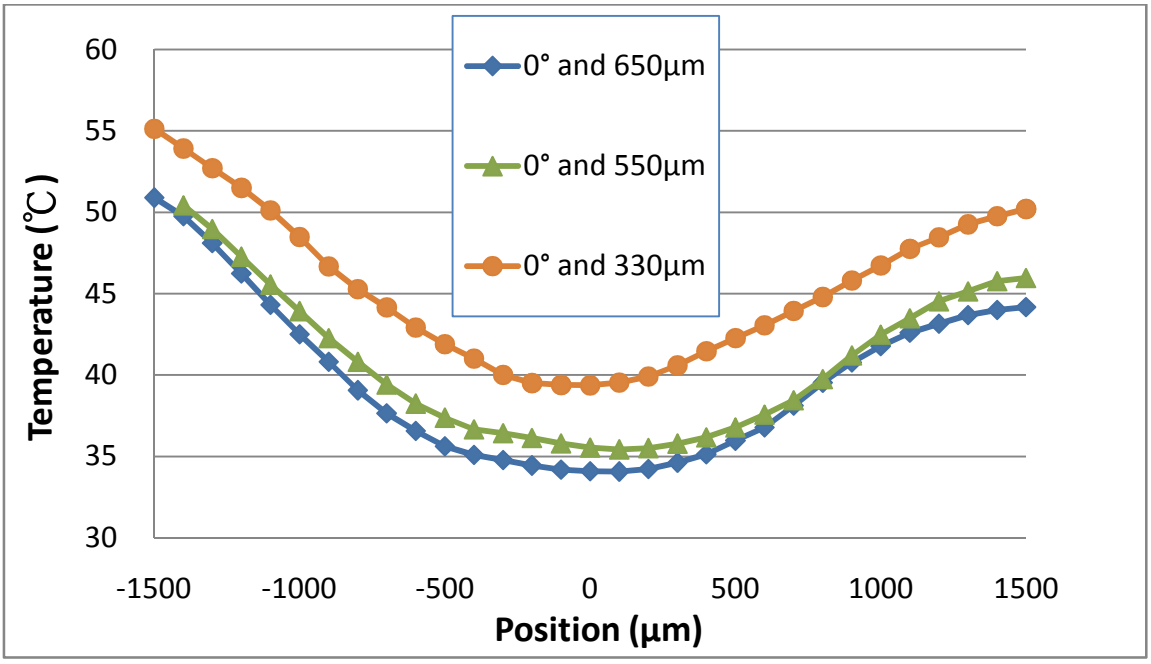

Figure 52 Temperature distribution for double streams with different impact spacings

Temperature values at different horizontal orientations within the crater were also obtained. Three temperature profile lines along each orientation were obtained as shown in Figure 53. Positive positions of x-axis represent the points between the impact points while negative positions represent the points away from the impact points.

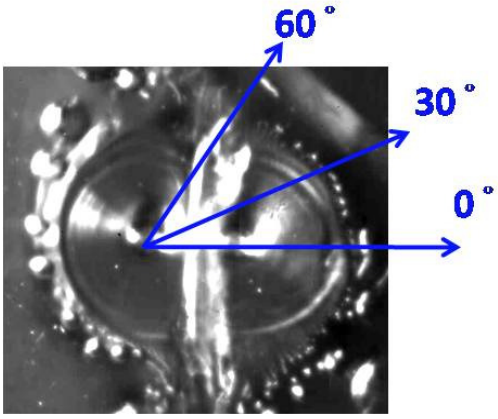

Figure 53 Different temperature line orientations

Figure 54 shows three different temperature profile lines for the orientations shown in Figure 53.

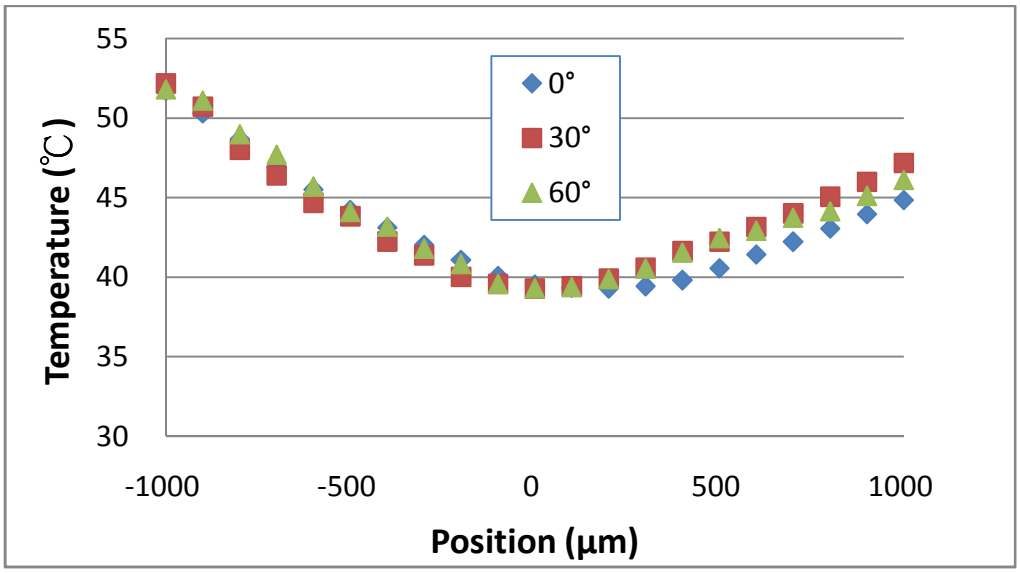

(a)

Figure 54 Temperature distribution at different horizontal orientations at S_2 of (a) 330 µm (b) 550 µm (c) 650 µm

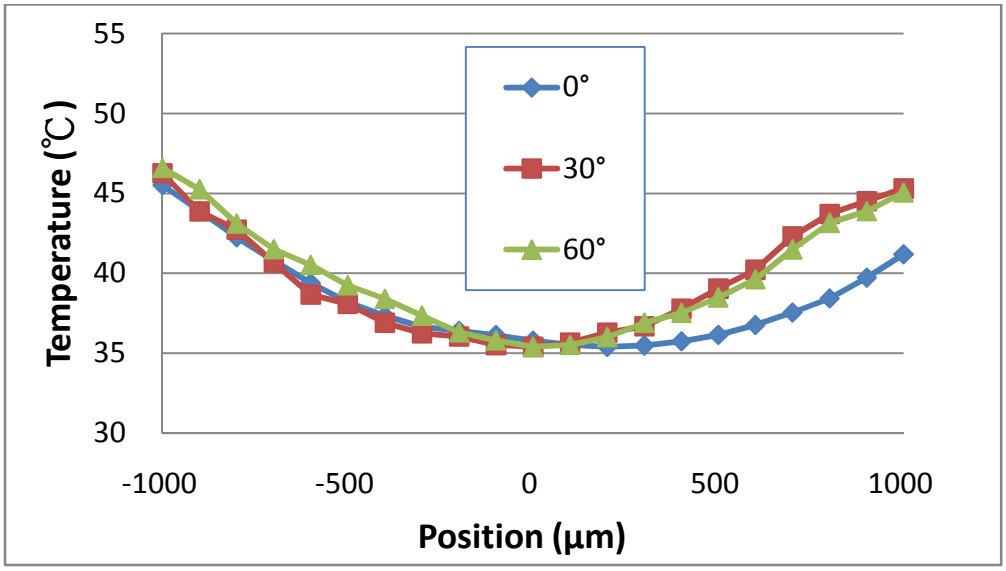

(b)

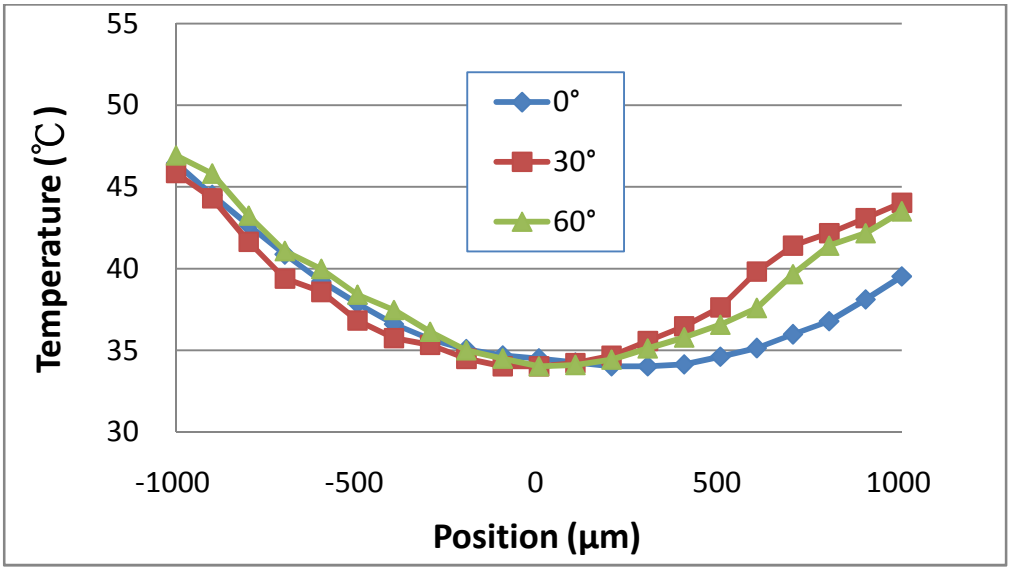

(c)

Figure 54 Continued.

For each impact spacing case, the temperature profile away from the impact point exhibits similar trend since it is not affected by the neighboring impact crater. This

implies that the temperature is independent of horizontal orientation (0°, 30°, and 60°) when away from the impact point. However, in the positive direction (between droplet impact zones) as shown in Figure 54, shows different temperature distribution at different horizontal orientations. At 0° horizontal orientation exhibits the best heat transfer due to the cooling effect from the adjacent impact. At 30° and 60° horizontal orientations show higher temperature distribution than at 0° horizontal orientation which can be attributed to lower fluid velocities at the surface since film thickness seems to less dependent on orientation. Temperature between impact points seems to be affected not only by the impact spacing, but also by horizontal orientation and the resulting velocity field. Analysis of the fluid dynamic is complicated specially when imaging the area between two impact craters. Therefore, fluid velocity should be further investigated using other technique such as micro particle image velocimetry (μPIV) to fully explain the temperature distribution within the impact area.

4.3.2.2 Effect of double stream impact angle on surface cooling

For the impact angle experiments, impact spacing was fixed at 550 μm and impact angle was varied from 0° to 45° with respect to the vertical direction of the surface. A single droplet generator with a two-orifice plate was used during the experiment. Therefore, two droplet streams impacted the surface in a way that the droplets of the second stream always fell on to the downstream side of the first stream droplets. Images from top and below the surface are shown in Figures 55 and 56. It is observed that impact crater is chaotic and not well defined for 45° impact angle when no

heat flux was applied. The fluid is chaotic for 45° impact angle because of two main reasons: First, impact droplets lack vertical momentum; thus, the fluid is unable to form a well defined thin film region and a clear crater boundary. Second, the downstream impact area is affected by the upstream fluid. Fluid flow from downstream is disturbed by the upstream flow. When heat flux is applied, the boundary of impact crater becomes clearer. It is mainly due to a reduction in the fluid surface tension with respect to the temperature. The fluid film within the crater spreads out easier and forms a well defined crater at lower surface tension.

	θ = 0°	θ = 25°	θ = 45°
q= 0 W/cm^2	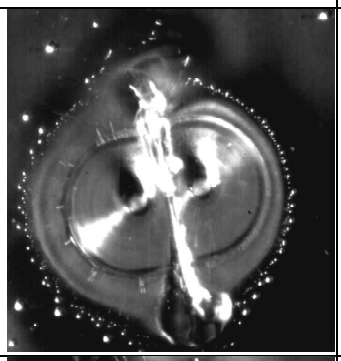	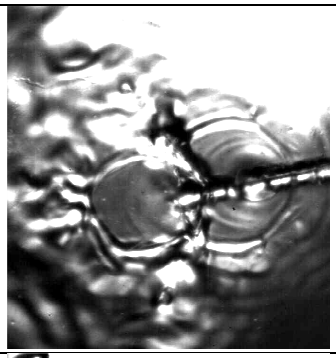	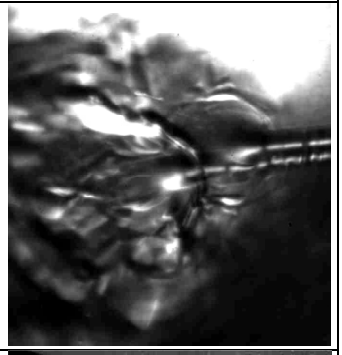
q = 23 W/cm^2	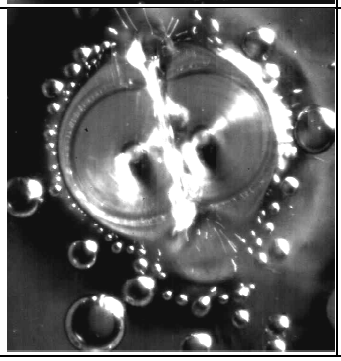	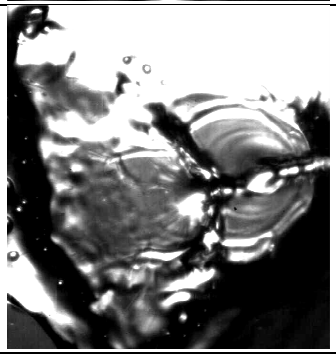	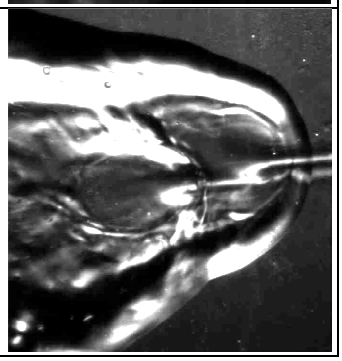

Figure 55 Impact images from below for impact angle with/without heat flux conditions

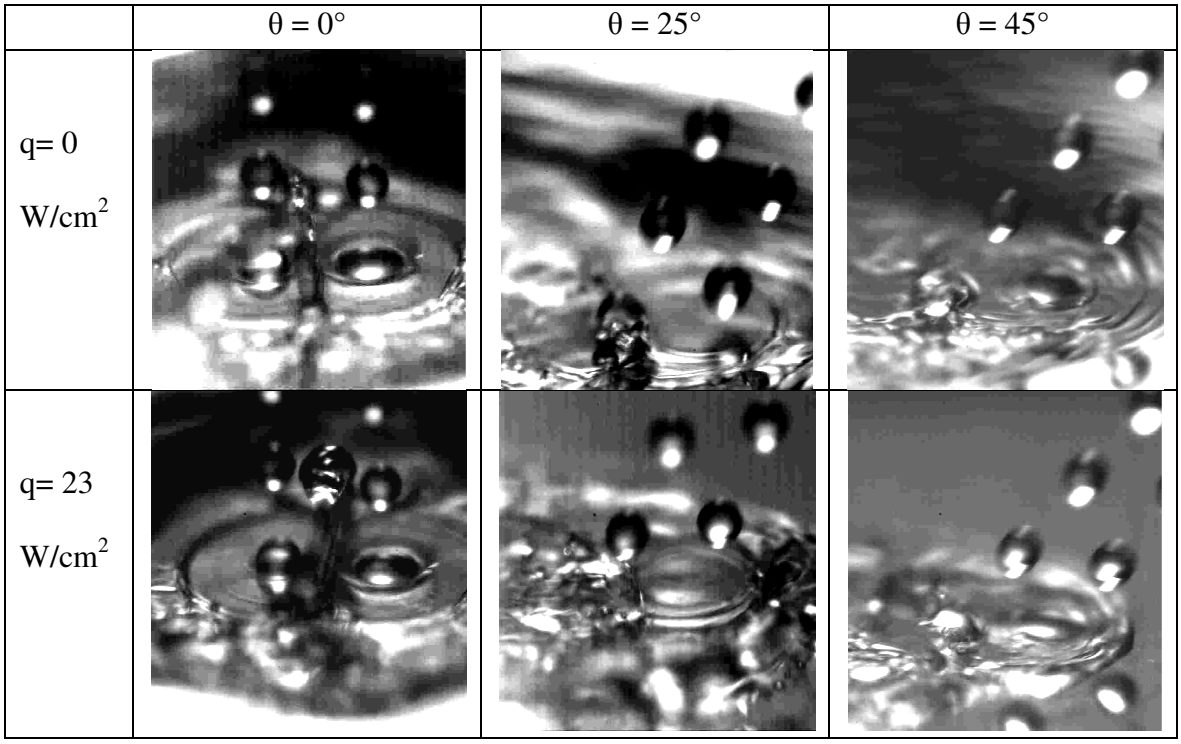

Figure 56 Impact images from top for impact angle with/without heat flux conditions

The heat transfer data of different impact angles are shown in Figure 57. The figure shows the minimum wall temperature with respect to different heat flux conditions. It is observed that at 25° impact angle exhibits slightly lower minimum wall temperatures than at 0° impact angle. The result is different from the single stream experiment which shows that the lowest minimum surface temperature always occurs at the 0° impact. The result can be explained by top view images as shown in Figure 56. There is fluid spreading and splashing between craters when the impact angle is 0° which impedes the fluid to form a well defined thin film region. At 25° impact angle, there is less fluid splashing between craters which can explain why the surface temperature is lower. As for the 45° impact angle case, it performs as well as the other

two cases (0° and 25°) in terms of exhibiting low surface temperature at low heat fluxes. However, at higher heat flux values, there is a clear effect of impact angle on surface temperature. Therefore, using an impact angle of 45° results in higher surface temperatures both when single and double streams are used indicating that the lack of vertical momentum is a dominant variable regardless of the number of droplet streams.

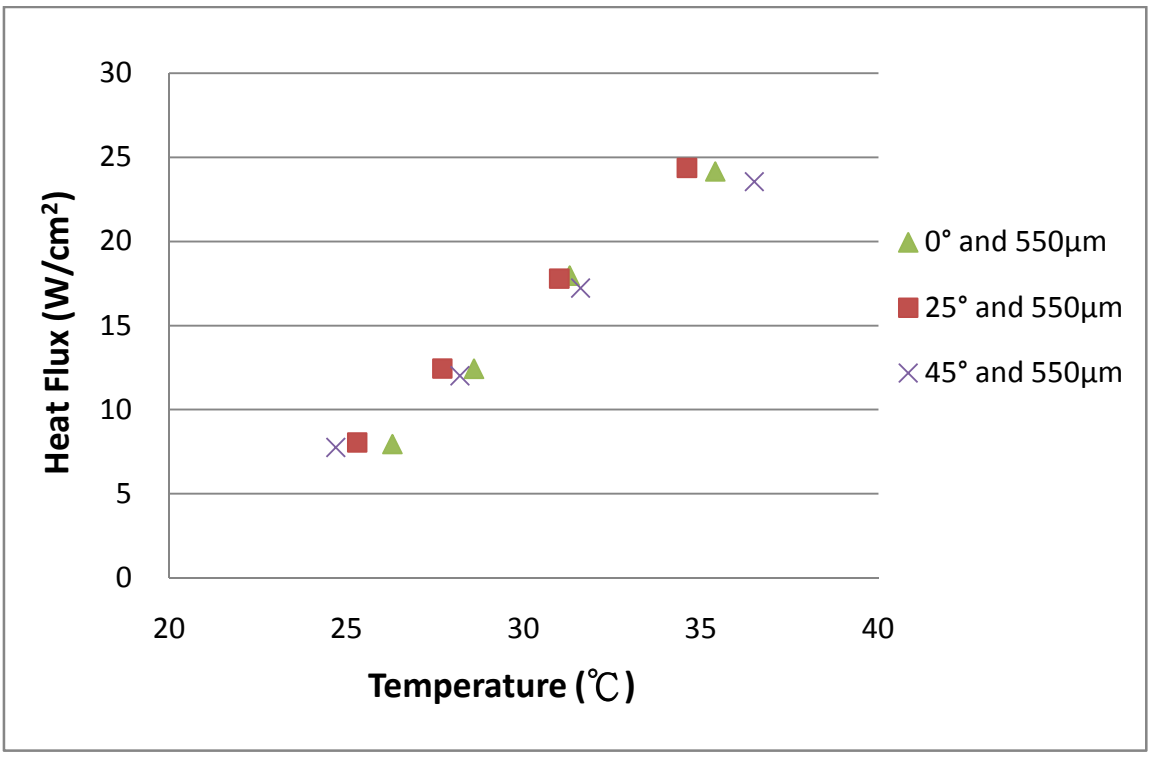

Figure 57 Minimum wall temperature of different impact angles for double streams under different heat flux conditions

Temperature values at different horizontal orientations within the crater were also obtained as in Figure 58. From the figure, temperature profile is symmetric for 0° impact angle. As the impact angle increases, the shape of the temperature curve changes

as shown in the figure which is attributed an unequal distribution of fluid velocity between the upstream and downstream sides. It is observed that temperature gradient is smoother on downstream side from the point of impact because greater tangential velocity is present which helps dissipate heat at that position. For an impact angle of 45°, the whole temperature distribution shift upwardly. However, when the impact angle is set to 25° and 45° impact, temperature profile exhibits a smaller temperature gradient (slope) than at 0° impact angle.

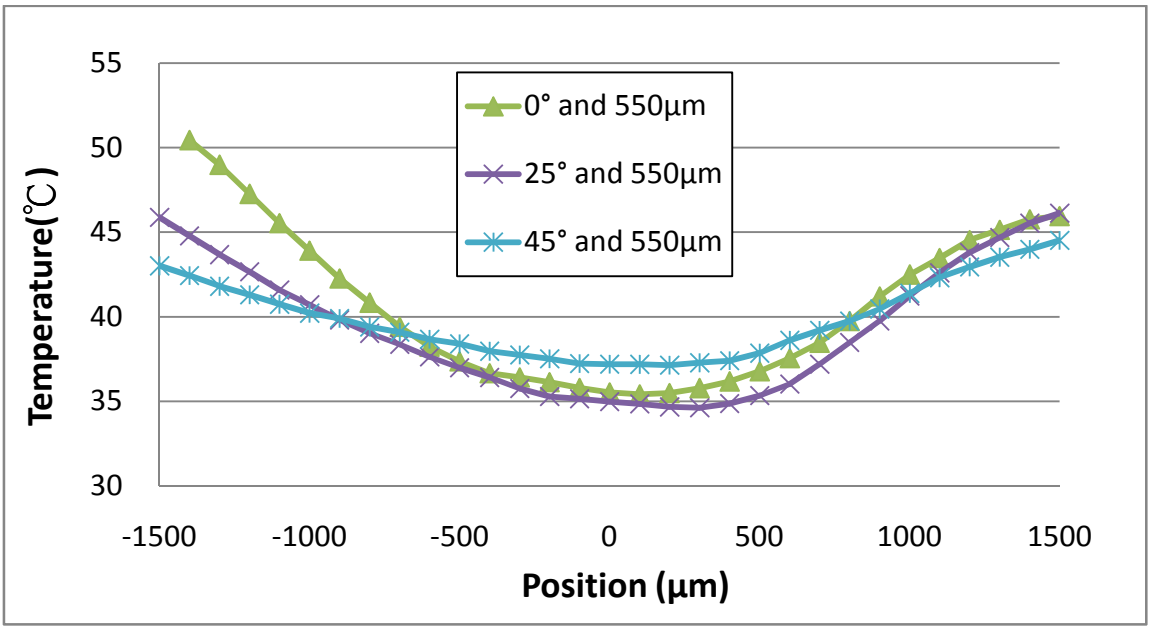

Figure 58 Temperature distribution for double streams with different impact angles

Temperature distribution at different horizontal orientations within the crater was also obtained as shown in Figure 59. Three temperature profile lines were generated along the three different orientations. The horizontal orientation of three different

temperature profile lines is defined the same way as in Figure 53. For all the inclined angle impact cases, the temperature profiles exhibit similar characteristics for all the horizontal orientations in the positive direction (upstream direction). However, the temperature profiles are markedly different in the downstream or negative direction for all the orientations. At 0° orientation, it exhibits similar film thickness as in other orientations; however, it is characterized by the best heat transfer performance since the tangential velocity gradient is expected to reach a maximum in this direction. The film thickness data are needed to investigate the relationship between surface temperature and film thickness.

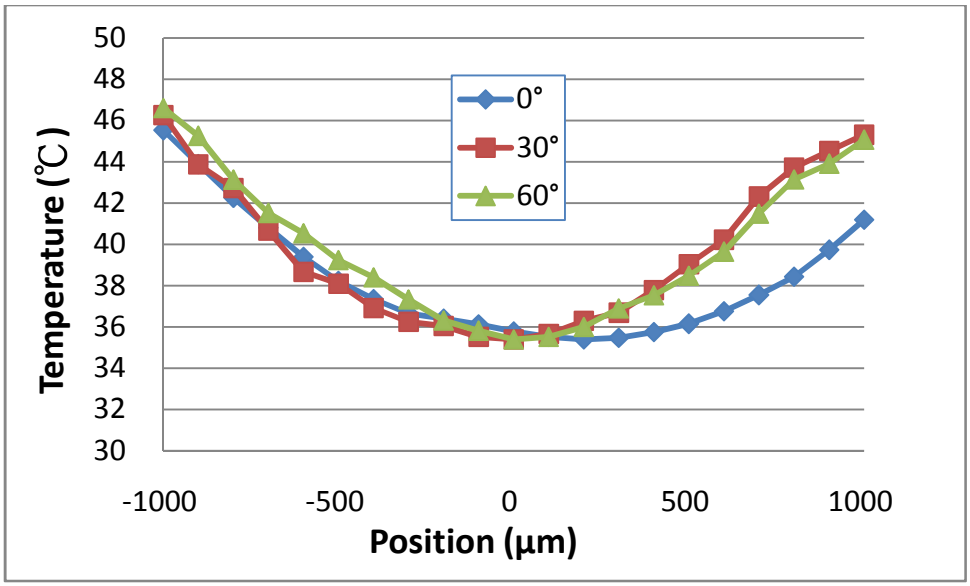

(a)

Figure 59 Temperature distribution at different horizontal orientations at impact angle of (a) 0° (b) 25° (c) 45°

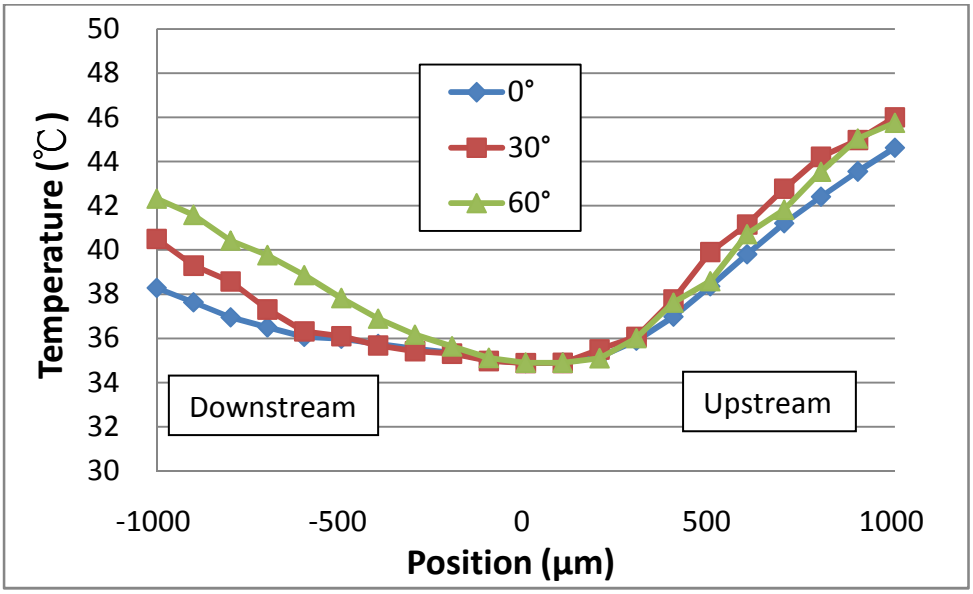

(b)

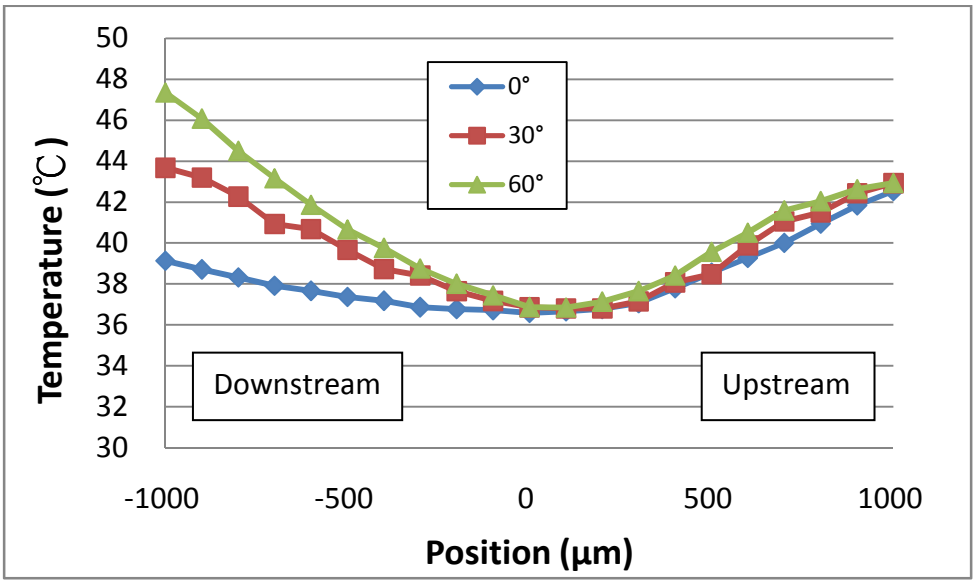

(c)

Figure 59 Continued.

4.3.3. Effect of double stream on film thickness

Film thickness was measured using the same technique used for the single stream experiment. The laser light source was aligned with only one of the droplet impact point for 0° impact since two craters are symmetric. For the inclined impact cases, the laser light was focused on the downstream side of droplet impact point. Since the fluid film was found to be chaotic and thick near where the two adjacent impact crater collided and coalesced, film thickness data was not obtained at a horizontal orientation of 90°. Figure 60 shows the measurement points for fixed impact angle and fixed impact spacing cases.

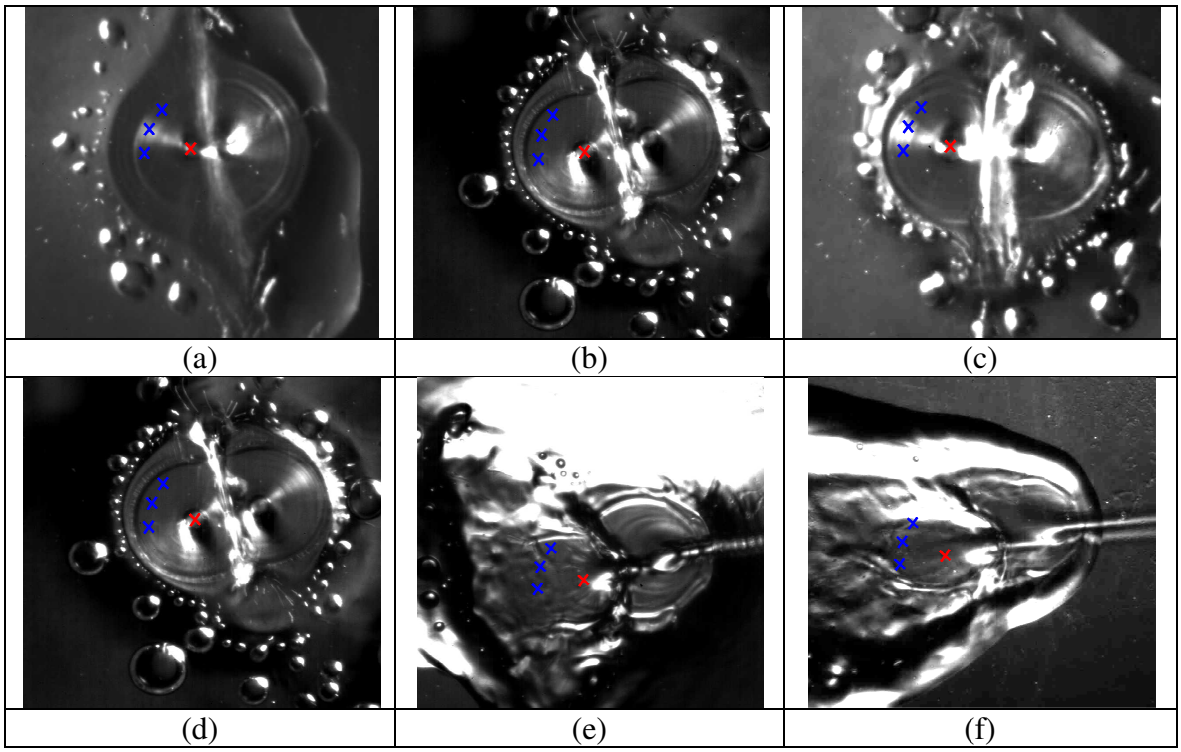

Figure 60 Film thickness measurement positions (a) 0°_330 µm (b) 0°_550 µm (c) 0°_650 µm (d) 0°_550 µm (e) 25°_550 µm (f) 45°_550 µm with heat flux of 23 W/cm^2:

The maximum and minimum film thickness for double streams cases are shown in Figures 61 and 62. It is found that the position does not have a significant effect on film thickness. Film thickness values are nearly constant for three different horizontal orientations within the crater. Therefore, the thickness within the impact crater was assumed to be constant in following analyses.

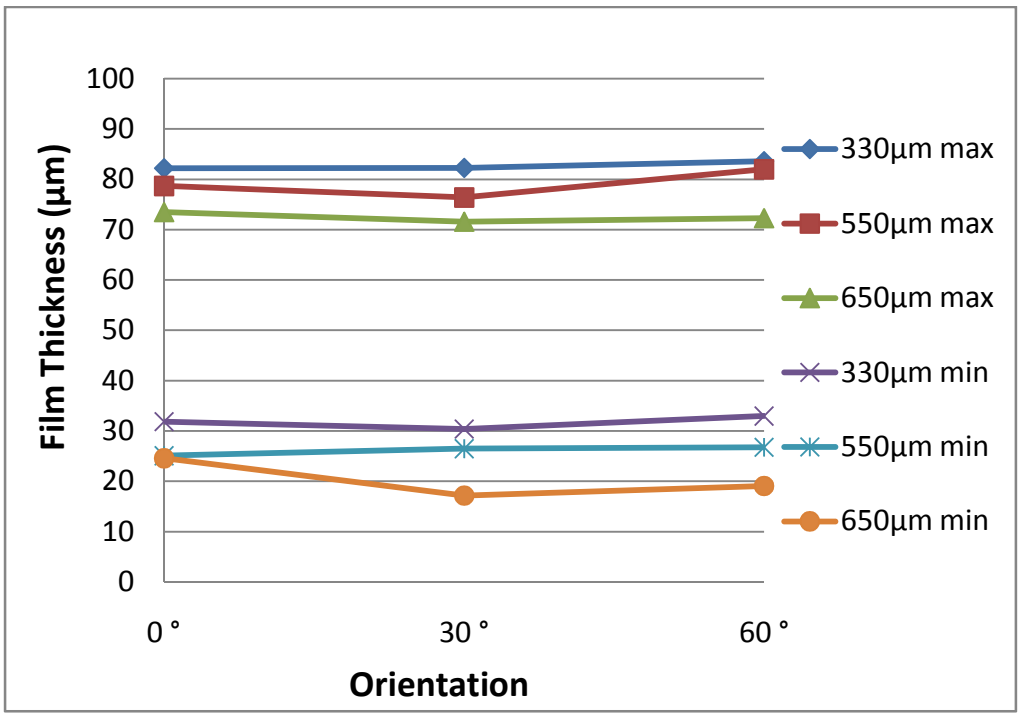

Figure 61 Maximum and minimum film thickness for different impact spacings at different orientations with heat flux of 23 W/cm^2

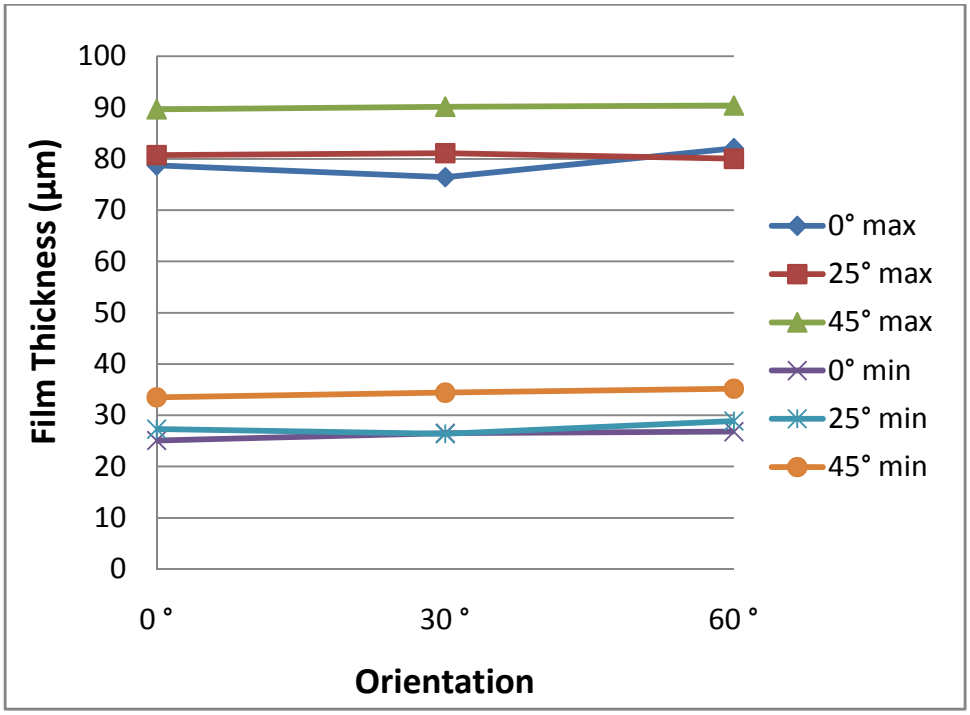

Figure 62 Maximum and minimum film thickness for different impact angles at different orientations with heat flux of 23 W/cm^2

The maximum and minimum film thickness values for double streams impact cases are shown in Figures 63 and 64. For fixed 0° impact angle, it can be seen that larger impact spacing results in thinner (lower) maximum and minimum film thickness. This implies that as the impact spacing increases which is consistent with the results presented earlier. Also, film thickness reduces as the heat flux increases for all impact spacings. It can be explained by the decrease of the fluid surface tension at higher surface temperature. The film spreads out easier at higher temperature resulting in thinner liquid films.

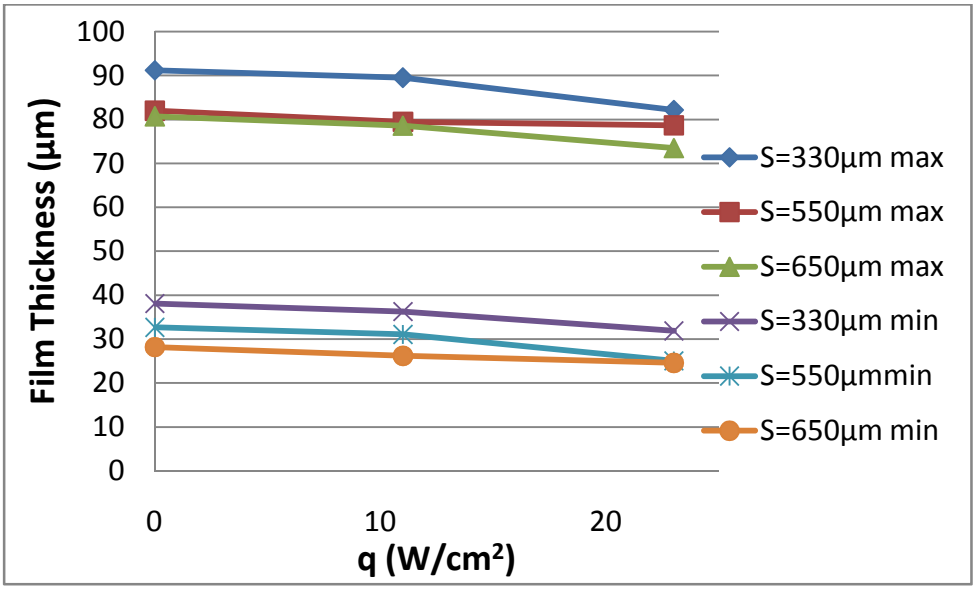

Figure 63 Maximum and minimum film thickness for different impact spacings under different heat flux conditions

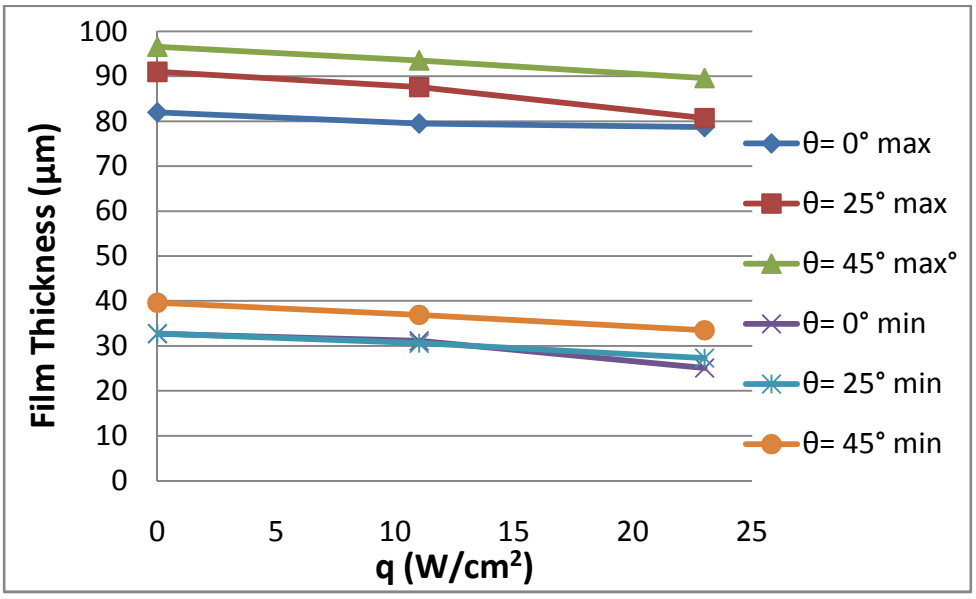

Figure 64 Maximum and minimum film thickness for different impact angles under different heat flux conditions

For fixed 550 μm spacing, it can be seen that at a 45° impact angle results in the thickest maximum and minimum film thickness values due to the lower vertical (fluid) momentum. Film thickness values are thinner for 0° and 25° impact angle cases. The results are different from the single stream experiment which shows that at only 0° impact angle exhibits the thinnest film thickness. As seen in Figure 56, there is less fluid collision and splashing at 25° impact angle than at 0° resulting in a thinner liquid film inside the impact zone. Moreover, less collision between the neighboring impact craters compensates for the lack of vertical (fluid momentum) resulting in similar thickness values as in 0° impact angle case. Therefore, increasing the impact angle slightly should reduce fluid collision when using multiple streams resulting in thinner liquid films and better heat transfer in well devised spray cooling systems.

A direct correlation between thickness and surface temperature for 0° impact angle is shown in Figure 65. The x-axis represents different orientations around the impact point. The primary y-axis represents the film thickness while the secondary y-axis stands for surface temperature. It can be seen that both film thickness and surface temperature are dependent on impact spacing but relatively insensitive to horizontal orientation. That means surface temperature depends only on the film thickness for 0° impact case when the fluid velocity gradient is expected to be symmetric with respect to the impact point.

The correlation between thickness and surface temperature for fixed impact spacing 550 μm and different impact angles is shown in Figure 66. The thickness is found to be dependent on impact angle. At 0° and 25° impact angles result in similar

film thickness while at 45° impact angle shows thicker thickness. Surface temperature also varies with different horizontal orientations for inclined impact cases. When the orientation angle increases, the surface temperature increases in a small amount. At 0° orientation position (downstream point) exhibits the lowest temperature. This is expected since the tangential fluid velocity is expected to reach a maximum in that direction promoting single-phase forced convection.

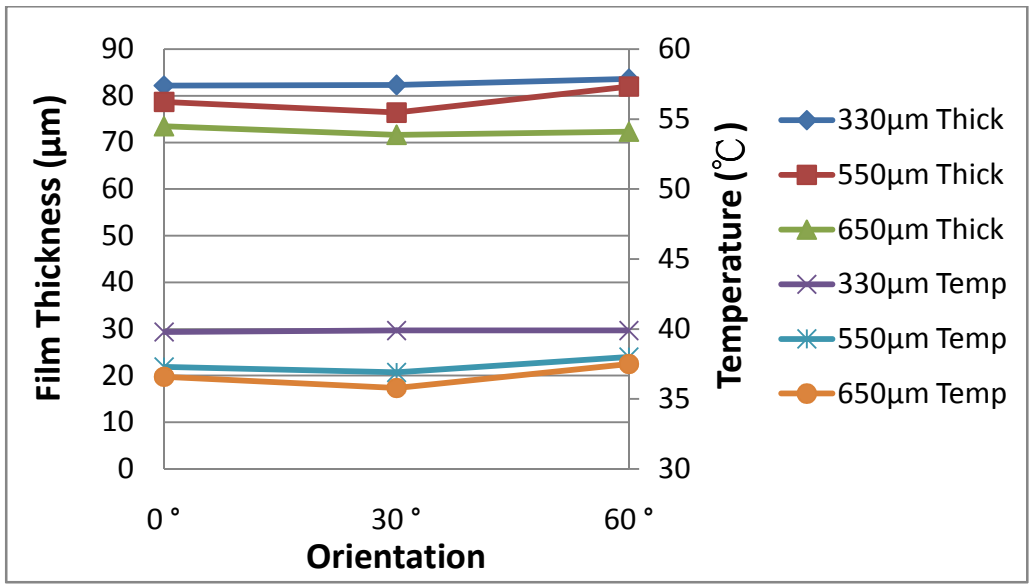

(a)

Figure 65 Relation between surface temperature and (a) maximum (b) minimum film thickness with different orientations and different impact spacings

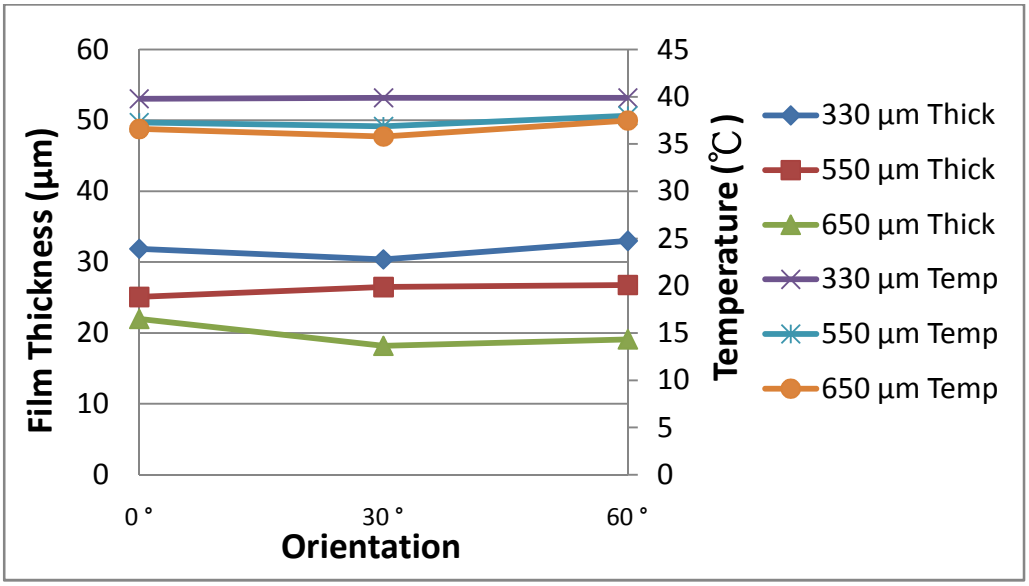

Figure 65 continued. (b)

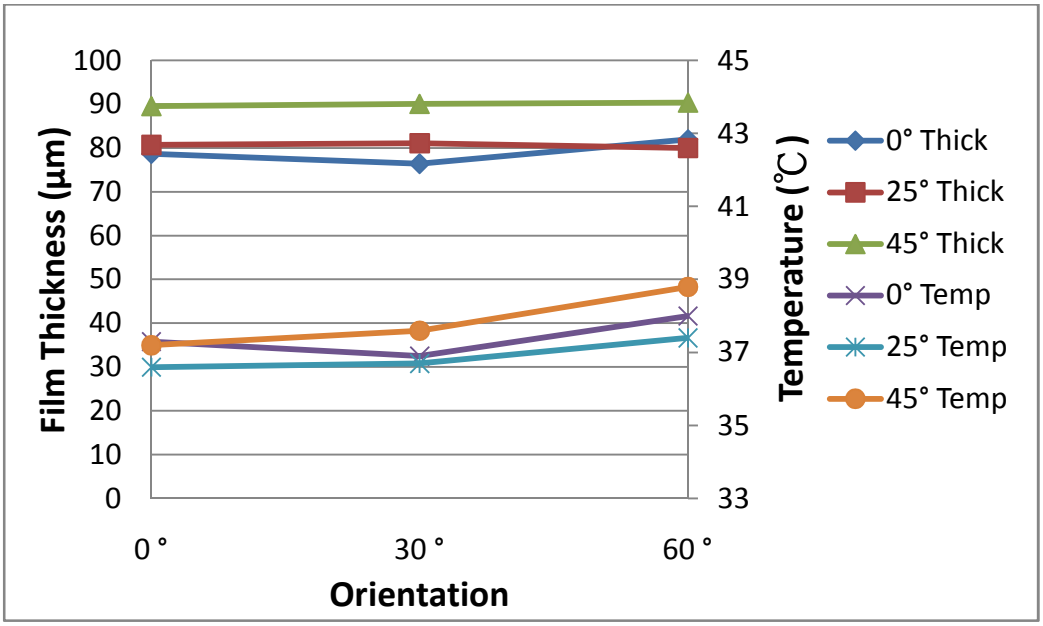

(a)

Figure 66 Relation between surface temperature and (a) maximum (b) minimum film thickness with different orientations and different impact angles

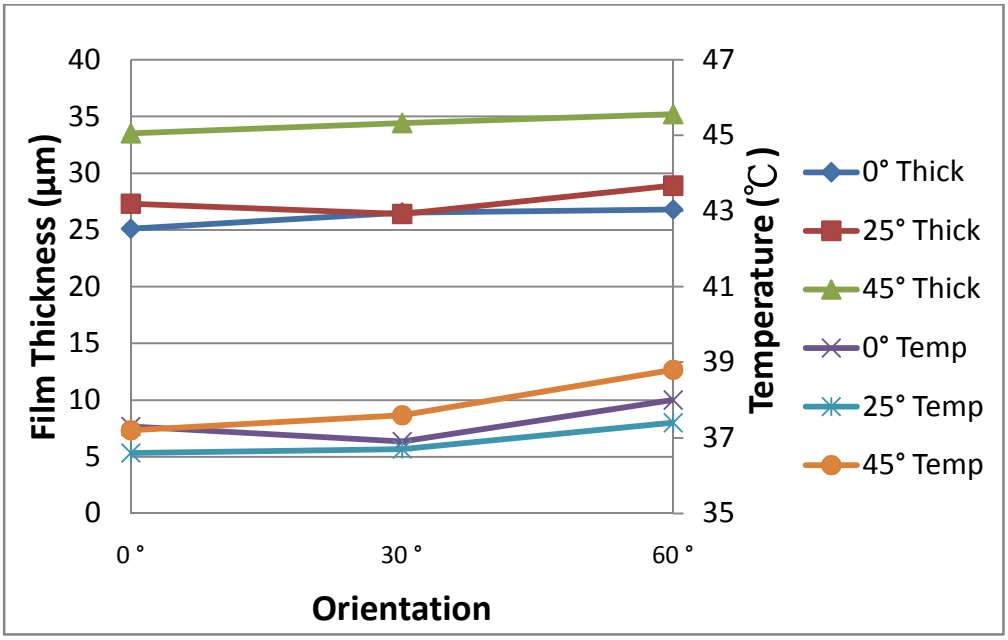

Figure 66 continued. (b)

5. CONCLUSION

Single stream droplet impingement cooling at different impact angles was performed to investigate the effect of impact angle on heat transfer. Double streams droplet impingement at different impact spacings and impact angles were also tested to understand their effects on surface cooling. The droplet and impact crater images were captured using a high speed imaging system. An infrared thermal imaging technique was used to measure surface temperature within the heat transfer area. The total laser light reflection approach was used to measure the film thickness within the impact crater.

From single stream thermal image results, it was found that at 0° impact angle results in the best heat transfer performance. As the impact angle was increased, the minimum surface temperature increased as well. Moreover, impact area was found to be the largest at 0° impact angle. This proves the theory that vertical impact momentum determines the crater formation size [27]. In addition, film thickness was found to be the thinnest at 0° impact angle. From the relation between surface temperature and film thickness, forced convection was proved to be the main heat transfer mechanism inside the impact crater. For fixed impact angle, the impact area was increased gradually before reaching the critical heat flux conditions. It can be attributed to the reduction of the surface tension with respect to fluid temperature.

From the double stream results, optimum spacing was defined and found in this study. An optimum spacing between adjacent droplet streams should result in low surface temperature with minimal variation within the two adjacent impact zones. The

optimum spacing was found to be mainly dependent on flowrate. Also, optimum spacing was found to be directly proportional to the flowrate per droplet stream. This helps clarify previous controversies regarding whether sparse or dense sprays results in better heat transfer. In addition, for fixed flow rate, dryout occurred between adjacent impacts when the spacing was larger than a critical spacing value, which caused large temperature variation within the two adjacent craters. On the other hand, fluid collision was observed at the spacing became smaller than the critical spacing, which led to the spreading-splashing mode and lower heat transfer.

The spreading-splashing mode for double stream impact was further investigated to understand its effect on heat transfer. For fixed 0° impact angle, minimum temperature was reduced significantly as the impact spacing increased within spreading-splashing region. For fixed impact spacing, small inclined impact angles were found to reduce the minimum temperature by minimizing the splashing level between adjacent impact points. In addition, film thickness within the impact crater was measured. It was found that film thickness is affected adversely by reducing impact spacing. Small impact angle for double stream was found to slightly reduce the film thickness and enhance the heat transfer. Film thickness was further compared at different horizontal orientations within the impact point. The film thickness was found to be consistent and uniform within the measurement region. However, the temperature distribution was different at different horizontal orientation. This leads to the conclusion that the tangential velocity distribution plays an important role in temperature distribution. Velocity field within the

impact crater should be measured with techniques such as micro Particle Image Velocimetry (μPIV) and compared with the numerical simulation.

REFERENCES

[1] I. Mudawar, "Assessment of high-heat-flux thermal management schemes," *IEEE Trans. Compon. Packag. Technol.*, vol. 24, pp. 122-141, 2001.

[2] C. O. Pedersen, "An experimental study of the dynamic behavior and heat transfer characteristic of water droplets impinging upon a heated surface," *Int. J. Heat Mass Transfer*, vol. 1, pp. 39-50, 1972.

[3] C. F. Ma, and A. E. Bergles, "Jet impingement nucleate boiling," *Int. J. Heat Mass Transfer*, vol. 29, pp. 1095-1101, 1986.

[4] M. Ghodbane, and J. P. Holman, "Experimental study of spray cooling with Freon-113," *Int. J. Heat Mass Transfer*, vol. 34, pp. 1163-1174, 1991.

[5] R. D. Watson, "Structure for handling high heat fluxes," *J. Nuclear Materials*, vol. 176, pp. 110-121, 1990.

[6] A. G. Pautsch, and T. A. Shedd, "Adiabatic and diabatic measurements of the liquid film thickness during spray cooling with FC-72," *Int. J. Heat Mass Transfer,* vol. 49, pp. 2610-2618, 2006.

[7] M. Ghodbane, and J. P. Holman, "Experimental study of spray cooling with Freon-113," *Int. J. Heat Mass Transfer*, vol. 34, pp. 1163-1174, 1991.

[8] S. S. Hsieh, and C. H. Tien, "R-134a spray dynamics and impingement cooling in the non-boiling regime," *Int. J. Heat Mass Transfer*, vol. 50, pp. 502-512, 2006.

[9] B. Horacek, and J. Kim, K. T. Kiger, "Spray cooling using multiple nozzles: Visualization and wall heat transfer measurement," *IEEE Transaction on Device and Materials Reliability*, vol. 4, no. 4, pp. 614-625, 2004.

[10] R. H. Chen, and J. C. Chow, J. E. Navedo, "Optimal spray characteristics in eater spray cooling," *Int. J. Heat Mass Transfer*, vol. 47, pp. 5095-5099, 2004.

[11] I. Mudawar, and K. A. Estes, "Optimizing and predicting CHF in spray cooling of a square surface," *J. Heat Transfer*, vol. 118, pp. 672-679, 1996.

[12] A. G. Pautsch, and T. A. Shedd, "Spray impingement cooling with single and multiple nozzle arrays. Part I: Heat transfer data using FC-72," *Int. J. Heat Mass Transfer*, vol. 48, pp. 3167-3175, 2005.

[13] Military Standardization Handbook 217C, "Reliability prediction of electronic equipment," U.S. Department of Defense, Washington, D.C., 1979.

[14] H. Martin, "Heat and mass transfer between impinging gas jets and solid surfaces," *Advances in Heat Transfer*, vol. 13, pp.1-60, 1977.

[15] J. Schwarzkof, T. Cader, K. Okamoto, B. Q. Li, and B. Ramarprian, "Effect of spray angle in spray angle in spray cooling thermal management of electronics," *ASME Heat Transfer Engineering Summer Conference*, Charlotte, NC, pp. 423-431, 2004.

[16] G. Aguilar, and H. Vu, J. S. Nelson, "Influence of angle between the nozzle and skin surface on the heat flux and overall heat extraction during cryogen spray cooling," *Physics in Medicine Biology*, vol. 49, pp. 147-153, 2004.

[17] M. Visaria, and I. Mudawar, "Theoretical and experimental study of the effects of spray inclination on two-phase spray cooling and critical heat flux," *Int. J. Heat Mass Transfer*, vol. 51, pp. 2398-2410, 2007.

[18] E. A. Silk, and J. Kim, K. Kiger, "Spray cooling of enhanced surfaces: Impact of structured surface geometry and spray axis inclination," *Int. J. Heat Mass Transfer*, vol. 49, pp. 4910- 4920, 2006.

[19] W. J. Yang, "Theory on vaporization and combustion of liquid drops of pure substances and binary mixtures on heated surfaces," *Institute of Space and Aeronautical Science*, University of Tokyo, Report no. 535, pp. 423-455, 1975.

[20] W. M. Healy, J. G. Hartley, and S. I. Abdel-Khalik, "Comparison between theoretical models and experimental data for spreading of liquid droplets impacting a solid surface," *Int. J. Heat Mass Transfer*, vol. 39, pp. 3079-3082, 1996.

[21] S. Nukiyama, "The maximum and minimum values of the heat transmitted from metal to boiling water under atmospheric pressure," *Int. J. Heat Mass Transfer*, vol. 37, no. 6, pp. 367-374, 1934.

[22] J. G. Leidenfrost, "On the fixation of water in diverse fire," *Int. J. Heat Mass Transfer*, vol. 9, pp.1153-1166, 1966.

[23] Z. Tamura, and Y. Tanasawa, "Evaporation and combustion of a drop contacting with a hot surface," Proceeding of the 7^{th} *Int. Symposium Combustion*, Butterworth's, London, pp. 509-522, 1959.

[24] S. M. Sellers, and W. Z. Black, "Boiling heat transfer rates for small precisely placed water droplets on a heated horizontal plate," *J. Heat Transfer*, vol. 130, no 5, pp. 1-4, 2008.

[25] G. Soriano, "Study the physics of droplet impingement cooling," Ph.D. dissertation, Texas A&M University, College Station, 2011.

[26] S. M. Sellers, "Heat transfer resulting from evaporation of liquid droplets on a horizontal heated surface," Ph.D. dissertation, Georgia Institute of Technology, Atlanta, 2000.

[27] C. H. R. Mundo, M. Sommerfeld, and C. Tropea "Droplet wall collisions: Experimental studies of the deformation and breakup process," *Int. J. Multiphase Flow*, vol. 21, no. 2, pp. 151-173, 1995.

[28] S. H. Hu, C. H. Cui, and X. J. Ma, "The effect of temperature and concentration on surface tension for ethanol solution," Proceeding of the *Power and Energy Engineering Conference*, Wuhan, China, pp. 416-419, 2010.

APPENDIX A

UNCERTAINTY ANALYSIS

A. Heat flux measurement and uncertainty analysis

There are four heat transfer mechanisms (see Figure 67) in this study, including the heat dissipation through the fluid (q''_{fluid}), natural convection through both sides of the surface (q''_{conv}), conduction through the holder (q''_{holder}) and conduction and then convection through the connecting wires. In this study, the heat loss was determined by knowing the temperature difference between the heater and the surrounding. In order to estimate the heat loss, the surface was heated by controlling the power input when no fluid was present. Average surface temperatures were recorded when reaching steady state at different power input values, which was used to indicate the relation between the heat loss and the power input. The heat losses measured experimentally are in the order of 7 to 12 % of the total power input. Figure 68 shows the overall heat loss as a function of average surface temperature.

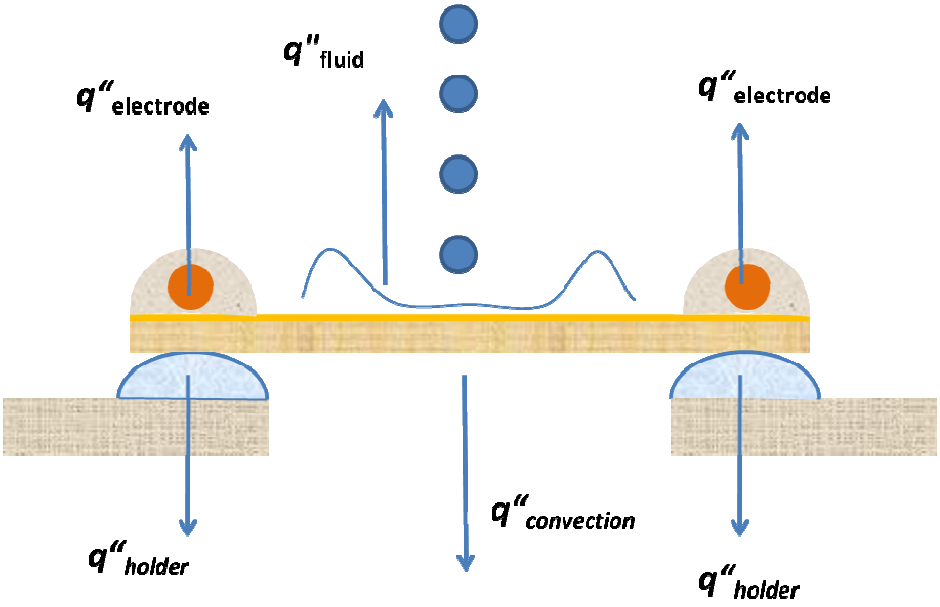

Figure 67 Heat loss mechanisms in the heater setup

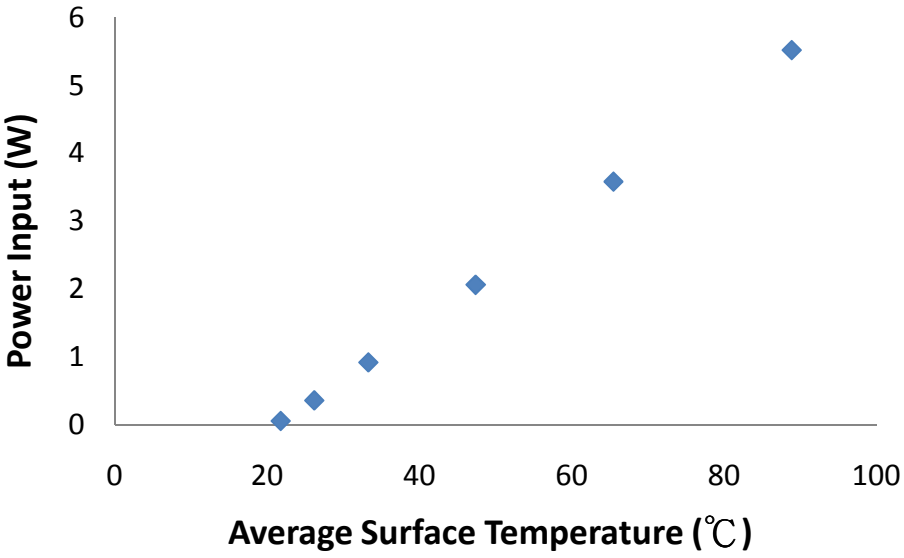

Figure 68 Power input as a function of average surface temperature for ITO heater

Equation 25 was used for computing the actual amount of heat flux for the impact cooling experiment.

$$q" = \frac{P_{in} - q_{loss}}{A_{heater}} \quad (25)$$

The uncertainty of the heat flux can be calculated using the Kline-McClintock methodology [30], as follows:

$$u_{q"}^2 = \left(\frac{\partial q"}{\partial V} u_V\right)^2 + \left(\frac{\partial q"}{\partial I} u_I\right)^2 + \left(\frac{\partial q"}{\partial T} u_T\right)^2 + \left(\frac{\partial q"}{\partial A} u_A\right)^2 \quad (26)$$

where $u_{q"}$ is the uncertainty of the heat flux, u_V is the uncertainty of the voltage reading, u_I is the uncertainty of the current reading, u_T is the uncertainty of the temperature reading, u_A is the uncertainty of the area measurement. The error associated with the measurement of voltage and current of power supply GEN-600-2.7 used in this study according to manufacturers were:

u_V=0.1% reading + 0.2% rated output voltage

u_I=0.1% reading + 0.4% rated output current

The uncertainty of the voltage and current under the maximum heat flux condition in this study were 1.2 V and 0.012 A. By putting these values into Equation 26, the uncertainty of the heat flux was found to be 1.24 W/cm^2, which is approximately 5% of the maximum heat flux obtained during the experiment.

B. Temperature measurement and uncertainty analysis

The temperature of an object was obtained by measuring the irradiance W (W/str-m^2) from the infrared camera. The interested temperature position was at the interface between the ZnSe substrate and the ITO coating. There are five irradiance components received by the IR camera in this study:

1. Irradiance from the surrounding reflected on the substrate surface, and transmitted through ambient air.

2. Irradiance from surrounding transmitted through the substrate, reflected on ITO coating and transmitted through ambient air.

3. Irradiance emitted by ITO coating transmitted through substrate and ambient air.

4. Irradiance emitted from the substrate, and transmitted through ambient air.

5. Irradiance emitted by ambient air.

Figure 69 shows the schematic of the five irradiance components received by the IR camera in this study.

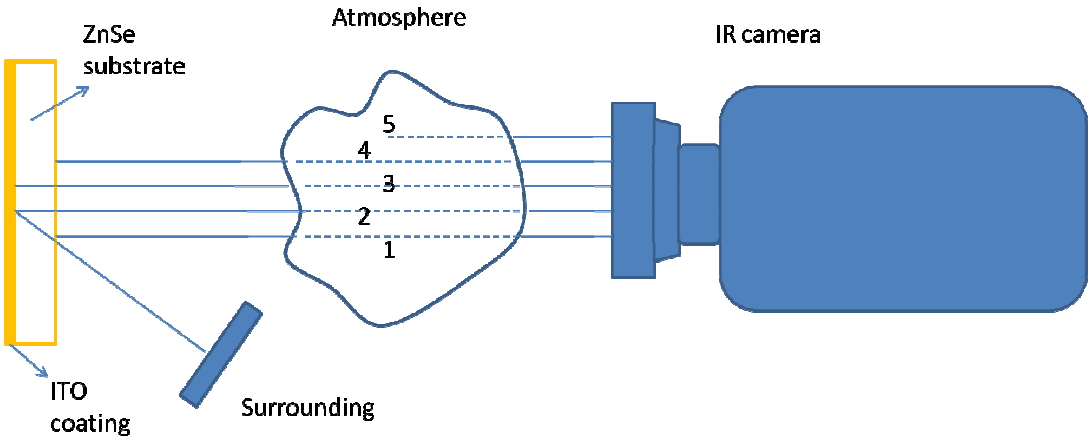

Figure 69 Schematic diagram of infrared temperature measurement technique

The total irradiance received by the IR camera from each of the components can be expressed as follows:

$$W_{tot} = \rho_{sub}\tau_{atm}W_{sur} + \tau_{sub}\rho_{obj}\tau_{sub}\tau_{atm}W_{surr} + \varepsilon_{obj}\tau_{sub}\tau_{atm}W_{obj} + \varepsilon_{sub}\tau_{atm}W_{sub} + \varepsilon_{atm}W_{atm} \quad (27)$$

It is assumed that the irradiance from the substrate can be represented by irradiance of the object and the difference irradiance:

$$W_{sub} = W_{obj} + W_{diff} \quad (28)$$

Substituting Equation 28 into Equation 27, the total irradiance can be expressed as:

$$W_{tot} = (\rho_{sub} + \tau_{sub}\rho_{obj}\tau_{sub})\tau_{atm}W_{sur} + (\varepsilon_{obj}\tau_{sub} + \varepsilon_{sub})\tau_{atm}W_{obj} + \varepsilon_{atm}W_{atm} + \varepsilon_{sub}\tau_{atm}W_{diff} \quad (29)$$

where ρ is the reflectivity, τ is the transmissivity, and ε is the emissivity. Emissivity of the substrate can be estimated based on the transmissivity property of ZnSe and the assumption that ZnSe is a gray body in the wavelength range of interest (8 to 12 μm). Transmissivity of the ZnSe with a thickness of 1.5 mm with an antireflective coating was above 0.9. Assuming a perfect coating with zero reflectivity, the emissivity of the value was in the order of 0.04. Emissivity was even lower in the case of a non-perfect coating. The irradiance difference term represents the irradiance difference between ZnSe – ITO interface and the ZnSe surface. Irradiance is a function of absolute temperature. Since the thickness of ZnSe was only 12 mm, the temperature difference between surfaces was

small. Thus it is reasonable to assume the irradiance difference term can be ignored. The equivalent reflectivity and emissivity are defined as follows:

$$\rho_{eq} = \left(\rho_{sub} + \tau_{sub}\rho_{obj}\tau_{sub}\right) \quad (30)$$

$$\varepsilon_{eq} = \left(\varepsilon_{obj}\tau_{sub} + \varepsilon_{sub}\right) \quad (31)$$

Substitute Equations 30 and 31 into Equation 29:

$$W_{tot} = \rho_{eq}\tau_{atm}W_{surr} + \varepsilon_{eq}\tau_{atm}W_{obj} + \varepsilon_{atm}W_{atm} \quad (32)$$

Equation 32 represents the total irradiance received by the infrared camera from an equivalent opaque surface. Based on Equation 32 there are three irradiance components:

1. Irradiance from surrounding reflected on an opaque surface, and transmitted through the ambient air.
2. Irradiance emitted by the equivalent surface and transmitted through the ambient air.
3. Irradiance emitted by the ambient air.

To simplify Equation 32, the following assumption were made and found to be valid through experimental tests:

1. At any surface, all the energy is absorbed, reflected or transmitted. This means:

$$\alpha + \rho + \tau = 1 \quad (33)$$

2. ITO surface is a gray body. In other words, the emissivity and absorptivity of the ITO are the same and constant in the wavelength of interest. This is valid for the small temperature range.

$$\alpha_{ITO} = \varepsilon_{ITO} \quad (34)$$

3. The ITO surface is opaque which means the transmissivity is zero in the wavelength of interest.

$$\tau_{ITO} = 0 \quad (35)$$

4. Ambient air is considered as a gray body and its reflectivity is assumed to be zero.

$$\alpha_{atm} = \varepsilon_{atm} \quad (36)$$

$$\rho_{atm} = 0 \quad (37)$$

Substitute Equations 33 to 37 into Equation 32, the total irradiance can be expressed as follows:

$$W_{tot} = \varepsilon\tau W_{obj} + (1-\varepsilon)\tau W_{surr} + (1-\tau)W_{atm} \quad (38)$$

The radiation energy was received by the sensor of the IR camera and then converted to an output signal. The signal was amplified and converted to digital value D. The digital reading of the camera and irradiance are related according to the following equation:

$$D_{tot} = A + BW_{tot} \quad (39)$$

where A is constant taking into account internal irradiance effects of the camera, and B is constant taking into account detector response to irradiance. Constant A is a fixed response of the sensor mostly due to the heat generation of electronic components inside

the camera. Constant B represents the linear response of the incoming irradiance, which at higher values of B, the more sensitive the camera becomes.

In order to obtain an expression of absolute temperature from the digital readings, an approximation of the absolute blackbody temperature as a function of irradiance was used.

$$T_{tot} = F + G \ln W_{tot} \quad (40)$$

where F and G are constants used to represent the Plank Function. By substituting Equation 39 into 40, the expression of the absolute temperature with the digital reading was obtained:

$$T_{tot} = A^* + B^* \ln D_{tot} \quad (41)$$

where A^* is the constant associated with the internal effect of the camera and B^* is the constant associated with the detector response of the camera. The constant A^* and B^* are obtained by using the least square fit technique using the temperature curve. The calibration was performed by the IR camera manufacturer (FLIR system) using NIST-traceable calibrated blackbody sources and thermocouples.

In order to obtain the temperature of the ITO surface, Equations 38 and 39 were combined and solved for the digital reading of the ITO surface.

$$D_{ITO} = \frac{1}{\varepsilon\tau} D_{tot} - \frac{1-\varepsilon}{\varepsilon\tau} D_{surr} - \frac{1-\tau}{\varepsilon\tau} D_{atm} \quad (42)$$

Substituting Equation 42 into 41, the following equation was obtained.

$$T_{ITO} = A^* + B^* \ln\left(\frac{1}{\varepsilon\tau} D_{tot} - \frac{1-\varepsilon}{\varepsilon\tau} e^{\frac{T_{surr}-A^*}{B^*}} - \frac{1-\tau}{\varepsilon\tau} e^{\frac{T_{atm}-A^*}{B^*}}\right) \quad (43)$$

The temperature of the ITO surface can be obtained by measuring the digital value of the object. This equation is embedded in the Examine IR software. It requires surrounding and ambient temperatures, emissivity of the object and transmissivity of ambient air to be able to provide the surface temperature. The software has an embedded algorithm to calculate transmissivity of ambient air using relative humidity of air, temperature, and distance from object to the camera.

The first step to compute the temperature uncertainty of the camera is to plot the apparent temperature and the digital counts of the camera over a temperature range of interest (Figure 70). Apparent temperature is the temperature of the object when emissivity is set to one. Using the least squares method and Equation 41, the values of the calibration constants of the camera were found to be A^* = -1014.8 and B^* = 104.97.

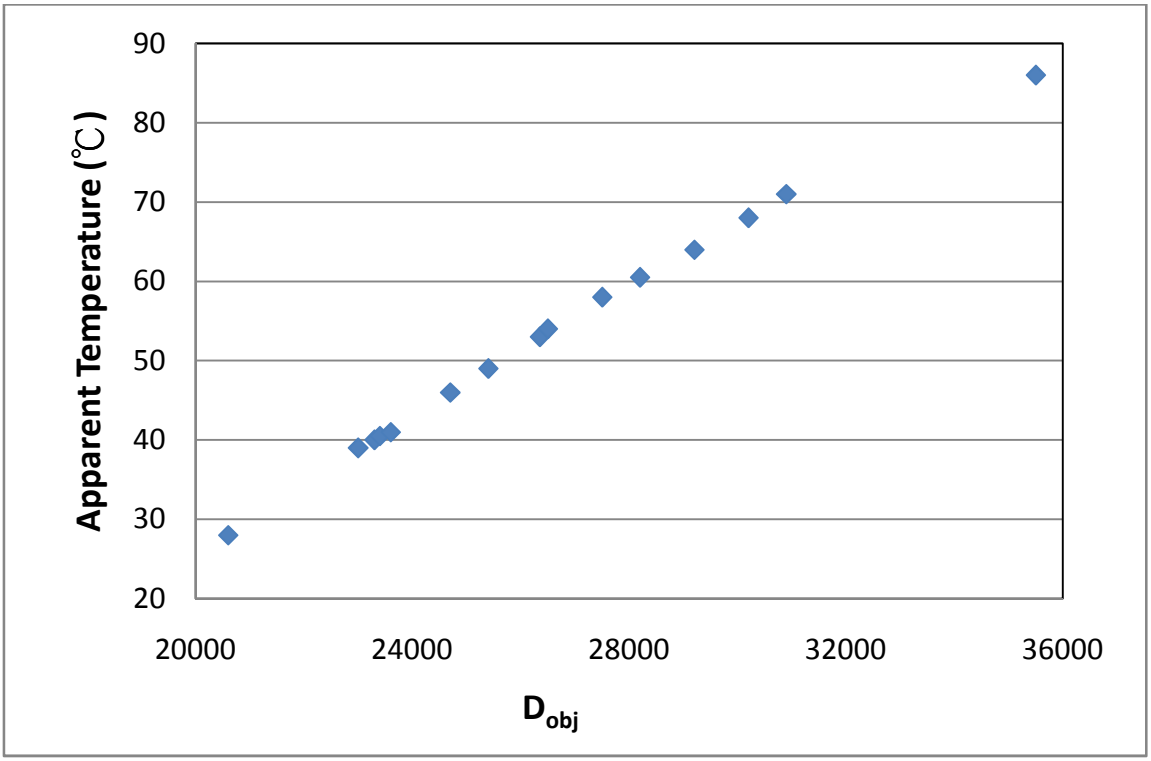

Figure 70 Apparent surface temperature vs. digital counts

Using Equation 41 and the Kline McClintock methodology, the temperature uncertainty can be found as follows:

$$\Delta T = \frac{B^{*}\Delta D_{ITO}}{D_{ITO}} \qquad (44)$$

At small distances between the camera and target, the tansmissivity of ambient air is assumed to be one and the reflectivity of the ambient air is assumed to be zero. Equation 44 then can be written as,

$$\Delta T = \frac{B^*}{D_{tot}-(1-\varepsilon_{ITO})D_{surr}}\left[\Delta D_{tot}^2 + \Delta D_{surr}^2\left(1-\varepsilon_{eq}\right)^2 + \Delta\varepsilon_{ITO}^2\left(\frac{-D_{ITO}+D_{surr}}{\varepsilon_{ITO}}\right)^2\right]^{1/2} \quad (45)$$

D_{tot} is obtained by taking readings of the object in digital counts mode, and D_{surr} is obtained by taking readings at the target location covered with a reflective foil. The uncertainty values of the object and surrounding digital readings are obtained by computing the standard deviation of statistically significant samples of the total digital value and the surroundings digital value. By measuring three different digital reading values of the equivalent surface, the uncertainty can be determined using Equation 45. The temperature reading with its uncertainty is presented in Table 4.

Table 4 Temperature uncertainty at different temperature values

Temperature (°C)	Uncertainty (°C)
30	±0.5
40	±0.8
50	±1.6

The variation of the uncertainty is mainly due to an increment of the difference between D_{surr} and D_{tot} as shown in the third term in Equation 45. If emissivity had a deterministic value, the surface temperature uncertainty would become ± 0.06°C at an apparent temperature of 55°C.

C. Emissivity measurement uncertainty analysis

The Standard ASTM E1933 “Standard test methods for measuring and compensating for emissivity using infrared imaging radiometers” was used in this experiment. The procedure was as follows:

Step 1: Measure the digital reading of the irradiance from the surroundings where the temperature measurement by placing a reflective foil over the surface to prevent any irradiation from the object from being measured by the camera and recording digital counts. Since the camera and the object are so close together, the effect of the ambient air is negligible and only the irradiance from the surrounding is measured.

Step 2: Apply a coating of known emissivity to a small section of the surface of the ITO heater.

Step 3: Heat the object so its temperature is at least 30°C above the temperature of the surroundings. This is done by placing the ITO heater in the laboratory oven for 3 hours at three different temperatures. Measure both the number of irradiance counts from the target and object of known emissivity.

Step 4: Calculate the emissivity using the following equation:

$$\varepsilon_{obj} = \frac{D_{obj} - D_{surr}}{D_{ref} - D_{surr}} \varepsilon_{ref} \quad (46)$$

where D represents the digital reading of the camera in number of counts. The reference used for this measurement was an electrical vinyl tape Super 88 with a known emissivity value of ε=0.95 ±0.05. The calculated emissivity values at different temperatures are listed at Table 5:

Table 5 Emissivity values of equivalent surfaces at different temperatures

Temperature (°C)	Emissivity
74	0.790
52	0.798
45	0.798

The proposed expression of the emissivity uncertainty is expressed as follows:

$$\frac{\Delta\varepsilon_{tar}}{\varepsilon_{tar}} = \sqrt{\left(\frac{\Delta\varepsilon_{ref}}{\varepsilon_{ref}}\right)^2 + 2\Delta D^2\left(\frac{1}{(D_{tar}-D_{sur})^2} + \frac{1}{(D_{ref}-D_{sur})^2}\right)} \quad (47)$$

The uncertainty value of the counts readings was found by computing the standard deviation (σ) of statistically significant readings of the uniform target. Assuming a normal distribution of the measurements, a range of three-standard deviation (3σ) gives a probability of 99.7% that the results fall within the range of accuracy. Applying Equation 47, the emissivity uncertainty of the equivalent surface was found to be 0.792 ±0.043.

D. Droplet diameter measurement uncertainty analysis

The droplet diameter was measured using the image analysis tool from National Instrument Vision Assistant software. The projected vertical surface area of each droplet was obtained first and then used to compute the droplet diameter. A scale of 1.5

μm/pixel was used for the measurement. The uncertainty of the diameter measurement was as follows:

$$u_{d_d} = \frac{\partial d_d}{\partial A} u_A \quad (48)$$

The droplet diameter uncertainty was found to be ±7.5 μm.

E. Droplet velocity measurement uncertainty analysis

The droplet velocity was calculated from Equation 49:

$$v_d = L \times f \quad (49)$$

where L is the distance between droplets and f is the disturbance frequency from the function generator. The uncertainty of the velocity measurement was given by:

$$u_{v_d}^2 = \left(\frac{\partial v_d}{\partial L} u_L\right)^2 + \left(\frac{\partial v_d}{\partial f} u_f\right)^2 \quad (50)$$

The distance of each droplet was measured using a magnification of 4.5 μm/pixel with a corresponding uncertainty of ± 20 μm. Uncertainty of frequency for signal generator (BK Precision Model 4011A) was ± 10 Hz. By substituting these values into Equation 50, the uncertainty of the droplet velocity was found to be ± 0.14 m/s.

F. Impact crater diameter measurement uncertainty analysis

The impact crater diameter was measured by the National Instrument Vision Assistant software. In the diameter measurement, a magnification of 5.88 μm/pixel was used. An estimated uncertainty of 4 pixels was considered for crater diameter measurements in the study. The corresponding uncertainty for the diameter measurement was estimated to be ± 24μm.

APPENDIX B

HFE 7100 FLUID SURFACE TENSION PROPERTY

Table 6 Surface tension of HFE-7100

T	σ
[°C]	[g s^{-2}]
12.4	15.82
14.6	15.58
16.8	15.30
19.7	15.05
21.7	14.77
23.9	14.48
26.4	14.21
29.2	13.92
32.0	13.64
34.4	13.36
37.1	12.98
40.8	12.72
44.4	12.01
48.5	11.62
51.7	11.39

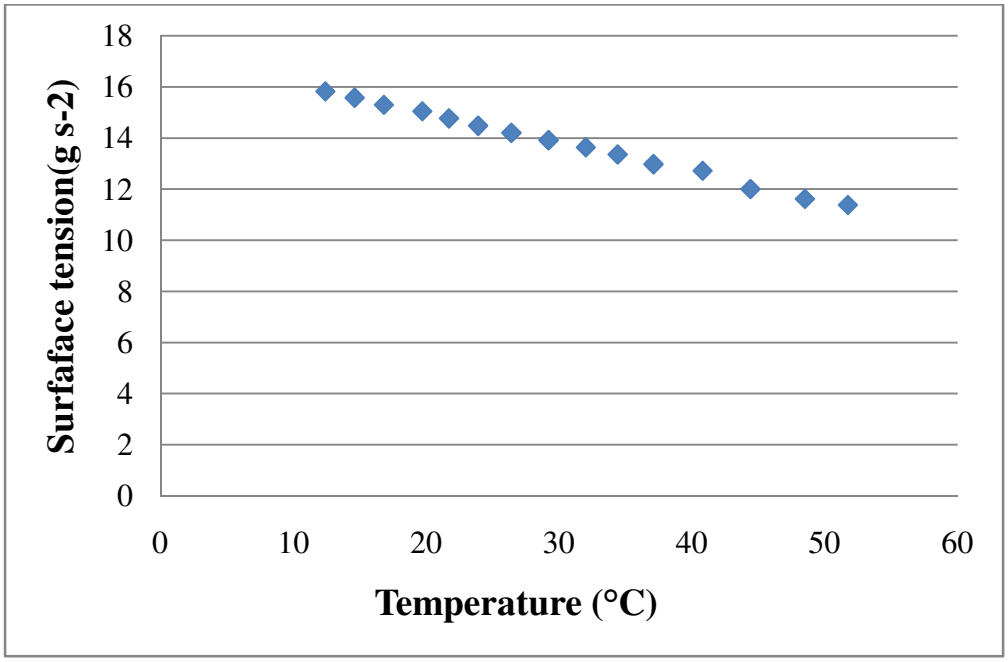

Figure 71 Surface tension of HFE-7100

VITA

Name: Hsin-Min Tsai

Address: Thompson Hall, TAMU
MS: 3367 TAMU
College Station, Texas 77843-3367

Email Address: window42@tamu.edu

Education: B.S., Mechanical Engineering, National Taiwan University, 2008

The typist for this thesis was Hsin-Min Tsai.